THE UNIVERSITY OF BIRMINGHAM

DOCTORAL THESIS

Robotic Disassembly of a Permanent Magnet DC Brushless Motor

Author: Chaozhi Liang

Supervisor: D T Pham

A thesis submitted in fulfilment of the requirements

for the degree of

DOCTOR OF PHILOSOPHY

in the

Department of Mechanical Engineering
University of Birmingham
UK, B15 2TT

February 2025

UNIVERSITY OF
BIRMINGHAM

University of Birmingham Research Archive

e-theses repository

This unpublished thesis/dissertation is copyright of the author and/or third parties. The intellectual property rights of the author or third parties in respect of this work are as defined by The Copyright Designs and Patents Act 1988 or as modified by any successor legislation.

Any use made of information contained in this thesis/dissertation must be in accordance with that legislation and must be properly acknowledged. Further distribution or reproduction in any format is prohibited without the permission of the copyright holder.

To my body,

To my wife,

To my parents.

Thank you for all the givens and losses.

each one shapes and completes me.

Acknowledgement

I am deeply grateful to my supervisor Professor. Duc Truong Pham and his AUTOREMAN research group, for continuous guidance and supports throughout my PhD journey.

I also extend my heartfelt appreciation to Professor Yongjing Wang and the ATARI research team for offering me a part-time job and providing invaluable assistance during my PhD.

I would like to thank staff at the University of Birmingham for your help in my PhD period.

This work was partially supported by EPSRC grant EPN0185241.

Abstract

Globally, the transition to electric vehicles (EVs) is accelerating. As these EVs reach the end of their service life, large quantities of valuable components, including electric motors, need to be remanufactured to achieve a more sustainable circular economy. Disassembly, the first step in the remanufacturing process, typically requires human intervention due to difficulties in automating it. This thesis investigates the robotic disassembly of a permanent magnet DC brushless motor. Six typical tasks are defined in motor disassembly, and four of them are studied, including the ‘Press-in’ task, ‘Press-on’ task, Unplugging task and Coil disassembly task.

Related to methodology, an analytical model implementing the magnetomotive force method was developed to calculate disassembly forces when removing a rotor with permanent magnets from a stator. This model provides reasonable accuracy in a very short calculation time without requiring high-performance computers compared with the finite element method. The average error rates of the FE method and MMF method are 16.7% and 26.3 %, respectively. By determining the material magnetic hysteresis, the improved analytical model predicts the force optimal positions, adapting to different cases of magnetic fields on the rotor with permanent magnets. Additionally, potential robotic solutions for the press-fit component disassembly tasks and the Coil disassembly task were investigated and experimentally validated.

A robotic cell, including two collaborative robots, a set of tools and two devices for disassembling press-fit components, is designed to fully automate the disassembly process. The disassembly quality in the robotic process is superior to that in the manual process, preventing unnecessary damage to the components. The time of the robotic process is 886 s at full capacity, which is 56.93% faster than that of the manual process (1390 s).

Robotic disassembly offers significant potential for advancing the circular economy in EV remanufacturing. However, although robotic automation improves disassembly efficiency and sustainability, it faces economic barriers due to high equipment costs. Future research should focus on cost-reduction strategies, expanding task automation, and hybrid approaches that combine robots and humans.

Declaration

I, Chaozhi Liang, hereby declare that this PhD thesis entitled "*Robotic Disassembly of a Permanent Magnet DC Brushless Motor*" was carried out on my own for the degree of Doctor of Philosophy at the University of Birmingham. I confirm that:

- The presented work has never been previously included in a thesis or dissertation submitted for a degree or other qualifications.

- Where the thesis is based on joint work done by myself with others, a clear statement has been made to illustrate how the contribution was exactly distributed.

- Except where stated otherwise by reference or acknowledgement, the work presented is entirely composed by myself.

Signature: [redacted]

Date: 15. February.2025

Content

List of figures

List of tables

Symbols

$\mathrm{A_b}$ - surface area of the steel bar, (m^2)

$\mathrm{A_g}$ - surface area of the air gap, (m^2)

$\mathrm{A_m}$ - surface area of the magnet, (m^2)

$\mathrm{A_s}$ - surface area of the steel, (m^2)

$\mathbf{B}$ - magnetic flux density of materials in the FE model, (T)

$\mathrm{B_g}$ - magnetic flux density in the air gap, (T)

$\mathrm{B_r}$ - magnetic flux density at the magnet, (T)

$\mathrm{B_{rt}}$ - magnetic flux density of the single magnet, (T)

$\mathrm{B_s}$ - magnetic flux density at the steel, (T)

$\mathrm{D_{cut}}$ - depth of cut, (mm)

$\mathrm{d_g}$ - length of the air gap, (m)

E - Young's modulus of the material, (GPa)

$\mathbf{E}$ - electric field in the FE model, (V/m)

f - friction coefficient

$\mathbf{F}$ - magnetic force in the FE model, (N)

$\mathcal{F}$ - magnetomotive force, ($A \cdot t$)

$\mathrm{F_0}$ - reference force of coil cutting, (N)

$\mathrm{F_{cut}}$ - cutting force in the coil disassembly task (T.4), (N)

$\mathrm{F_{dis}}$- total disassembly force, (N)

$\mathrm{F_f}$ - frictional force, (N)

$\mathrm{F_i}$ - magnetic force on each magnet on the rotor, (N)

$\mathrm{F_{loss}}$- force loss during the press-fitted component disassembly process, (N)

$\mathrm{F_{px}}$ - unplugging force in the X direction, (N)

$\mathrm{F_{pz}}$ - unplugging force in the Z direction, (N)

$\mathrm{F_x}$ - magnetic force along the X direction, (N)

$\mathrm{F_{xt}}$ - magnetic force determined from the FT sensor using a single magnet in the test, (N)

$\mathrm{F_y}$ - magnetic force along the Y direction, (N)

$\mathrm{F_z}$ - magnetic force along the Z direction, (N)

$\mathrm{F_{Bx}}$ - resultant magnetic force on the rotor along the X direction, (N)

$\mathrm{F_{By}}$ - resultant magnetic force on the rotor along the Y direction, (N)

$\mathrm{F_{Bz}}$ - resultant magnetic force on the rotor along the Z direction, (N)

g - gravitational constant, 9.81 (m/s^2)

$\mathrm{g'}$ - effective air gap, (m)

$\mathbf{H}$ - magnetic strength of the material in the FE model, (KA/m)

$\mathrm{H_g}$ - magnetic strength at the air gap, (KA/m)

$\mathrm{H_s}$ - magnetic strength at the steel bar, (KA/m)

$\mathbf{I}$ – the identity 3-by-3 tensor (or matrix) in the FE model

i - number of magnets

$\mathrm{k_{cal}}$ - calculating factor for the magnetic forces

$\mathrm{L_b}$ - length of the steel bar, (m)

$\mathrm{L_c}$ - contact length of the press-fitted components, (mm)

$\mathrm{L_h}$ - length of the magnet holder, (m)

$\mathrm{L_m}$ - length of the magnet, (m)

$\mathbf{n}$ - surface normal of material in the FE model

$\mathbf{M}$ - magnetic intensity of the magnet in the FE model, (kA/m)

$\mathrm{M_0}$ - magnetic intensity of the magnet, (kA/m)

m - weight of the rotor, (kg)

$\mathrm{O'}$ - the origin after movement, (m)

$\mathrm{O'_x}$ - new X coordinate of the origin after movement, (m)

$\mathrm{O'_y}$ - new Y coordinate of the origin after movement, (m)

P - pressure applied on the contact surface in the pressure-fitted components, (Pa)

$\mathrm{P'_B}$ - new coordinate of the steel hub after movement, (m)

$\mathrm{P'_M}$ - new coordinate of the rotor after movement, (m)

$\mathbf{p}$ - air pressure in the FE model, (Pa)

r - radius of press-fitted components, (mm)

$\mathrm{R_{bi}}$ - inner radius of the steel hub, (m)

$\mathrm{R_{bo}}$ - outer radius of the steel hub, (m)

$\mathrm{R_{mi}}$ - inner radius of the magnet, (m)

$\mathrm{R_{mo}}$ - outer radius of the magnet, (m)

$\mathbf{T}$ - stress tensor of material in the FE model

$\mathrm{T_b}$ - thickness of the magnet, (m)

$\mathrm{T_h}$ - thickness of the magnet holder, (m)

$\mathrm{T_m}$ - thickness of the magnet, (m)

v - Poisson's ratio

$\mathrm{v_0}$ - robot initial cutting speed, (%)

$\mathrm{v_{cut}}$ - robot feeding speed, (%)

$\mathbf{V}_\mathrm{m}$ - magnetic scalar potential in the FE model, (A)

$\mathrm{v_{spin}}$ - spinning speed of the milling bit, (Rev/min)

$\mathrm{W_b}$ - width of the steel bar, (m)

$\mathrm{W_h}$ - width of the magnet holder, (m)

$\mathrm{W_m}$ - width of the magnet, (m)

x - position in the X direction, (m)

$\mathrm{x_0}$ - X coordinate of the original origin, (m)

$\mathrm{x'_0}$ - X coordinate of the new origin after movement, (m)

$\mathrm{x'_B}$ - X coordinate of the steel hub after movement, (m)

$\mathrm{x'_M}$ - X coordinate of the magnet after movement, (m)

$\mathrm{x_g}$ - air gap, (m)

y - position in the X direction, (m)

$\mathrm{y_0}$ - initial Y coordinate of the origin, (m)

$\mathrm{y'_0}$ - Y coordinate of the new origin after movement, (m)

$\mathrm{y'_B}$ - Y coordinate of the steel hub after movement, (m)

$\mathrm{y'_M}$ - Y coordinate of the magnet after movement, (m)

Z - interference value, (μm)

z - position in the Z direction, (m)

$\boldsymbol{\varepsilon_0}$ - permittivity in air in the FE model, (F/m)

Λ - permeance, (H)

$\boldsymbol{\mu}$ - permeability of the corresponding material in the FE model, (H/m)

μ_0 - permeability of vacuum, (H/m)

μ_f - dynamic frictional coefficient.

μ_{factor} - correction factor for the material magnetic permeability in the B-H region.

μ_{fitting} - permeability of the steel hub trained by the determined single magnet, (H/m)

μ_{air} - permeability of air, (H/m);

μ_{steel} - permeability of steel, (H/m);

$\mu_{r_{\mathrm{mag}}}$ - relative permeability of the magnet;

$\mu_{\mathrm{r\,air}}$ - relative permeability of air;

$\mu_{\mathrm{r\,steel}}$ - relative permeability of carbon steel;

θ - angle between the centre of the magnet and the centre of the steel bar, (°)

θ_d - deflection angle during the press-fitted component disassembly process, (°)

θ_M - angle of the cylindrical magnet, (°)

θ_{Mp} - angle between magnets, (°)

Abbreviations

BE – boundary element

EOL – End-of-Life

EV – Electric Vehicle

FE – Finite Element

FT – Force Torque

MMF – Magnetomotive Force

NdFeB – Neodymium Iron Boron.

PDE – Partial Differential Equations

PM – Permanent Magnet

RE – Rare Earth

SC – Schwartz Christoffel

TM – TechMan

UMPF – Unbalanced Magnetic Pulling Force

Chapter 1 Introduction

1.1 Background

Climate change, which significantly threatens human health, agricultural output, the environment and economies, has attracted much attention in recent decades. This is caused by the excessive emission of greenhouse gases from human activities, particularly deforestation and the burning of fossil fuels (Wuebbles, Fahey and Hibbard, n.d. and Pachauri *et al.*, 2014). To reduce environmental impacts, most countries have set net zero carbon policies to reduce the carbon dioxide emissions produced by human activities. The net zero carbon policy is defined as achieving a balance of the carbon dioxide produced by human activities and that removed from the atmosphere (Shubbar *et al.*, 2021). Major economies worldwide have set targets for net zero carbon, such as Germany by 2045; the USA, the UK, France, Japan, and South Korea by 2050; and China and Russia by 2060 (Climate Watch and Data-Driven EnviroLab, n.d.). Following this policy, the circular economy is one of the critical strategies in industry and is defined as a closed-loop system to extend the service life of materials for as long as possible (Hawken, Lovins and Lovins, 2013). The circular economy aims to eliminate waste and ensure the continual use of resources through principles such as reuse, repair, refurbishment, remanufacturing and recycling (MacArthur, 2013).

Remanufacturing is a process in which end-of-life (EOL) products are returned to at least their original condition, giving them a new lease of life while reducing raw materials, energy consumption and greenhouse gas emissions compared with manufacturing the same products anew (Kerin and Pham, 2019). The main processes in remanufacturing are product disassembly, component cleaning, component repair or replacement, product reassembly, and product testing (Kerin and Pham, 2020). Disassembly is thus the first element in a remanufacturing process chain. It is labour-intensive, as disassembly is difficult to automate. When it can be successfully implemented, robotic disassembly improves work efficiency (Liu *et al.*, 2020), reducing risks when dangerous products are involved.

The need to remanufacture EOL permanent magnet (PM) motors has increased in recent years because of their availability and the desire to avoid sending them to landfills. PM motors are commonly used in electric vehicles (EVs), the quantity of which will reach more than 120 million in 2039 (Casper and Sundin, 2021)The remanufacturing of PM motors enables the reuse of valuable components, such as rare earth magnets.

The remanufacturing of EOL motors has been investigated for the UK market, and the lack of an automatic disassembling process has been highlighted (Tiwari *et al.*, 2021). In China, the remanufacturing of Y-series AC induction motors has been shown to reduce energy consumption by 68.26%, raw material usage by 75.32%, and greenhouse gas emissions by 68.26% (Handong *et al.*, 2017). With respect to disassembly techniques, a flexible vision-based method was developed to find and remove screws in electric motors automatically (Mangold *et al.*, 2022), and a novel image-processing algorithm was proposed to enable a robot to detect screws and disassemble a motor (Bdiwi, Rashid and Putz, 2016). A sequence planning software platform was developed for the robotic disassembly of electric motors (Hansjosten and Fleischer, 2023), and the disassembly of a PM synchronous rotor was studied experimentally (Heim *et al.*, 2023).

To the best of the author's knowledge, there has been no systematic study of the electric motor disassembly process to determine the optimum disassembly strategy to minimise the efforts required and ensure the integrity of motor components. This thesis systematically investigates and analyses the tasks involved in disassembling permanent magnet (PM) motors and proposes effective solutions to address these challenges.

1.2 Problem analysis and research questions

This section analyses the configuration of a chosen electric motor as part of the initial inquiry into the motor disassembly process. Electric motors can be categorised based on their types of current use, working principles, or structural designs. Common examples include AC induction motors and DC brushless motors. In the disassembly process, the structure of motors can be classified into magnetless motors and permanent magnet motors. In magnetless motors, the rotor and stator are usually made of a nonmagnetic material. A typical example is squirrel cage induction motors, where the rotor is mainly made of aluminium or copper. Another example is the reluctance motor, where the rotor is made of coils. Thus, there is no magnetic field affecting the disassembly process of these magnetless motors. However, in permanent magnet DC brushless motors, the rotor is made of mainly magnetic materials, specifically NdFeB (neodymium iron boron). Those magnetic materials have very strong magnetic fields, causing large and unstable magnetic forces in the disassembly process. Large magnetic forces increase the difficulty of robotic disassembly.

This study selects a DC (permanent magnet) motor (model number: W5248GCF) for robotic disassembly. This type of motor is used in industrial electric fans and grass trimmers, adapting DC 58 V voltages, delivering 900 W of power and achieving a spinning speed of 2800 RPM. Regarding the structure of the permanent magnet DC brushless motor (Figure 1-1), a Bearing (large)

(A.2) and a Bearing (small) (D.1) are held in a Front cover (A.1) and End cover (D.2). A Stator case set (C.13) houses 12 sets of Coils (C.1 - C12). A Rotor set (B), which is made of neodymium magnets, is connected on the Bearing (large) (A.2) and Bearing (small) (D.1). 4 Screws (E.1–E.4) are fixed together with the End cover (D.2), Stator set (C.13) and Front cover (A.1).

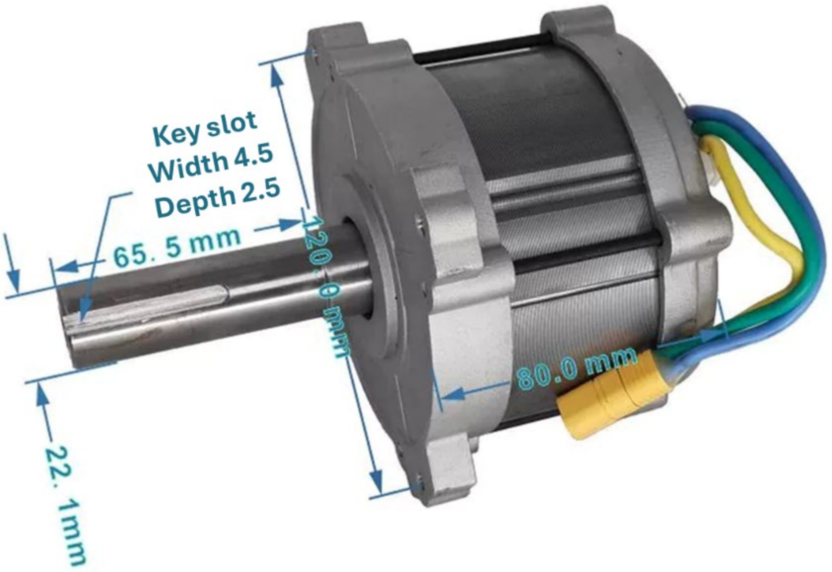

(a) A permanent magnet DC brushless motor in product view (Magnet DC motor, n.d.)

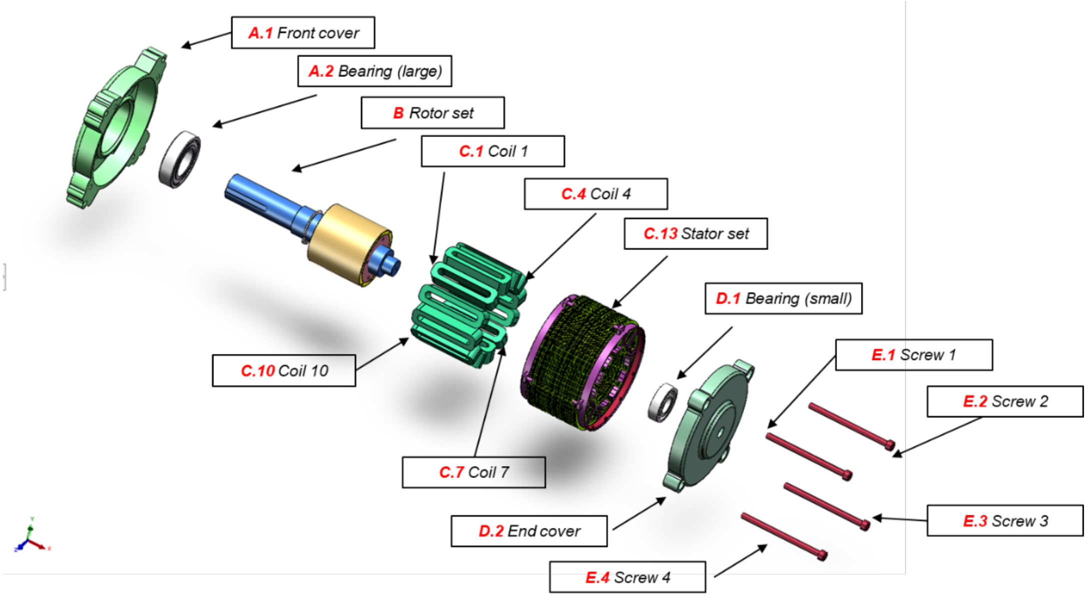

(b) Permanent magnet DC brushless motor in assembly view

Figure 1-1 Structure of a permanent magnet DC brushless motor (Magnet DC motor, n.d.).

The manual disassembly process is analysed on Table 1-1. The permanent magnet DC brushless motor is disassembled in 6 stages. Based on the analysis of the motor, disassembly tasks are classified as follows:

1. Press-in task (T.1): A component has interference fitted and hidden in the other component, where one of the components has very limited accessibility for disassembly. The Bearing (large) (A.2) is pressed into the Front cover (A.1), e.g., The Bearing (large) (A.2) is viewed in only one direction.

2. Press-on task (T.2): A component has interference fitted on the other component, where both components have good accessibility for

disassembly. For example, the Shaft of the Rotor set (B) is pressed onto the Front cover (A.1).

3. Unplugging task (T.3): This is a typical disassembly process for removing the Rotor set (B) with permanent magnets from the Stator set (C.13). However, enormous resistance to magnetic forces makes disassembly of the permanent magnet DC brushless motor difficult.

4. Coil disassembly task (T.4): This process refers to the removal of the copper Coils (C.1–C.12) from the Stator set (C.13).

5. Unscrewing task (T.5): This is the process of unfastening the Screws (E.1–E.4) or bolts on motors.

6. Pick-and-place task (T.6): This is a common process for removing components from the motor. The Front cover (A.1) is selected and removed from the Stator set (C.13).

Table 1-1 Manual disassembly sequence of the DC permanent magnet motor.

Stages	**Permanent magnet DC brushless motor**							
Start	A.1	A.2	B	C.1-12	C.13	D.1	D.2	E.1-4
Stage 1	A.1	A.2	B	C.1-12	C.13	D.1	D.2	E.1-4
Stage 2	A.1	A.2	B	C.1-12	C.13	D.1	D.2	E.1-4
Stage 3	A.1	A.2	B	C.1-12	C.13	D.1	D.2	E.1-4
Stage 4	A.1	A.2	B	C.1-12	C.13	D.1	D.2	E.1-4
Stage 5	A.1	A.2	B	C.1-12	C.13	D.1	D.2	E.1-4
Stage 6	A.1	A.2	B	C.1-12	C.13	D.1	D.2	E.1-4
Stage 7	A.1	A.2	B	C.1-12	C.13	D.1	D.2	E.1-4
End	A.1	A.2	B	C.1-12	C.13	D.1	D.2	E.1-4

In summary, problem analysis has reviewed different tasks in a permanent magnet DC brushless motor. Following these tasks, the following hypothesis is proposed:

“Robotic disassembly can be an alternative disassembly technique for permanent magnet DC brushless motor disassembly and reduces the total time in the disassembly process.”

To validate or refute this hypothesis, three research questions were subsequently examined in this study:

1. What are the impacts on the magnetic forces during the Unplugging tasks (T.3)?

2. How does robotic disassembly perform on a Press-fitted component (T.1 and T.2) and Coil disassembly (T.4)?

3. What are the constraints of robotic disassembly of electric motors?

1.3 Aim and objectives

This study aims to explore the robotic disassembly process for permanent magnetic electric motors. To achieve this aim, the objectives are as follows:

1. To study and model the influence of magnetic forces on the disassembly process (OB.1), address the Unplugging task (T.3);
2. To improve the model by using a data-driven method and to predict the optimised disassembly position (OB.2), address the Unplugging task (T.3);
3. To study and simulate how disassembly force affects the press-fit component disassembly process (OB.3), address the Press-in task (T.1) and Press-on task (T.2);
4. To examine key parameters and investigate an automatic solution (OB.4), address the Coil disassembly task (T.4);
5. To develop a robotic cell to automate the disassembly process for the selected permanent magnet DC brushless motor (OB.5).

1.4 Thesis outline

This thesis comprises seven chapters summarised as follows.

- Chapter 1 introduces the background of remanufacturing and robotic disassembly of the PM motor, analyses the structure of the selected PM DC brushless motor, raises hypotheses and research questions, and summarises the aim and objectives of this research.

- Chapter 2 reviews the literature concerning the manufacturing of electric motors and each disassembly task mentioned in section 1.2.

- Chapter 3 studies the problem of separating the rotor with permanent magnets from the stator, referred to as the Unplugging task (T.3). An analytical model, known as the magnetomotive force (MMF) model, and a finite element (FE) model are developed to evaluate magnetic forces in the separation process. The performances of both models are evaluated and compared with the experimental results.

- Chapter 4 studies the problem of unbalanced magnetic pulling force (UMPF) in the disassembly process and improves the accuracy of the developed MMF model by measuring the material permeability of the hub. The improved MMF model predicts the positions of the robot where the disassembly forces are minimised in the UMPF problem.

- Chapter 5 studies challenges for press-fit components, which are classified as Press-in tasks (T.1), Press-on tasks (T.2), and Coil disassembly tasks (T.4). Solutions associated with robotic disassembly are offered for these tasks.

- Chapter 6 describes the design of a robotic cell for DC magnetic electric motor disassembly. Differences and time efficiency between robotic disassembly and manual disassembly for this permanent magnet DC brushless motor are presented.

- Chapter 7 summarises the key findings of this thesis and suggests areas for further development.

Chapter 2 Literature review

2.1 Remanufacturing of electric motors

This section reviews the remanufacturing of electric motors in recent years. Remanufacturing is a broad term meaning a process in which EOL products are restored to at least their original condition, giving them a new lease of life while reducing raw materials, energy consumption and greenhouse gas emissions compared with manufacturing the same products anew (Kerin and Pham, 2019). The main processes in the remanufacturing of EOL electric motors include electric motor sorting, cleaning, condition testing, disassembly, repairing or replacement, reassembly, and product testing.

To understand the need for the remanufacturing of electric motors, Tiwari *et al.* (2021) comprehensively researched the circular economy of electric motors. They highlighted the growing demand for the remanufacturing of electric motors in the next few years, which aims to minimise material waste and energy consumption in the production of new electric motors. However, the challenges in remanufacturing are summarised as follows: (i) uncertainties in EOL electric motors, (ii) insufficient automation technologies and complex processes, and (iii) cost-effectiveness and investment considerations for remanufacturing. In terms of impacts on the environment, Handong *et al.* (2017) reported that remanufacturing electric motors results in an average reduction of 68.26% in energy consumption, 75.32% in material consumption and 68.26% in the emission of greenhouse gases in their study of remanufacturing Y-series motors in China. With respect to material savings, Li *et al.* (2021) reported a value composition for a permanent magnet synchronous motor, attributing 40% to copper products, 30% to magnetic materials, 20% to silicon steel sheets and 10% to manufacturing and other factors. They stated that the added value of remanufactured parts can be brought into full play by remanufacturing high-value parts, such as the stator, casing, end cover and shaft. Ihne *et al.* (2024) proposed that magnetic materials, specifically rare earth (RE) elements, such as neodymium iron boron (NdFeb) materials, are crucial strategic materials in the European industry. These materials are widely used in permanent magnet motors in electric vehicles (EVs); nevertheless, there is a lack of recycling or remanufacturing methods to reuse or recycle these materials from EOL EVs. Li *et al.* (2019) demonstrated the cost and energy savings of remanufacturing magnets from EOL EVs and reusing magnets on permanent magnet motors. They highlighted that automatic disassembly technologies for both EOL motors and magnets are underdeveloped at this stage. Similar studies on the recycling and reuse of magnets have been reported (Jin *et al.*, 2018; Nordelöf *et al.*, 2019; Kimiabeigi *et al.*, 2018 and Gonzalez *et al.*, 2018). To summarise these studies, the reuse of remanufactured magnets is promising; however, the disassembly process is one of the key challenges in removing magnets from EOL EVs. Therefore, these studies illustrate that the remanufacturing of EOL electric motors is not only environmentally beneficial and more cost-effective than the production of new electric motors but also supplies strategic RE magnetic materials to industry.

The author subsequently reviews the technical aspects of remanufacturing EOL electric motors. The most relevant studies of the disassembly of EOL electric motors were conducted by a German research team. Hansjosten and Fleischer (2023) developed a software platform for the robotic disassembly of electric motors. The software platform can identify the time-optimised path in the disassembly sequences and offers backup plans when problems stop robotic execution in the original sequence. Hansjosten, Baumgärtner and Fleischer (2024) developed a method for destructive disassembly of electric motors, which cut off the support structure on the front cover to reduce the disassembly time rather than unfastening the screws on the cover. However, the paper does not present the key parameters, such as the cutting force, feeding rate, tool spinning speed, etc. The author suggested that this method might not be the best for disassembling permanent magnet motors because the cutting chips might be attached to the magnets and are very difficult to remove because of magnetic forces. Heim *et al.* (2023) studied the removal of magnets from a rotor through several experiments. The magnets are pressed out from the rotor in serial tests to evaluate how disassembly forces perform across different sizes of magnets. A model of disassembly forces was developed based on the experiments. However, the key step of removing the rotor with permanent magnets from the stator set has not been studied in this paper. In addition, the disassembly capabilities of 5 different electric motors used on electric bicycles were studied by Erdmann *et al.* in 2023, who highlighted that the positioning and disconnection processes consume the majority of the disassembly time. The robot vision system helps with screw detection during EV electric motor disassembly (Bdiwi, Rashid and Putz, 2016). Furthermore, some studies have evaluated the performance of manufactured electric motors in production. The efficiency of an electric motor is enhanced to the IE4 level when the induction motor is replaced by an interior permanent magnet during remanufacturing (Ni *et al.*, 2016). The remanufacturing of an asynchronous motor, which replaces the original magnetless rotor with a permanent magnet rotor, results in more stable output performance, particularly in terms of torque, and saves 185 billion kilowatts of electricity power annually (Li *et al.*, 2022).

To the best of the authors' knowledge, work on the robotic disassembly of electric motors has not been studied systematically; however, this is a very important process in remanufacturing based on the literature review. There has been no systematic study of the disassembly process to determine the optimum disassembly strategy to minimise the efforts required and ensure the integrity of motor components. The author reviews the literature on each disassembly task.

2.2 Press-fit component disassembly (T.1 and T.2)

This section reviews press-fit component disassembly. The key issue is to study how the disassembly force changes in press-fit components. This review focuses on the methodologies for calculating the disassembly force. Huang *et al.* (2020) studied human-robot collaboration for the disassembly of press-fit components in 2020. In this study, the robot is tasked with picking and placing objects, and the hammer executes the disassembly of press-fit components on a hydraulic press by manually shaking the hydraulic pump. However, this paper lacks a methodology for modelling or calculating disassembly forces. A relative study by Xu, Pham and Su (2024) examined robotic disassembly solutions for twist-and-pull or twisting-pulling mechanisms in the press-fit components, presenting an analytic model and a FE method in ABAQUS software. This study proves that the twisting-pulling method reduces the average axial friction by approximately 32.53% compared with direct unplugging in press-fit component disassembly. Nevertheless, studies on the disassembly of press-fit components are very limited; thus, the author will look into methodologies related to the assembly of press-fit components.

However, unlike disassembly, the assembly of press-fit components has been well studied. The common methods for determining assembly force can be classified into analytical methods and numerical methods. In terms of the analytical method, initial research on a pin inserted into a hole was conducted by Goel in 1978). This study developed an analytic model for how radial forces affect pin-hole assembly. Qiu (2016) presented both an analytical method and an FE method for interference assembly for 3 rings, also referred to as multilayer thick-walled cylinders. The analytical method illustrated high accuracy and rapid calculation in early design, with an error rate of only 0.40% compared with the FE method in ABAQUS. The FE method requires time and high-performance equipment to achieve precise results in a detailed design. Wang *et al.* (2017) systematically studied analytical methods and FE methods to calculate the resistance force for press-fit components assembly, introducing a thick-walled cylinder theory to improve calculation accuracy. In 2018, Bai *et al.* (2018) studied the impacts of centrifugal forces and temperatures on an analytical model in a multilayer press-fit scenario.

One famous numerical method for the FE method is the finite element (FE) method. Sun *et al.* (2010) provided a detailed 3D FE method in Abaqus software in 2010. This study discusses (i) the optimisation of contact behaviours with different heating methods before the components are assembled, (ii) the effects on the interface during the assembly process, and (iii) the structural distortion after the assembly process. Kovan (2011) developed a detailed FE method in COMSOL Multiphysics for analysing the stress and separation frequencies of interference-fitted connections throughout all preferred diameter series. Golbakhshi, Namjoo and Mohammadi (2013) studied the impact of temperature on the assembly of press-fit components on a 3D FE model via SolidWorks software in 2013.

In summary, even if there are very few studies on press-fit component disassembly, the assembly of press-fit components has been well-developed in both analytical methods and FE methods in recent decades. The studies covered most areas in press-fit component assembly, including calculation of assembly forces, multilayer component conditions, effects of temperatures and material deformations, etc. These studies and methodologies will be applied to the development of press-fit component disassembly; therefore, the author will develop a model for both the Press-in task (T.1) and Press-on task (T.2) in Chapter 5.

2.3 Disassembly of magnetic materials (T.3)

This section reviews the disassembly of magnetic materials, typically removing the Rotor set (B) with permanent magnets from the Stator set (C.13). Unfortunately, few studies have investigated the robotic disassembly of magnetic materials. The author looks into 2 main aspects, including methodology for calculating for disassembly forces and effects from magnetic field distributions.

The mechanism for the disassembly force is dependent upon the magnetic force generated by magnetic materials. Thus, the author investigated methodologies for calculating magnetic forces. The computation of magnetic forces is a popular topic in electromagnetism. The main modelling techniques in electromagnetism can be classified as analytical or numerical. Maxwell’s equations, Poisson’s equation, the magnetic scalar potential, and the magnetic vector potential have been the fundamental tools used to generate analytical models in recent decades. Analytical modelling methods include equivalent circuit mapping, Schwartz Christoffel (SC) mapping, the harmonic method, the method of images and the surface charge and current model (Curti, Paulides and Lomonova, 2015). Most cases in which the analytic method has been applied involve motor rotation. These analytical methods have been used to model magnetic field distributions in rotating magnet machines (Ramakrishnan *et al.*, 2017). A motor model has been developed via the magnetomotive force

(MMF) method in the framework of equivalent circuit mapping (Zhu and Howe, 1993). Moreover, the main numerical tools employed in the study include the FE method and boundary element (BE) method. The FE and BE are used to solve Laplace's equation, which describes magnetic fields in space, and Poisson's equation, which shows how they behave in different materials (Jin *et al.*, 2018) (Gaul, Kögl and Wagner, 2013). Therefore, both analytical and numerical methods are well developed for modelling the magnetic force distribution for a rotor rotating inside a stator.

In terms of the effects of magnetic field distributions, the unbalanced magnetic pulling force (UMPF) problem, an ordinary problem arising from an uneven distribution of magnetic fields, refers to the effects of the magnetic field distribution in motor rotation scenarios. The conventional UMPF problem has been well developed in motor rotation scenarios over the past 2 decades. Related to the definition of this problem, Holehouse *et al.* (2014) defined the UMPF problem across 3 cases in a permanent magnet motor and resolved it via analytic models. This paper introduced uniform displacement, displacement at one end and opposite radial displacement in the UMPF problem. The UMPF problem affects motor spinning continuity and generates vibrations to damage bearings, hence reducing motor lifespan. Additionally, Abdi, Abdi and McMahon (2015) defined both static and dynamic models of motor rotation. Analytical methods and numerical methods are widely used to model this UMPF problem. On the one hand, Salah, Dorrell and Guo (2019) summarised motor faults, the percentage of faults, and fault monitoring and developed an analytical model for the UMPF problem caused by airgap eccentricity in induction motors. The analytic model is improved by using motor magnetic saturation and least squares approaches throughout the rotation process of a bearingless induction motor (Yang *et al.*, 2020). Finally, Li *et al.* (2022) proposed that the hybrid model of a nonlinear conformal mapping and reluctance network displays comparable accuracy to the FE model for addressing the UMPF problem in a surface-mounted permanent magnet motor. However, one of the drawbacks of employing analytic methods is the reduction in accuracy. On the other hand, related to the numerical model, the 2D FE method has proven effective in modelling the UMPF in a wound rotor induction machine (Dorrell and Kayani, 2014) and in a large hydrogenator (Abdi, Abdi and McMahon, 2015). Holehouse *et al.* (2014) demonstrated funding from both an analytic model and 2D/3D FE models in permanent magnet machines. Compared with the analytic method, the numerical method has superior accuracy. Nevertheless, the numerical method requires high-performance computing capabilities and is time-consuming in its calculations.

In summary, the effects of magnetic forces and distributions of magnetic fields in motor rotation have been well developed through both analytical and numerical methods; however, these 2 problems in motor disassembly have not been investigated until now. Fortunately, both analytical and numerical methods can be effectively employed to develop models for motor disassembly. The author discusses the Unplugging task (T.3) in detail in Chapters 3 and 4.

2.4 Coil disassembly (T.4)

The target of the coil disassembly task (T.4) is to remove copper Coil (C.1–C.12) from the Stator set (C.13). However, the author did not identify related papers about coil disassembly. A possible solution is that the copper coils might be cut off by robots. Thus, the author investigated the areas of robotic cutting and robotic milling; fortunately, this area is popular and has been well explored.

Several studies have evaluated developments in robotic cutting and milling and their challenges and trends. Bogue (2008) reviewed cutting techniques and their possible applications in robotics, including (1) water jets, (2) laser cutting, (3) ultrasonic cutting, (4) plasma cutting and (5) oxy-gas cutting. Chen and Dong (2013) reviewed the development of robot machining systems, including path planning for robotic machining, vibration and chatter analysis, vibration compensation, dynamic modelling and stiffness modelling. Wang *et al.* (2023) provided a comprehensive review of both traditional milling processes using CNC machines and robotic milling. The key benefits of robotic milling are (i) complete automatic processing, (ii) cost efficiency and (iii) flexibility in the milling process. However, the challenges are low stability and difficulties in developing dynamic models and milling trajectories. Zhu *et al.* (2022) recently reviewed the challenges, approaches and trends associated with the robotic milling process. The problems include offline process simulation and planning and online status monitoring and control.

In terms of studies of key parameters in robotic cutting and milling, Matsuoka *et al.* (1999) experimentally investigated essential parameters in robotic milling, such as (a) feed rate, (b) cutting force, (c) end milling capacity of the robot, (d) cutting surface conditions, (e) static stiffness, (f) structural dynamic characteristics, (g) cutting accuracy of the articulated robot and (h) forced vibration. Cordes, Hintze and Altintas (2019) developed an analytical model for cutting analysis by incorporating the traditional milling method into the dynamic control method. Their testing validated the model in both high-speed and low-speed milling of aluminium workpieces. Given the improvements in the qualities of robotic cutting and milling, 2 main areas of robotic configuration and stability are critical. With respect to the effects of robotic configuration and positioning, Vosniakos and Matsas (2010) focused on the key parameters of the initial pose of the robot and employed genetic algorithms to determine the optimal pose for robotic milling. Denkena and Lepper (2015) analysed errors in robotic positioning and developed a solution for tool deflection to compensate for these errors. Cen and Melkote (2017) studied the influences of robot dynamics on machining forces and suggested an optimal robot configuration (pose) and cutting conditions to improve the milling process according to the machining forces. Mousavi *et al.* (2018) explained the optimisation of robotic machining stability through robot configurations and the functional redundancy based on the chatter model.

With respect to machinery stability and vibration compensation during the robotic milling process, Huynh *et al.* (2020) studied a dynamic model for joint stiffness and damping parameters and experimented with the dynamic model on KUKA KR90 R3100. Zaeh and Roesch (2014) developed a method for compensating for static path deviation via a model-based fuzzy controller, and the model was validated on a KUKA KR 240 R2500 for robotic milling. Vibrations were analysed to improve quality in robotic milling via a KR500-3 6-DOF industrial robot (Nguyen, Johnson and Melkote, 2020). This work studied the relationships between the natural frequency and robot movements in the X, Y and Z directions and developed a model via Gaussian process regression (GPR) for suppressing vibrations. Hao *et al.* (2020) introduced experimental studies on the stability of robotic milling. The main outcome is the development of a regenerative chatter model to predict stability in high-speed milling. Guo, Zhang and Sun (2022) concentrated on improving the stability of a robotic milling system and developed a dynamic model for robotic control.

In summary, although the specific situation of Coil disassembly (T.4) has not yet been studied, robotic cutting and milling, as a potential technology for copper coil disassembly, has been well developed. Fortunately, most of the models developed for robotic cutting and milling require the detailed geometry of the tool. Nevertheless, the geometry of the cutting tool might be unclear in the coil disassembly task (T.4). This problem will be studied in Chapter 5.

2.5 Unscrewing process (T.5)

This section reviews the robotic unscrewing process, and a large amount of research has been conducted in this field. The main 2 research aspects can be defined as screw positioning and the robotic execution of unscrewing. With respect to screw positioning, the main research directions are vision systems and sensor-based systems. DiFilippo and Jouaneh (2018) introduced a study employing a designed sensor equipped with a screwdriver and a vision system of 2 webcams, one of which is installed over the robot and the other of which is fixed on the robot. Both systems achieve a 96.5% success rate in removing the screws from a laptop. A learning method is built into the vision system to increase accuracy. Liu *et al.* (2023) studied camera detection for structure damage to screws and developed a linear regression model as a solution for a two-stage detection framework. The initial stage includes screw extraction employing reflection features, and the second stage uses texture features to filter out false areas. Vision detection was developed by DiFilippo, Jouaneh and Jedson in 2024 via a neural network in YOLO-v5 for unfastening tasks on laptops. The key factors influencing the system's overall detection rate are systematically studied, including (a) the screw hole depth, (b) the presence of a taper in the screw hole, (c) the screw hole location, and (d) the colour difference between the laptop cover and the screw colour. Research from Foo, Kara and Pagnucco in 2021 focused on the identification of several types of screws via a deep learning model. Al Assadi *et al.* (2022) proposed a supervised learning strategy for identifying screw stripping on a screwdriver during the unscrewing process, whereby the bit or nut is inserted inside the screw drive.

In terms of robotic execution, an early research by Chen, Wegener and Dietrich in 2014 introduced a case of human robot collaboration in the unscrewing process using impedance control. Owing to the special design of the bit holder, the robot can use standard socket wrench bits. To address initial positional errors, Li *et al.* (2020) presented a spiral search strategy to align, locate, and engage a nut runner with a hexagon screwdriver. Rastegarpanah *et al.* (2021) achieved a 95% success rate on hexagonal nuts unscrewing by using a compliant robot. In a comprehensive study on the robotic unfastening process, Huang *et al.* (2021) introduced 3 typical failures: (1) screwdriver misalignment with the screw head, (2) screwdriver slipping on the screw head and (3) screws being too tight to be removed. This paper offered strategic solutions for secondary trials of searching and unfastening attempts when failures occurred in the first trial. This strategy achieved a 100% successful operation rate. Learning methods can improve the success rate and optimise robotic actions. Zhou *et al.* (2022) focused on improving the efficiency and safety of human-robot collaboration during the unscrewing process and employed an innovative

PSO–Pareto algorithm. Peng *et al.* (2024) investigated the optimisation of the robotic unscrewing method via reinforcement deep learning, improving the precision of screw location and the success rate of the unfastening process.

In summary, Unscrewing tasks (T.4) have been well developed in terms of positioning and robotic disassembly execution. The technologies are able to achieve a very high success rate for the unscrewing task. The author suggested that existing methods and models might effectively achieve the unscrewing task in motor disassembly, making the development of new methods and models unnecessary.

2.6 Pick and place (T.6)

This section focuses on the literature regarding robotic pick-and-place operations. Overall, this area has been well developed in recent years. With respect to the background of robotic pick and place operations, Surati *et al.* (2021) reviewed robotic pick and place tasks in industry, including robot types, artificial intelligence, object recognition and controllers. Lobbezoo, Qian and Kwon (2021) and Lobbezoo and Kwon (2023) reviewed the application of reinforcement learning in robotic pick and place operations and analysed key factors for reinforcement learning. These two papers claimed that generalising the training samples could make the pick and place task more widely applicable.

Furthermore, vision systems are widely used for identification and positioning in robotic pick and place operations. Kotthauser and Mauer (2009) developed a vision-based system for identification and positioning in robotic pick and place operations. Kumar *et al.* (2014) focused on feature extraction and classification in a vision system applied during robotic pick and place operations. They achieved 99.33% classification accuracy and 83.64% feature extraction accuracy. Andhare and Rawat (2016) developed a method to determine the x and y coordinates of an object within a vision system for robotic pick and place operation. The vision system also helps to improve safety in human-robot collaboration (Kotthauser and Mauer, 2009).

With respect to robotic pick and place applications, Jørgensen *et al.* (2019) designed an adaptive robotic system for handling deformable objects, employing 3D light scanning and a vacuum gripper. Myint and Htun (2016) designed a robot equipped with a gripper for pick and place tasks via an inverse kinematic model. Borrell Méndez *et al.* (2020) applied robotic pick and place operations in the footwear industry; they built a vision-based system to identify different pieces of footwear and developed a decision-making model to generate a time-optimised sequence. To minimise the operation time, Perumaal and Jawahar (2013) developed a mathematical model to generate a robotic path for pick and place operations. Unlike the optimisation of path planning above, a method for optimising the energy consumption of robotic systems was developed by parametrising motors and prescheduled trajectories with action constraints (Pellicciari *et al.*, 2013). Recently, a learning-based model has been applied to this operation. Gomes *et al.* (2022) applied a reinforcement learning method on a cobot for picking untrained objects and achieved an 89.9% success rate of grasping.

In summary, this area has been well developed, in which vision systems improve the success rate of the robotic unscrewing process, and a learning-based model helps to adapt a wide range of objects in robotic pick and place operations. The author suggested that the robot-trained method can be easily applied to robotic pick and place operations in motor disassembly, making further research or development in this field unnecessary.

Chapter 3 Model of electric magnet motor disassembly

3.1 Problem description

Given the importance and value of magnetic materials, the author studied the Unplugging task (T.3), which involves removing the Rotor set (B) with permanent magnets from the Stator set (C.13) (Figure 3-1).

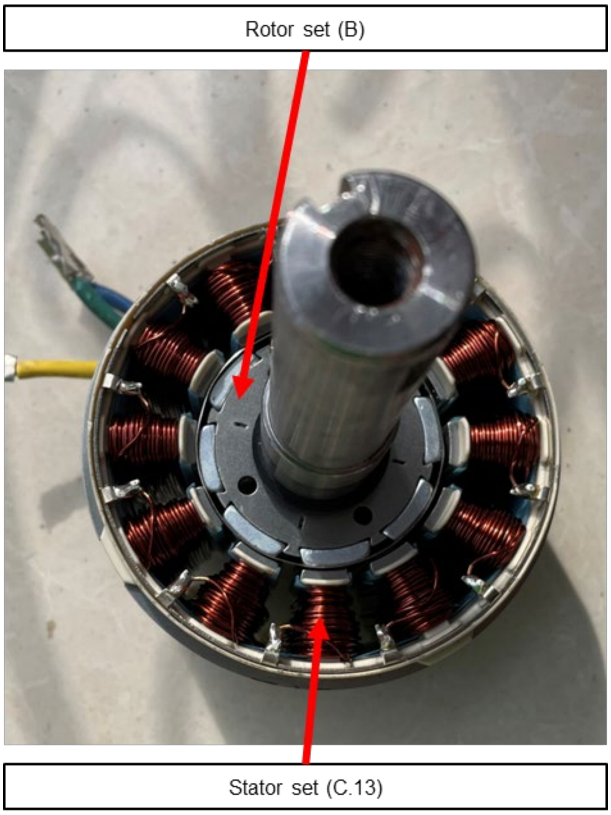

Figure 3-1 Unplugging task (T.3): Removal of the Roter set (B) from the Stator set (C.13).

The separation of the rotor and stator when disassembling PM motors can be simplified as the problem of removing a cylindrical peg from a cylindrical hole in the presence of a magnetic field. During disassembly, the peg may not be in contact with the hole, or it may touch the hole at one point or two points or along a line (Figure 3-2) (Zhang *et al.*, 2019). Disassembly can fail because of jamming and wedging, which only take place under two-point contact conditions (contact state (c) in Figure 3-2).

Jamming occurs when the peg cannot move because of incorrectly applied forces and moments. Wedging involves the peg becoming stuck at a position because high internal forces within the peg keep it in static balance regardless of the external force. Wedging can occur only when the peg or the hole can deform elastically and when the clearance between the peg and the hole is sufficiently small relative to its diameter (Pham, 1982).

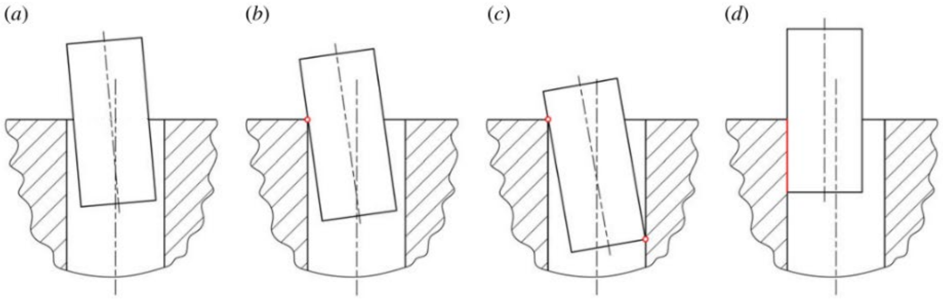

Figure 3-2 Peg-hole contact conditions: (a) no contact, (b) one-point contact, (c) two-point contact and (d) line contact (Zhang et al., 2019).

The ideal state during disassembly is that of having no contact between the peg and the hole, as there are no contact forces to cause damage. In the case of a rotor and stator, this is difficult to achieve because of the permeant magnetic forces that tend to cause the rotor to attach itself to the stator. Contact states (b), (c) and (d) in Figure 3-2 are therefore likely to occur, with contact state (d), the worst-case, being the most likely.

In the ideal state of no contact, the rotor levitates at the centre of the stator once both end bearings are removed. This would be possible if the magnetic fields at the poles were equal and if the rotors were perfectly symmetrical. However, the magnetic fields are normally unbalanced, and the rotor geometry is imperfect. Therefore, without external intervention, the rotor will attach itself fully to the stator after the removal of the end bearings, which explains the high likelihood of the line contact state (Figure 3-2 (d)).

The contact state (d) is to be avoided because both the rotor and the stator can be damaged during disassembly. The strong magnetic attractive forces between the rotor and stator generate high frictional resistance, causing excessive scoring and wear on the contact surfaces. This is also an issue with contact states (b) and (c). Scenario (c) is worse than scenario (b) because it provides the necessary conditions for jamming and wedging, although wedging is unlikely because the clearance between the rotor and stator is on the order of 0.7–1.5 mm, which is large for a 50–60 mm-diameter rotor.

This work aims to facilitate an ideal disassembly process where the rotor can be removed under contactless conditions to prevent damage. The next section describes the modelling of the forces acting on the rotor, the purpose of which is to direct a robot to pull the rotor away without the latter touching the stator.

3.2 Methodology

3.2.1 Overall force analysis

In the following analysis, for simplicity, slot structures are neglected, and the rotor and stator are assumed to be smooth cylinders. The rotor axis and stator axis are kept parallel throughout. Otherwise, contact state (c) will occur, incurring the risk of jamming. The disassembly force F_{dis} comprises two components, F_{px} and F_{pz} (Eq. 3.1). Under line contact conditions (Figure 3-3 (a)), F_{px} and F_{pz} are given by Eq. 3.2 and Eq. 3.3, respectively, where F_{Bx} and F_{Bz} are the x- and z-components of the resultant magnetic force F_B on the rotor, mg is the weight of the rotor, and F_f is the friction force on the rotor due to F_{Bx}. F_f is given by Eq. 3.4, where μ_f denotes the dynamic coefficient of friction between the rotor and stator. The same equations apply under no-contact conditions, except that F_f is now zero (Figure 3-3 (b)).

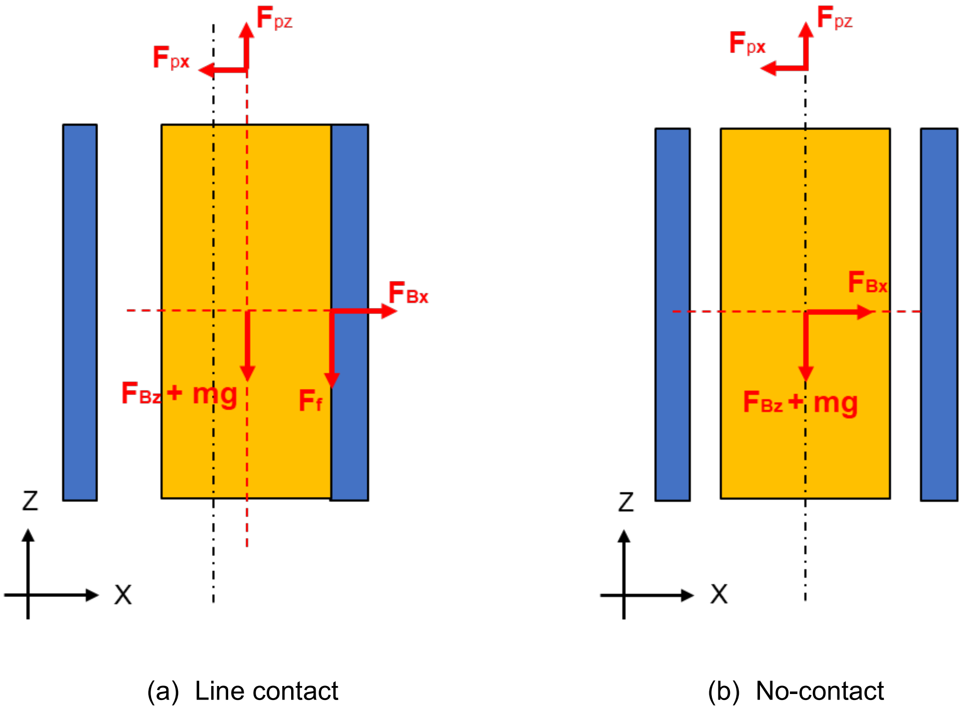

(a) Line contact (b) No-contact

Figure 3-3 Force analysis under line contact and no-contact conditions.

$$F_{dis} = -\sqrt{{F_{pz}}^2 + {F_{px}}^2} \tag{3.1}$$

$$F_{px} = -(F_{Bx}) \tag{3.2}$$

$$F_{pz} = -(F_{Bz} + F_f + mg) \tag{3.3}$$

$$F_f = \mu_f F_{Bx} \tag{3.4}$$

The key to obtaining the total disassembly force is to determine the magnetic forces FB, which is the subject of the next section.

3.2.2 Determination of magnetic forces via the MMF method

The MMF method (Zhu and Howe, 1993) was chosen over the magnetic scalar potential method (Engel-Herbert and Hesjedal, 2005) because it is simpler and yields more accurate results. This is because the latter method requires the solution of 3D integral equations and produces large errors associated with divisions by small numbers, given the small distances involved (the gap between the rotor and the stator being less than a millimetre).

The MMF method was used first to model the magnetic force between a single bar magnet and a parallel steel bar. The result obtained was then integrated to provide the force between a rotor comprising several bar magnets circumferentially positioned on a circular hub and a concentric steel cylinder representing the stator. It is assumed that the relative movement of the rotor and the hub is slow and that magnetostatic conditions apply. Lenz's Law could therefore be neglected.

3.2.2.1 Force between a bar magnet and a parallel steel bar

Both the magnet and the steel bar are modelled as consisting of points. For the magnet, the points are magnetic point sources. Referring to Figure 3-4, the magnet (the green part) and its holder (the orange part) move along the X and Z directions relative to the steel bar (the blue part). The magnetic flux diffuses from the point source (B_r) in the magnet (Eq. 3.5) (Zhu and Howe, 1993) through air (B_g) (Eq. 3.6) (Zhu and Howe, 1993) into the steel bar (B_s) (Eq. 3.10), resulting in magnetic forces in the X direction (F_x) (Eq. 3.11) and Z direction (F_z) (Eq. 3.12) on the steel bar. The magnetic flux (B_r) can be determined on the surface of the magnets via a Gauss meter.

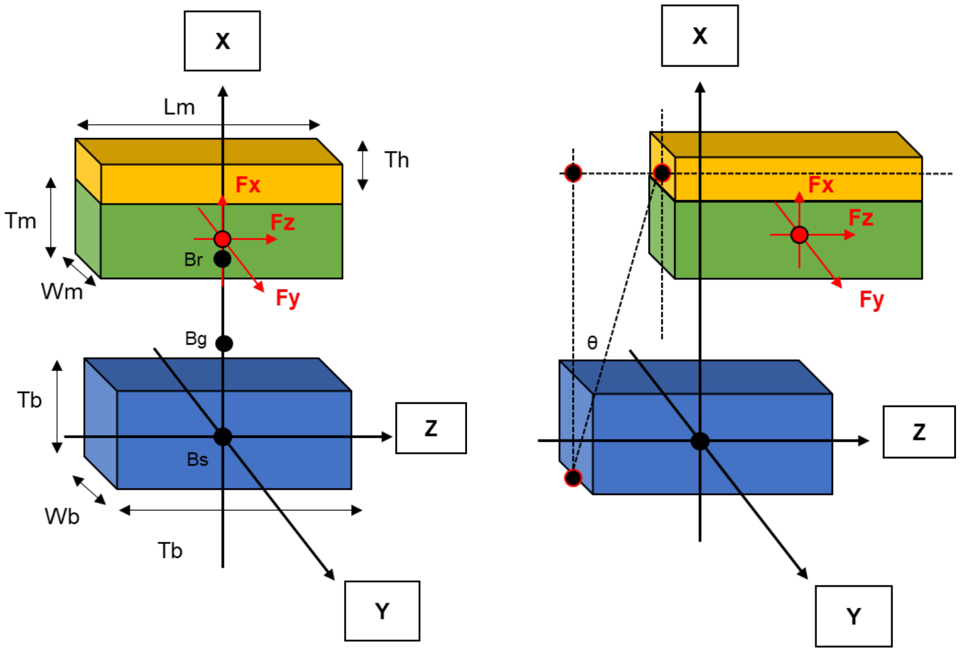

(a) magnet moves in X direction (b) magnet moves in Z direction

Figure 3-4 Single magnet and single steel bar problem.

$$|M_0| = \frac{B_r}{\mu_0 \mu_{r_{mag}}} \tag{3.5}$$

where μ_0 is the magnetic permeability in vacuum, $\mu_{r_{mag}}$ is the relative magnetic permeability of the magnet and M_0 is the magnetisation of the magnet. Both the magnetic north pole and south pole exert attractive forces on magnetic materials such as steel. Thus, the absolute value of magnetisation is used to simplify the calculations.

$$\mathrm{B_g(x,z)} = \frac{\mathcal{F} * \Lambda}{\mathrm{A}} = \frac{(|\mathrm{M_0}|\mathrm{T_m}) * \left(\frac{\mu_0}{\mathrm{g'(x,z)}}\right)}{\mathrm{A}}$$

$$= \left(\frac{\mathrm{B_r}}{\mu_0 \mu_{\mathrm{r_{mag}}}} \mathrm{T_m}\right) * \left(\frac{\mu_0}{\mathrm{d_g(z)} + \frac{\mathrm{T_m}}{\mu_{\mathrm{r_{mag}}}}}\right) \left(\frac{\mathrm{A_m(x)}}{\mathrm{A_g(x)}}\right) = \left(\frac{\mathrm{B_r}}{1 + \frac{\mu_{\mathrm{r_{mag}}} \mathrm{d_g(z)}}{\mathrm{T_m}}}\right) \left(\frac{\mathrm{A_m(x)}}{\mathrm{A_g(x)}}\right) \tag{3.6}$$

$$= \left(\frac{\mathrm{B_r}}{\mathrm{d_g(z)} + \frac{\mathrm{T_m}}{\mu_{\mathrm{r_{mag}}}}}\right) \left(\frac{\mathrm{T_m}}{\mu_{\mathrm{r_{mag}}}}\right) \left(\frac{\mathrm{A_m(x)}}{\mathrm{A_g(x)}}\right)$$

where $\mathrm{B_g(x,z)}$ is the magnetic flux density related to the position of the magnet in the X direction and Z direction in the air gap. $\mathcal{F}$ represents the MMF to determine magnetic source from the magnet and Λ is the permeance, describing how magnetic field transferring in the airgap (Eq. 3.6). Both equations are fundamental in the Magnetostatic (Zhu and Howe, 1993). $\mathrm{g'}$ is the effective airgap, considering the thickness of the magnet ($\mathrm{T_m}$) and the airgap with the magnet located at x $\mathrm{d_g(x)}$. $\mathrm{A_b}$ and $\mathrm{A_m}$ represent the areas of the steel bar (Eq. 3.7) and the magnet (Eq. 3.8), respectively. $\mathrm{A_m}$ is assumed to be the same as the area of the air gap $\mathrm{A_g}$. These areas change, depending on the position of the magnet in the Z direction. $\mathrm{L_b}$ and $\mathrm{L_m}$ represent the lengths of the steel bar and the magnet, respectively. $\mathrm{W_b}$ and $\mathrm{W_m}$ represent the widths of the steel bar and the magnet, respectively.

$$\mathrm{A_b(z)} = (\mathrm{L_b} - |\mathrm{z}|) * \mathrm{W_b} \tag{3.7}$$

$$\mathrm{A_m(z)} = (\mathrm{L_m} - |\mathrm{z}|) * \mathrm{W_m} \tag{3.8}$$

$$H_g(x,z) = \frac{B_g(x,z)}{\mu_{air}} = \frac{B_g(x,z)}{\mu_0 \mu_{r_{air}}} \quad (3.9)$$

$$B_s(x,z) = 0.2811 * \log(H_g(x,z)) + 0.2561 \quad (3.10)$$

where H_g is the external magnetic strength in the air gap. $\mu_{air} = \mu_0 \mu_{r_{air}}$ is the magnetic permeability of air. The magnetic hysteresis B–H curve is used to model how steel components react to magnetic fields. The steel bar used in the experiment was made of S235 grade carbon steel, but its B–H curve was not available to the author. The B–H curve for 1018 low-carbon steel from COMSOL Multiphysics 5.6 software, a similar material, was used instead (Eq. 3.10). A correction factor (μ_{factor}) was added to adjust the magnetic permeability of the material in the B-H region. μ_{factor} was determined by considering the difference between the magnetic force calculated via the MMF model and that experimentally determined. The force F_B is given by Eq. 3.11 and Eq. 3.12:

$$F_{Bx}(x,z) = -\frac{B_g(z)^2 A_b(x)}{2\frac{B_s(x,z)}{H_g(x,z) * \mu_{factor}}} \quad (3.11)$$

$$F_{Bz}(x,z) = F_{Bx}(x,z) * \tan\theta\,(x,z) \quad (3.12)$$

where

$$\tan\theta\,(x,z) = \frac{z}{d_g(x) + T_m + T_b + \frac{T_h}{2}} \quad (3.13)$$

where F_{Bx} and F_{Bz} represent the resultant magnetic forces in the X direction and Z direction, respectively. T_B, T_m and T_h are the thicknesses of the steel bar, the magnet, and the magnet holder, respectively.

3.2.2.2 Force between a cylindrical rotor assembly and a cylindrical steel hub

The above method was extended to the case where the rotor was made up of four bar magnets equidistantly positioned around a cylindrical holder as one common structure of a PM rotor (Ocak, 2018). This rotor assembly was able to move axially (along the Z direction in Figure 3-5 (a)) and, to a limited degree, radially inside a cylindrical steel hub (along the X and Y directions in Figure 3-5 (b)). The hub represents the stator. The equations describing the relative position between points on the magnets and corresponding points on the hub are given in Appendix A.

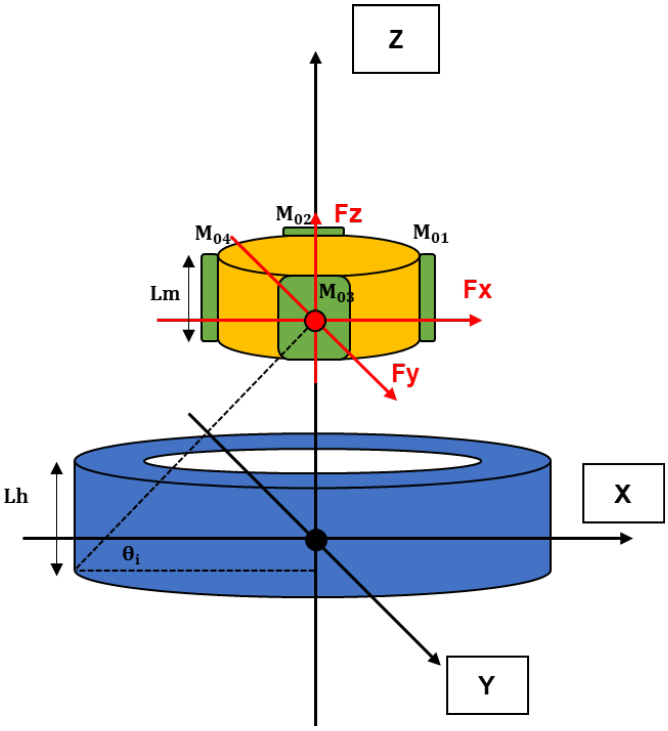

(a) 3D view

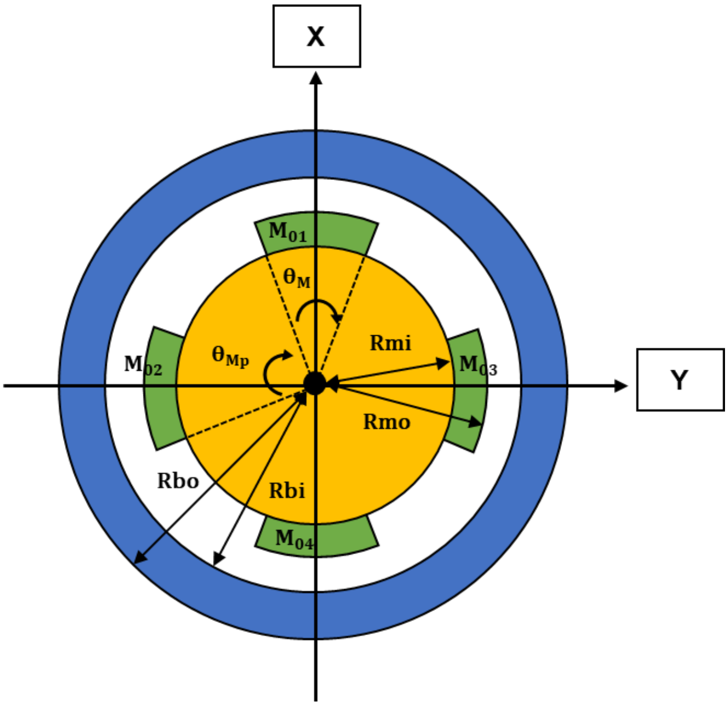

(b) top view

Figure 3-5 Cylindrical rotor and hub.

Similar to the previous case, the resultant magnetic forces in the X, Y and Z directions (F_{Bx}, F_{By} and F_{Bz}) can be calculated (Eqs. 3.14–3.26) (Zhu and Howe, 1993).

$$|M_0(i)| = \frac{B_r(i)}{\mu_0 \mu_{r_{mag}}} \tag{3.14}$$

$$B_g(i,x,y,z) = \left(\frac{B_r(i)}{\left|d_g(i,x,y)\right| + \frac{T_m(i)}{\mu_{r_{mag}}}} \right) \left(\frac{T_m(i)}{\mu_{r_{mag}}} \right) \left(\frac{A_m(i,z)}{A_g(i,z)} \right) \tag{3.15}$$

$$A_b(i,z) = (L_b(i) - |z|) * W_b(i) * \left(\frac{R_{bi} * \pi * \theta_M(i)}{180} \right) \tag{3.16}$$

$$A_m(i,z) = (L_m(i) - |z|) * W_m(i) * \left(\frac{R_{mi} * \pi * \theta_M(i)}{180} \right) \tag{3.17}$$

$$H_g(i,x,y,z) = \frac{B_g(i,x,y,z)}{\mu_{air}} = \frac{B_g(i,x,y,z)}{\mu_0 \mu_{r_{air}}} \tag{3.18}$$

$$B_s(i,x,y,z) = 0.2811 * \log(H_g(i,x,y,z)) + 0.2561 \tag{3.19}$$

$$F_{Bx} = F_{x1} - F_{x4} \tag{3.20}$$

$$F_{By} = F_{y3} - F_{y2} \tag{3.21}$$

$$F_z(i,x,y,z) = F_x(i) * \tan\theta\,(i,x,y,z) + \ F_y(i) * \tan\theta\,(i,x,y,z) \tag{3.22}$$

$$\tan\theta\,(i,x,y,z) = \frac{z}{d_g(i,x,y) + T_m(i) + T_b(i) + \frac{T_h}{2}} \tag{3.23}$$

$$T_m(i) = R_{mo}(i) - R_{mi}(i) \tag{3.24}$$

$$T_b(i) = R_{bo}(i) - R_{bi}(i) \tag{3.25}$$

$$F_{Bz} = \sum_{i=1}^{i=4} F_z(i) \tag{3.26}$$

3.2.3 **Determination of magnetic forces via the finite element method**

The problem of determining the forces on the magnetised rotor shown in Figure 3-5 can be described by partial differential equations (PDEs). As the movement of the rotor is slow, the problem is a magnetostatic problem, and it is possible to consider only the magnetic forces in the FE model. The governing equations demonstrate how the magnetic flux transfers from the magnets (point sources), though the airgap, to the steel hub and produces magnetic forces on the hub (Kovetz, 2000):

$$\boldsymbol{\nabla} \cdot \mathbf{B} = 0 \tag{3.27}$$

$$\mathbf{H} = -\nabla \cdot \mathbf{V_m} \tag{3.28}$$

$$\mathbf{B_1 n_1} = \mathbf{B_2 n_2} \tag{3.29}$$

$$\mathbf{B} = \begin{cases} \mu_0(\mathbf{H} + \mathbf{M})\,, & \text{in the magnet} \\ \boldsymbol{\mu}\mathbf{H}\,, & \text{in the airgap} \\ \mathrm{f}(\|\,\mathbf{H}\,\|)\dfrac{\mathbf{H}}{\|\,\mathbf{H}\,\|}, & \text{in the steel hub} \end{cases} \tag{3.30}$$

$$\mathbf{F} = \oint_{\partial\Omega_1} \mathbf{n_1 T_2}\,\mathrm{dS} \tag{3.31}$$

$$\mathbf{T_2} = -\mathbf{pI} - \left(\frac{\boldsymbol{\varepsilon_0}}{2}\mathbf{E}\cdot\mathbf{E} + \frac{1}{2\mu_0}\mathbf{B}\cdot\mathbf{B}\right)\mathbf{I} + \boldsymbol{\varepsilon_0}\mathbf{EE^T} + \frac{1}{\mu_0}\mathbf{BB^T} \tag{3.32}$$

Eq. 3.27 and Eq. 3.28 are basic equations in magnetostatics, where $\mathbf{B}$ is the magnetic flux density; $\mathbf{H}$ is the external magnetic strength; and $\mathbf{V_m}$ is the magnetic scalar potential. The transfer of magnetic fields between different materials is described by Eq. 3.29, where $\mathbf{n}$ is the surface normal of the materials. Eq. 3.30 gives the magnetisation models of the magnet, air and steel hub, where $\boldsymbol{\mu}$ is a matrix representing the magnetic permeability of the corresponding material. To calculate the magnetisation of the steel hub, the external magnetic strength $(\mathbf{H})$ is expressed as a function of the Magnetic flux density $\mathbf{B}$, where the unit vector $(\frac{\mathbf{H}}{\|\mathbf{H}\|})$ gives the direction of the magnetic strength $(\mathbf{H})$. Eq. 3.31 yields the magnetic force $(\mathbf{F})$ on the steel hub, where $\mathbf{n_1}$ is the surface normal of the hub and $\mathbf{T_2}$ is the stress tensor of the surrounding air. The stress tensor of the surrounding air $(\mathbf{T_2})$ is shown by Eq. 3.32, where $\mathbf{p}$ is the air pressure, which is 0 in vacuum; $\mathbf{I}$ is the 3-by-3 identity matrix. $\mathbf{E}$ is the electric field, which is 0 in the current free model, and $\boldsymbol{\varepsilon}_\mathbf{0}$ is the permittivity in air.

The FE method implemented in COMSOL Multiphysics 5.6 software was used to solve the above set of PDEs. The mesh sensitivity was tested to balance the accuracy of the results and the computational time. The following setting was adopted: a 0.5 mm triangular mesh was used on the surfaces of the magnets and the inner surface of the steel hub, and a triangular mesh in the range of 0.209–4.87 mm controlled by COMSOL software was employed for the remaining components (Figure 3-6 (b)). The boundary of the air domain ((i) in Figure 3-6 (a)) was set to reduce the calculation time. The magnetic flux density of each magnet was measured by a Gauss meter. As in the case of the analytical models, the B–H curve was also used to model how steel components react to a magnetic field. All the parameters (Table 3-1) were built in COMSOL via a laptop with an Intel i7 10th generation processor, an RTX 2070MQ GPU and 32 GB of RAM.

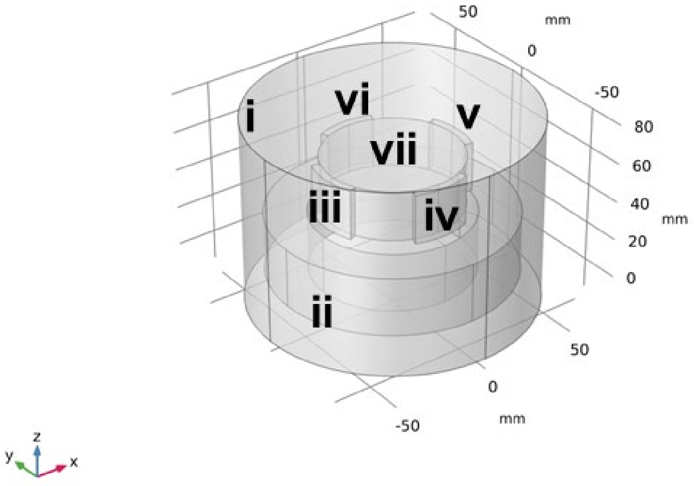

(a) geometry: (i) air domain, (ii) steel hub, (iii) – (vi) magnets (M01, M02, M03 and M04) and (vii) magnet holder

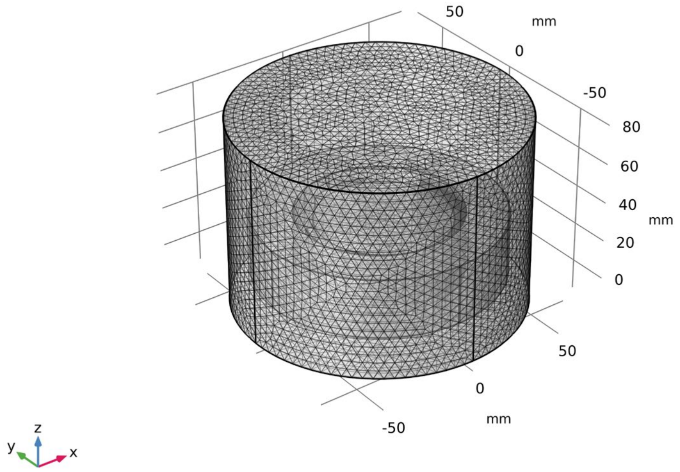

(b) mesh

Figure 3-6 FE model of the cylindrical rotor-stator problem.

3.3 Experiment

Experiments were conducted to validate the MMF and FE methods as applied to the cylindrical rotor-stator problem. The experimental setup is shown in Figure 3-7. The movement of the rotor was controlled by a Staubli TX90L collaborative robot arm with a touch-sensitive cover, and the steel components were fixed on a table. The magnetic forces between the magnet and the steel hub were determined at different positions via an ATI 'Theta' force/torque (FT) sensor fixed on the table. The magnetic flux density of the magnets is measured by a Gauss meter (Model: San Liang TS200). Static measurements were taken in the experiments; thus, Lenz's law can be neglected. Each experiment was repeated 3 times, and 300 data points were recorded for each position of the rotor. Table 3-1 lists all the parameters for the problem.

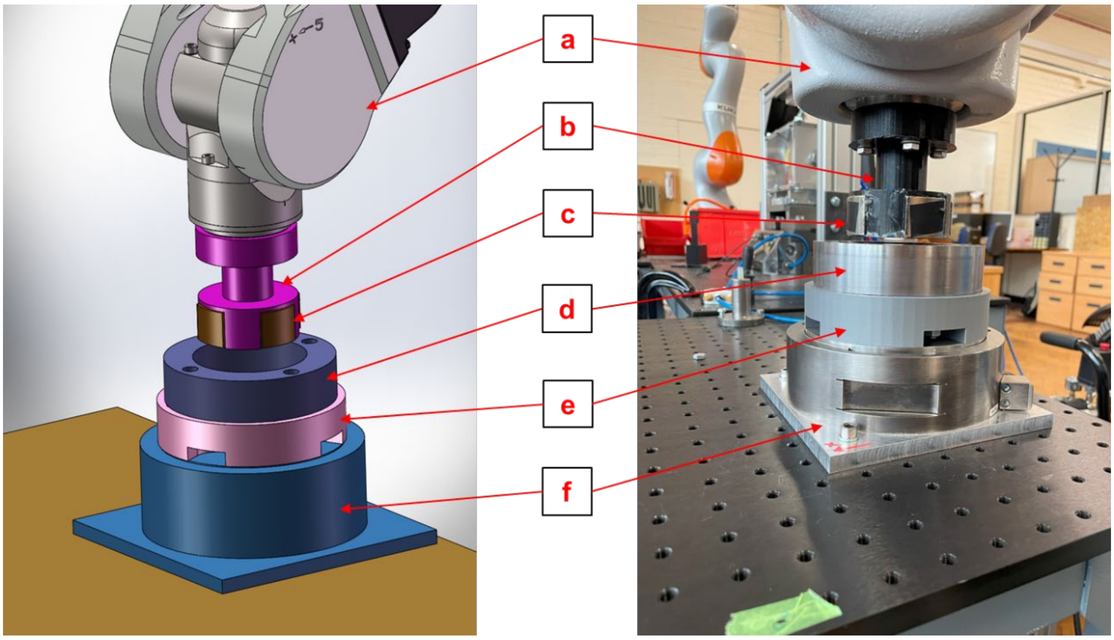

Figure 3-7 Experimental setup for the cylindrical rotor-stator problem: (a) Staubli TX90L Touch (robot), (b) magnet holder, (c) magnets, (d) steel hub, (d) holder of the steel hub and (f) ATI

Theta (FT sensor). Both the magnet holder and the holder of the steel hub were made of plastic, which did not affect the magnetic force.

Table 3-1 Parameters of the cylindrical rotor-stator problem.

No	Parameters	Symbol	Values	Unit
1	Magnetisation of magnet 1	M_{01}	-163.50	kA/m
2	Magnetisation of magnet 2	M_{02}	162.24	kA/m
3	Magnetisation of magnet 3	M_{03}	164.92	kA/m
4	Magnetisation of magnet 4	M_{04}	-174.40	kA/m
5	Length of the steel hub	L_b	30	mm
6	Length of the magnet holder	L_h	25	mm
7	Length of the magnet	L_m	25	mm
8	Inner radius of the steel hub	R_{bi}	39.5	mm
9	Outer radius of the steel hub	R_{bo}	59.5	mm
10	Radius of the magnet holder	R_h	33.5	mm
11	Inner radius of the magnet	R_{mi}	33.5	mm
12	Outer radius of the magnet	R_{mo}	37.5	mm
13	Angle between magnets	θ_{Mp}	90	Degree
14	Angle of cylindrical magnet	θ_M	45	Degree
15	Weight of the magnets and the holder	m	0.327	kg
16	Dynamic friction coefficient between the magnet and the hub	μ_f	0.42	-
17	Calculating factor for correcting the material magnetic permeability in the B-H region	μ_{factor}	100	-
18	Magnetic permeability of vacuum	μ_0	$4\pi 10^{-7}$	H/m

3.4 Results

Figure 3-8 shows the magnetic forces and disassembly force at different rotor positions. The X movement range X (-1.5 to 1.5 mm) and Y movement range (-1.3 to 1.3 mm) are different because of the imperfect structure of the magnet holder in the experiment. The magnetic forces experienced in the positive positions (i.e., X = 0 to 1.5 mm; Y = 0 to 1.3 mm) and negative directions (i.e., X = 0 to -1.5 mm; Y = 0 to -1.3 mm) are caused by the different magnetic fields from magnets (Figure 3-8 (a) and (b)). For movements in the X-Y plane (i.e., the radial plane), with the rotor located inside the stator (at Z = 0 mm), the forces obtained via the FE and MMF methods agree well with those determined experimentally (Figure 3-8 (a) and (b)). The average error rates of the FE method and MMF method are 16.7% and 26.3 %, respectively. The FE method performed better when the rotor was moved along the Z direction (i.e., the axial direction) (Figure 3-8 (c)). However, it is difficult to determine the magnetic forces accurately via the MMF method when the magnet is located near the top of the steel hub (Z ≈ 30 mm), where the magnetic flux concentrates at the corner of the magnet (Figure 3-8 (c) and (e)). As shown in Figure 3-10 (f), the FE method can address this corner effect. Figure 3-8 also shows that the peak magnetic forces obtained via the two methods are similar.

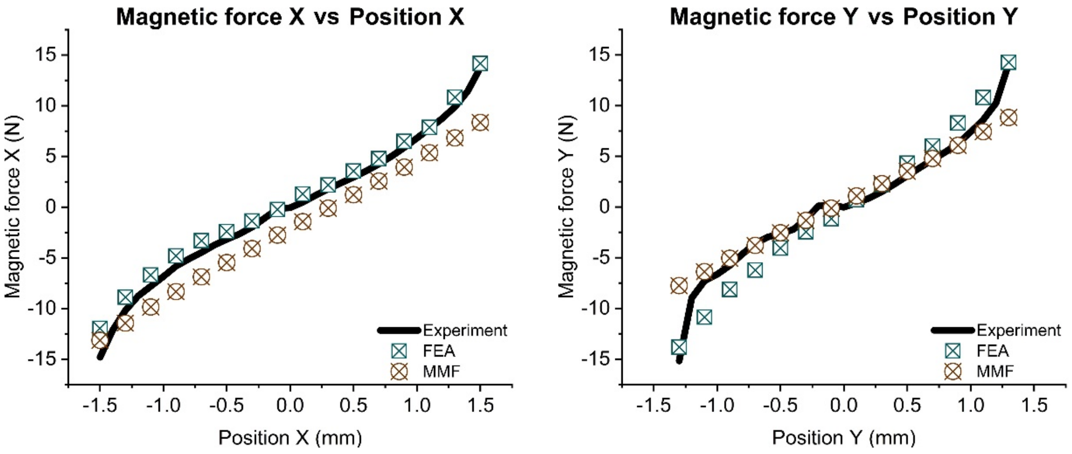

(a) Magnetic force X vs Position X

(b) Magnetic force Y vs Position Y

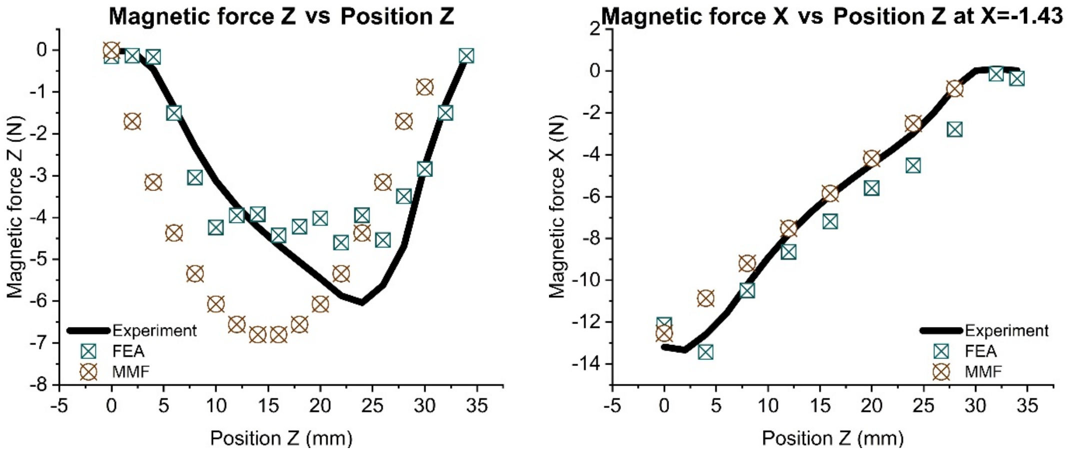

(c) Magnetic force Z vs Position Z

(d) Magnetic force X vs Position Z at X = -1.43 mm

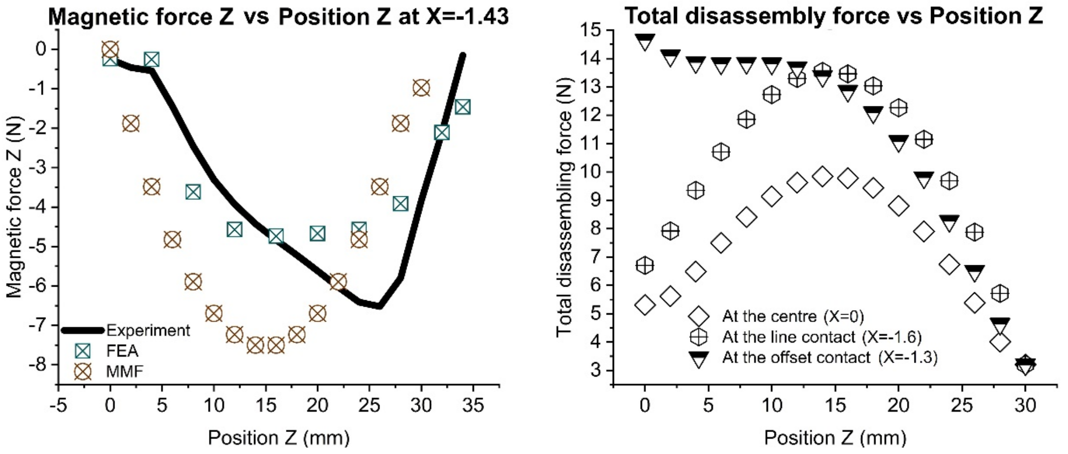

(e) Magnetic force Z vs Position Z at x = -1.43 mm

(f) Total disassembly force

Figure 3-8 Validation of the experiment, the MMF and the FE methods and the results of the total disassembly force.

Appendix B presents the FE simulation results for the cases of the rotor moving along the X, Y and Z directions relative to the stator. To find the optimal disassembly path, the magnetic forces on the rotor are considered. The resultant magnetic forces along X or Y are significantly increased when the magnets are close to the left or right side of the hub, as the magnetic fields are concentrated on one side (Figure 3-9 (a), (d) and (c) (f)). However, the forces are smaller at the centre of the steel hub because the magnetic forces cancel out (Figure 3-9 (b) and (e)). Moreover, radial movements in the X and Y directions cause significant changes in the magnetic force when the offset position (X=-1.43) and central position (Figure 3-8 (a) and (b)) are compared. However, they have limited effects on the axial magnetic force Z (Figure 3-8 (c) and (e)).

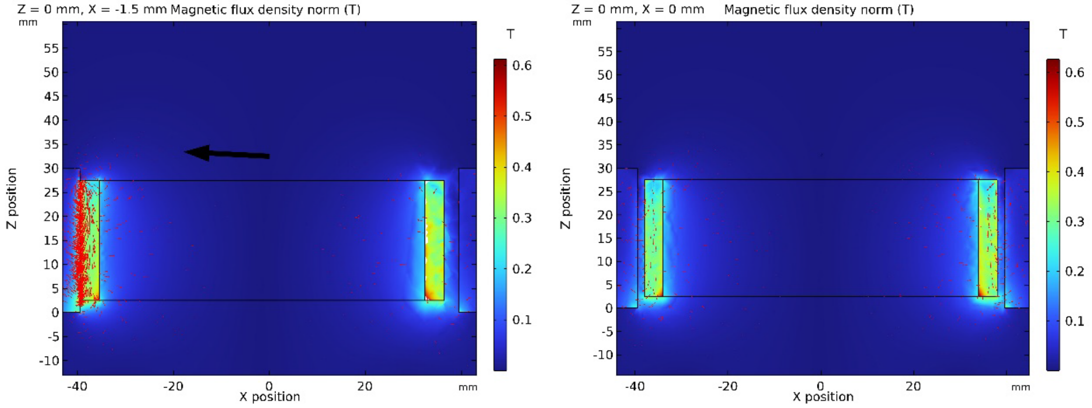

(a) at Z = 0 mm and X = - 1.5 mm (b) at Z = 0 mm and X = 0 mm

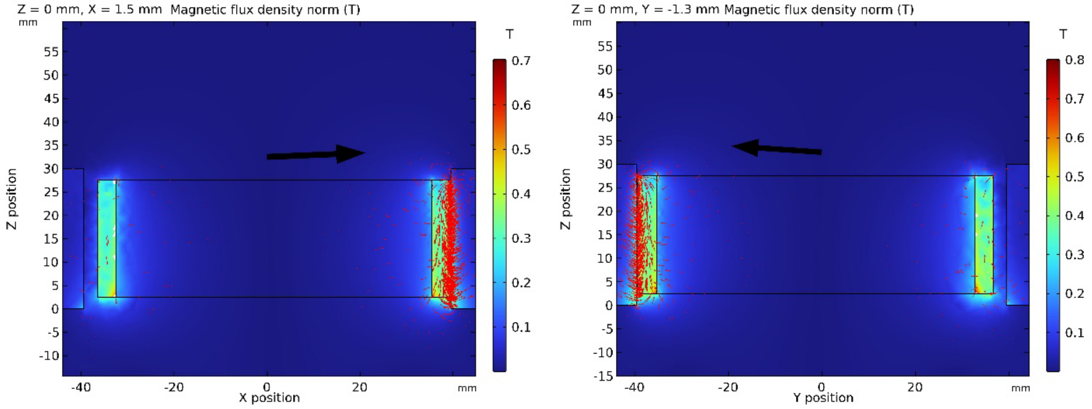

(c) at Z = 0 mm and X = 1.5 mm (d) at Z = 0 mm and Y = - 1.3 mm

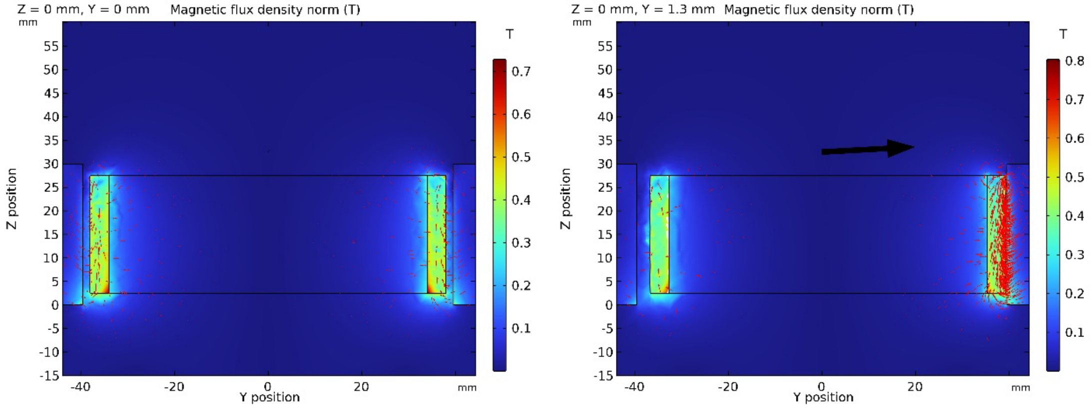

(e) at Z = 0 mm and Y = 0 mm (f) at Z = 0 mm and Y = 1.3 mm

Figure 3-9 Rotor motion in the X and Y directions. The colour table represents the magnetic flux density norm. The red arrows represent the proportional magnetic flux density in the X, Y and Z directions, and the block arrow represents the proportional resultant magnetic force of the magnet.

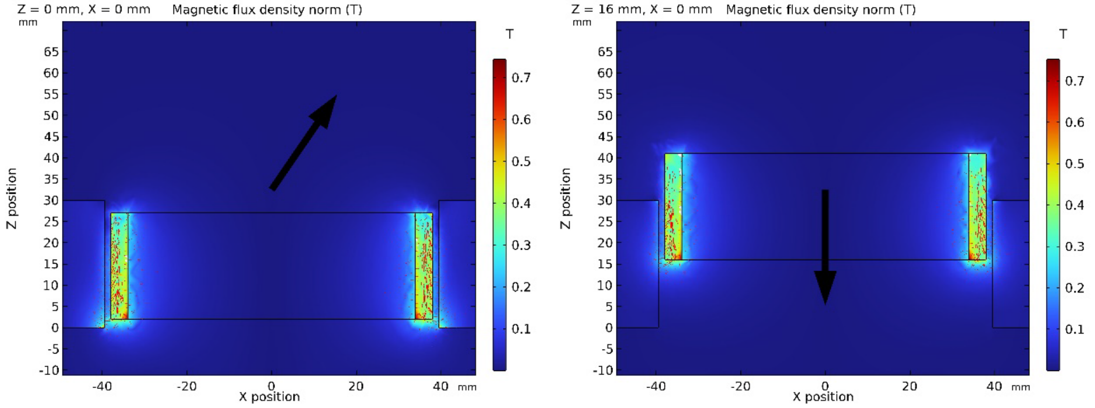

(a) at Z = 0 mm and X = 0 mm (b) at Z = 16 mm and X = 0 mm

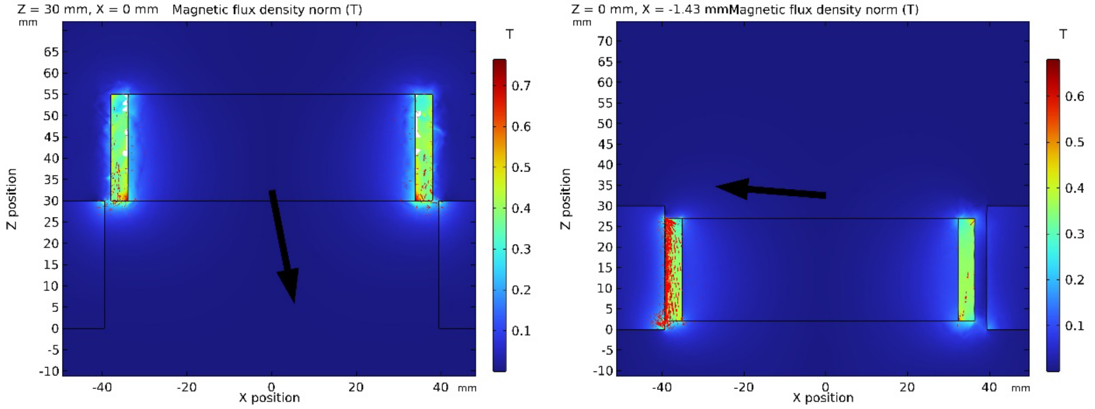

(c) at Z = 30 mm and X = 0 mm (d) at Z = 0 mm and X= -1.43 mm

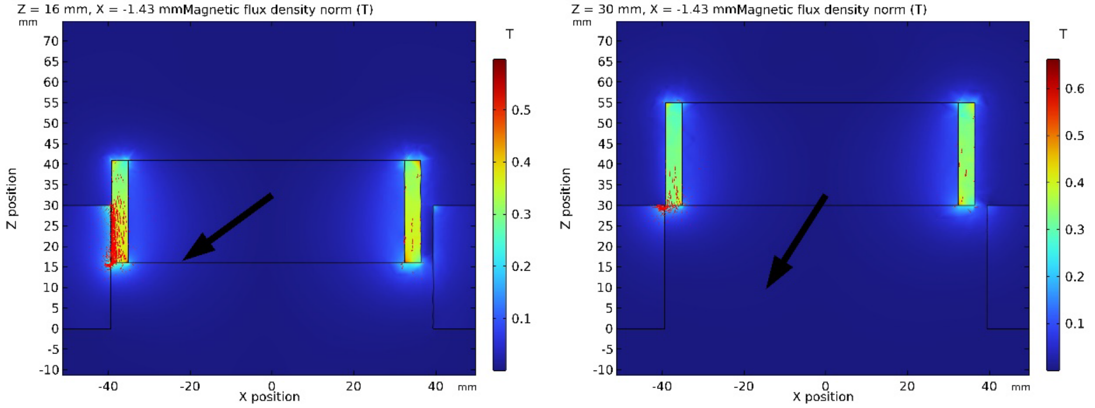

(e) at Z = 16 mm and X = -1.43 mm (f) at Z = 30 mm and X = -1.43 mm

Figure 3-10 Rotor motion in the Z direction: (a), (b) and (c) with the rotor and stator remaining concentric and (d), (e) and (f) with the rotor axis offset by -1.43 mm along the X direction relative to the stator axis. The colour table represents the magnetic flux density norm. The red arrows represent the proportional magnetic flux density in the X, Y and Z directions, and the block arrow represents the proportional resultant magnetic force of the magnet.

The total disassembly force is minimal at the centre of the steel hub (9.84 N at X = 0 mm) compared with that in the contact condition (13.14 N at X = -1.6 mm) and the offset condition (14.33 N at X = -1.3 mm) (Figure 3-8 (f)). Thus, compared with the disassembly force under the contact condition and the offset condition, the maximum disassembly force in the balanced non-contact case is 38% and 49% lower, respectively. The best way for a robot to remove the rotor would be to lift it out of the steel hub while keeping it concentric with the hub (i.e., X = Y = 0 mm). In addition to requiring the minimum disassembly force, this also prevents surface damage to both components.

3.5 Summary

A model to calculate the magnetic forces has been generated via the MMF method. The average error rates of the FE method and MMF method are 16.7% and 26.3 %, respectively. Compared with the FE method, the MMF method works as a fast model for computing magnetic forces, but it is difficult for the MMF method to accurately determine magnetic forces along the axial direction of the rotor because of corner effects. The FE method enables corner effects to be accounted for but requires high-performance computers and a long computational time. The potential use of this MMF model is merged into robotic control programs to achieve a fully automatic disassembling process, in which magnetic forces are determined during motor disassembly and input to the

MMF model. Then, optimised disassembling positions are output back to be executed by the robot.

The optimal disassembly strategy is to keep the rotor concentric with the stator to eliminate radial magnetic forces on the rotor while withdrawing it axially. In this central position, the magnetic forces along the radial direction are balanced, so the rotor does not attach to the stator, and the total disassembly force consists only of the weight of the rotor and the magnetic force along the axial direction. Thus, compared with the disassembly forces under the contact and offset conditions, the maximum disassembly force is lower. Therefore, as the proposed robotic method for disassembling PM motors, this strategy helps reduce the total disassembly force and avoids damage to the rotor and stator surfaces.

However, in practice, challenges remain due to unstable magnetic fields and the imperfect symmetry of the rotor and stator structures. Thus, the rotor position where lateral magnetic forces are minimised might not be at the exact centre of the stator. To take these practical imperfections into account, future work might focus on improving the accuracy of the MMF method by experimentally determining the magnetic permeability of the steel hub.

Chapter 4 Unbalanced magnetic pulling problems in disassembly

4.1 Problem description

In the previous chapter, the author proposed a model to calculate magnetic forces via the MMF method and the FE method. Compared with the FE method, the MMF method demonstrated reasonably high accuracy in estimating magnetic forces while requiring significantly shorter computation times, and it does not necessitate the use of high-performance computing resources. However, a critical problem, which significantly affects the magnetic force, is defined as the unbalanced magnetic pulling force (UMPF) problem. This problem is caused by differences in magnetic poles and complicates the identification of positions where magnetic forces are minimised in the horizontal directions. This section explores the UMPF problem in detail and proposes enhancements to the MMF model to more accurately predict the optimal force positions for robotic disassembly applications.

The UMPF problem in the motor disassembly scheme is defined in this section. UMPF problems are caused by uneven distributions of magnetic fields on the rotor. Five different cases are defined on an EOL surface-mounted permeant magnet motor in the disassembly stage. The full pole is a normal condition of a motor, in which the magnetic field of each magnet is slightly different because of quality issues in manufacturing (Figure 4-1 (a)). One-pole failure might occur due to magnet breakage or damage from high temperatures (Figure 4-1 (b)). This also happens when 2 poles fail in the symmetrical structure (Figure 4-1 (c)) and in the asymmetrical structure (Figure 4-1 (d)) of the rotor. Multipole failure might occur during firing or burning on one side of the motor and might be caused by short circuits on coils or cables (Figure 4-1 (e)).

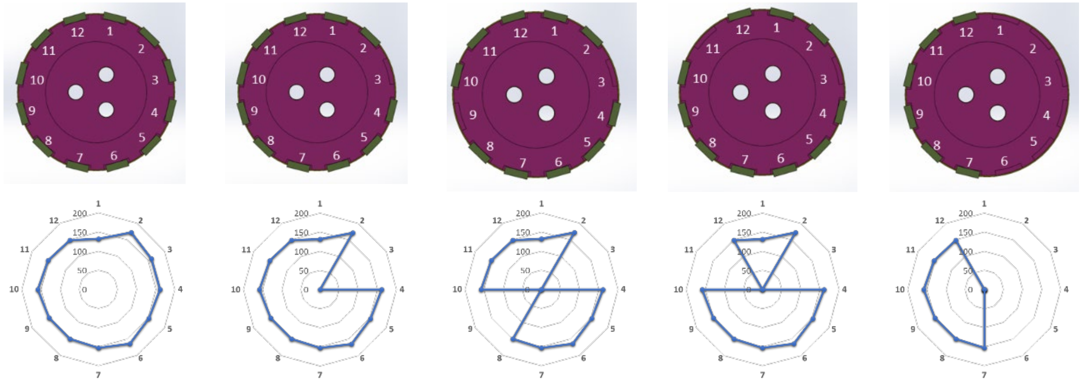

(a) (b) (c) (d) (e)

Figure 4-1 Description of 5 cases of the UMPF problem in motor disassembly: (a) full poles, (b) 1 pole missing, (c) 2 poles missing symmetrically, (d) 2 poles missing asymmetrically and (e) poles 1–6 missing.

Relative to the disassembly process, the airgap design, intended to manage thermal effects in a range between 0.7 and 1.5 mm, allows the rotor to move within the stator during disassembly. The robotic disassembly process demands that the rotor remains parallel to the stator under no contract conditions, which prevents surface damage to both the rotor and stator. To reduce the disassembly forces, the best disassembly position is defined such that the lateral resultant magnetic forces are minimised in the airgap. The key problem is to find the best disassembly position in the 5 cases in the airgap. In other words, this can also be explained as an optimisation problem between the disassembly position in the airgap and the disassembly force. To solve this problem, magnetic forces are calculated on the basis of the magnetic field at different positions in the airgap. On the basis of previous studies, the MMF method is a better option than the FE method for solving this problem in terms of time consumption and equipment requirements. The accuracy of the MMF method can be improved by measuring magnetic hysteresis (B–H curve) from the material; then, the improved MMF method is applied to the UMPF problem in the motor disassembly stage.

With respect to experiments and validations, Cuellar *et al.* (2012) reviewed different methods for magnetic hysteresis determination, and a common method is experimental measurement in which coils generate induction magnetic fields when currents pass through (Kis *et al.*, 2004; Lu, Zhu and Hui, 2007 and Lu *et al.*, 2021). However, employing coils might cause challenges in performing experiments within a robotic disassembly workstation. Therefore, the author considers measuring the B–H curve by using a robot and Force Torque (FT) sensor at room temperature.

4.2 Methodology

4.2.1 Fitting the B-H function applied on MMF

Eq. 4.2 is derived from Eq. 4.1, the widely used equation for calculating magnetic forces, where the magnetic forces (F_{xt}) are determined from the FT sensor and the magnetic flux density of the magnet (B_{rt}) is measured by a Gauss meter in the experiment. Eq. 4.3 is employed to calculate the magnetic flux density in the airgap (B_{gt}).

$$F_{xt}(x_t, z_t) = -\frac{B_{gt}(x_t)^2 A_b(z_t)}{2\mu_{fitting}} \tag{4.1}$$

$$\mu_{fitting} = -\frac{B_{gt}(x_t)^2 A_b(z_t)}{2F_{xt}(x_t, z_t)} \tag{4.2}$$

$$B_{gt}(x_t) = \left(\frac{B_{rt}}{x_t + \frac{T_{mt}}{\mu_{rt\_mag}}}\right)\left(\frac{T_{mt}}{\mu_{rt\_mag}}\right)\left(\frac{A_{mt}}{A_{gt}}\right) \tag{4.3}$$

where A_b and A_{mt} are the cross-sectional areas of the steel hub and test magnet, respectively (Eqs. 4.4 and 4.5).

$$A_b(z_t) = (L_r - |z_t|) * W_b \tag{4.4}$$

$$A_{mt}(z_t) = (L_{mt} - |z_t|) * W_{mt} \tag{4.5}$$

4.2.2 Magnetic unbalancing pulling problem in motor disassembly

The initial MMF model for motor disassembly was introduced in the previous chapter. A similar model is developed to calculate the position on the X and Y planes where the resultant magnetic forces are minimised (Figure 4-2). For simplicity, the slot structures are neglected, and the rotor and stator are assumed to be smooth cylinders in the MMF model. Importantly, the magnetic forces along the Z direction are considered negligible because of their minimal impact on the total disassembly force when the positions are changed.

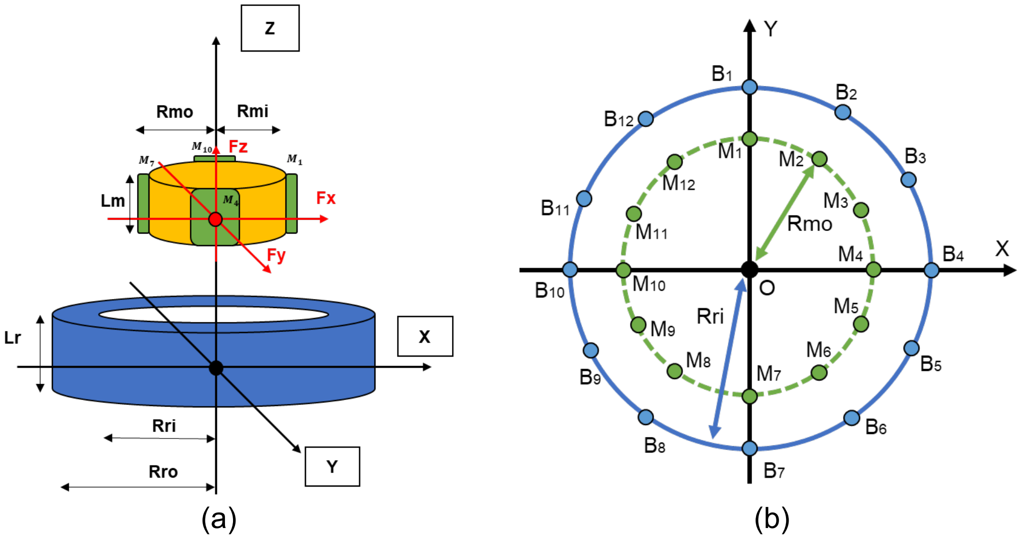

(a) (b)

Figure 4-2 MMF model for motor disassembly: (a) diagram of rotor disassembly from a hub (3D view) and (b) positions of the magnet and hub on the X and Y planes (top view).

The distance is calculated by the coordinates of the magnet and the steel hub (Eq. 4.6) and the resulting magnetic force in the X- and Y-directions (Eqs. 4.9 and 4.10). The geometries of the rotor and steel hubs are described in Eq. 3.16, Eq. 3.17, Eq. 3.24 and Eq. 3.25.

$$d_g(i,x,y) = \sqrt{(x'_B(i) - x'_M(i))^2 + (y'_B(i) - y'_M(i))^2} \tag{4.6}$$

$$B_g(i,x,y) = \left(\frac{B_r(i)}{d_g(i,x,y) + \frac{T_m(i)}{\mu_{r_{mag}}}}\right)\left(\frac{T_m(i)}{\mu_{r_{mag}}}\right)\left(\frac{A_m(i)}{A_g(i)}\right) \tag{4.7}$$

$$F_i(i,x,y) = \frac{B_g(i,x,y,z)^2 A_b(i)}{2\mu_{fitting}} \tag{4.8}$$

$$F_x = \sum F_i \sin\theta_i \tag{4.9}$$

$$F_y = \sum F_i \cos\theta_i \tag{4.10}$$

4.3 Experiments

Experiment 1 aims to determine magnetic forces when the magnet approaches the steel hub (Figure 4-3 (a)). Then, the magnetic hysteresis is calculated on the basis of the determined magnetic forces and positions. The structure of experiment 1 is that a single piece of permanent magnet is attached to the FT sensor (model: ATI Omega 85), and the FT sensor is installed onto the end effector of the Staubli TX90L collaborative robot arm with a touch-sensitive cover. The magnetic flux density of the magnet is measured by a Gauss meter (Model: San Liang TS200). The steel hub is fixed on a table. The robot moves the magnet approaching the hub in the X direction. The FT sensor determines 1000 data points at each position, and the experiment is repeated 5 times.

Experiment 2 aims to validate the magnetic forces calculated from the MMF model at different positions within the hub (Figure 4-3 (b)). The structure of the hub is the same as that in experiment 1. In contrast, a rotor, which has 12 magnets, is fixed onto the FT sensor in experiment 2. The magnet can be disassembled from the rotor to validate the 5 different cases. The rotor is moved by the robot within the stator to validate the result of the MMF model. Ten random measurements are taken at different positions in each case, and each position has 1000 force data recordings. The key parameters of both experiments are shown in Table 4-1.

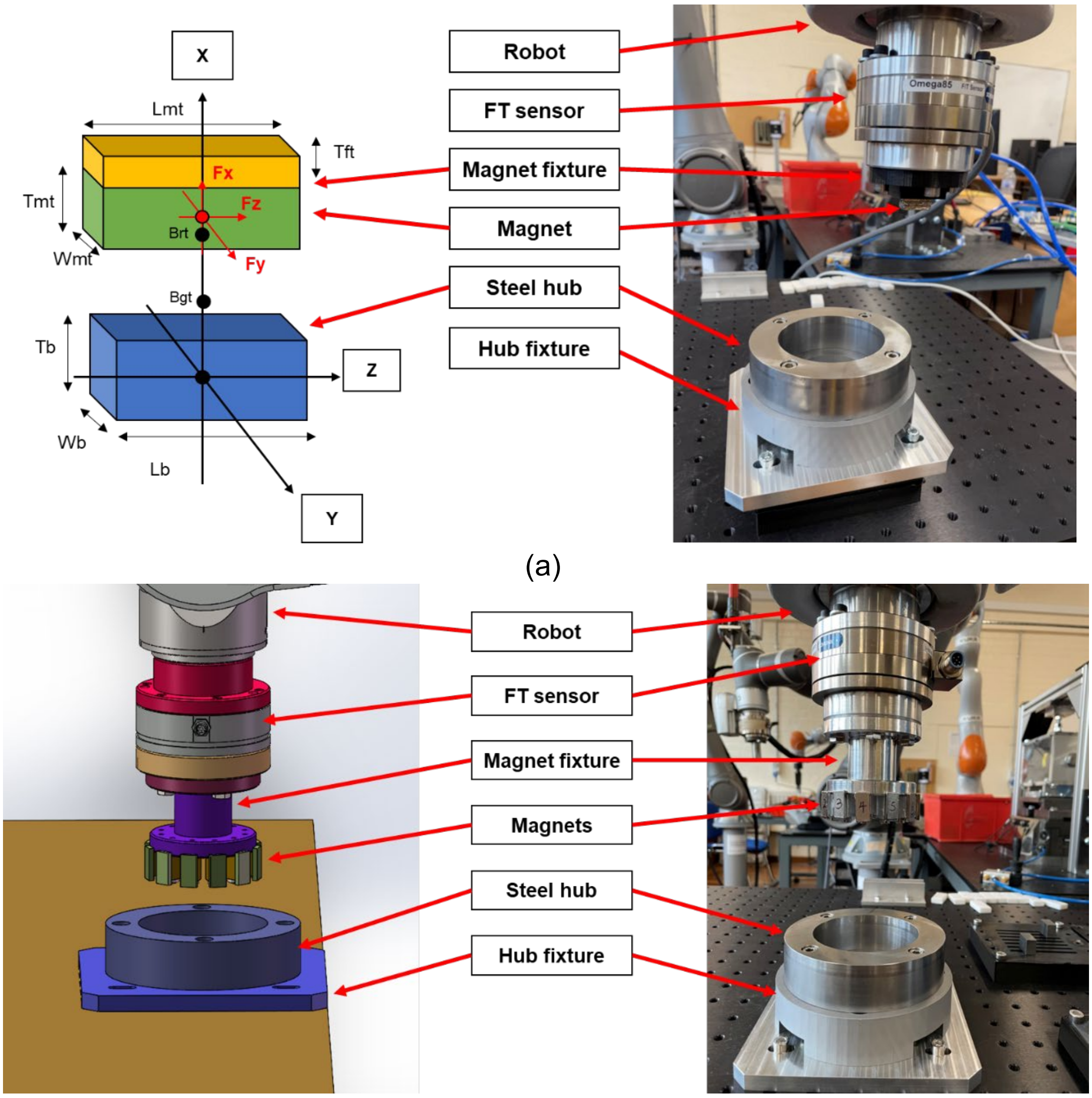

(a)

(b)

Figure 4-3 Experiments: (a) experiment of measuring the force and distance to calculate the B–H curve and (b) experiment of measuring the magnetic force at distances to calculate the B–H curve.

Table 4-1 Key parameters of 2 experiments in the UMPF problem.

No	Parameters	Abb	Values	Unit
1	The cross-sectional area of the steel hub	A_b	Calculated	mm^2
2	The cross-sectional area of the airgap	A_g	$=A_m$	mm^2
3	The cross-sectional area of the test airgap	A_{gt}	Calculated	mm^2
4	The cross-sectional area of the magnet	A_m	Calculated	mm^2
5	The cross-sectional area of the test magnet	A_{mt}	Calculated	mm^2
6	The magnetic flux density just above the hub	B_g	Calculated	T
7	The magnetic flux density just above the hub in test	B_{gt}	Unknow	T
8	The flux density of magnet 1 on the rotor	B_r1	0.1325	T

9	The flux density of magnet 2 on the rotor	B_r2	0.1725	T
10	The flux density of magnet 3 on the rotor	B_r3	0.1609	T
11	The flux density of magnet 4 on the rotor	B_r4	0.1615	T
12	The flux density of magnet 5 on the rotor	B_r5	0.1524	T
13	The flux density of magnet 6 on the rotor	B_r6	0.1646	T
14	The flux density of magnet 7 on the rotor	B_r7	0.1533	T
15	The flux density of magnet 8 on the rotor	B_r8	0.1497	T
16	The flux density of magnet 9 on the rotor	B_r9	0.1491	T
17	The flux density of magnet 10 on the rotor	B_r10	0.1588	T
18	The flux density of magnet 11 on the rotor	B_r11	0.1522	T
21	The flux density of magnet 12 on the rotor	B_r12	0.1496	T
22	The flux density of magnet for measurement of magnetic permeability	B_{rt}	0.1563	T
23	Total magnetic forces	F	Unknown	N
24	Resultant magnetic forces along X direction	F_x	Unknown	N
25	The test magnetic forces along x	F_{xt}	Determined	N
26	Resultant magnetic forces along Y direction	F_y	Unknown	N
27	The distance between the magnet and the hub	g	Calculated	mm
28	The length of the steel hub	L_b	30	mm
29	The length of the test magnet	L_{mt}	25	mm
30	Position of the rotor after movement	P'_M	Calculated	-
31	The inner radius of the steel hub	R_{bi}	39.5	mm
32	The outer radius of the steel hub	R_{bo}	59.5	mm
33	The inner radius of the magnet	R_{mi}	32.5	mm
34	The outer radius of the magnet	R_{mo}	35.5	mm
35	The thickness of the steel hub	T_b	15	mm
36	The thickness of the test magnet	T_{mt}	3	mm
37	The width of the hub	W_b	10	mm
38	The width of the test magnet	W_{mt}	10	mm
39	Movement on X direction on global coordinate system	x	Determined	mm
40	X original position (at the centre of the hub)	x_0	0	mm
41	X position of magnet after movement in global coordinate system	x'_M	Calculated	mm
42	The test magnet movement along x	x_t	Determined	mm
43	Movement on Y direction on global coordinate system	y	Determined	mm
44	Y original position (at the centre of the hub)	y_0	0	mm
45	Y position of magnet after movement in global coordinate system	y'_M	Calculated	mm
46	The test magnet movement along z	z_t	Determined	mm
47	Magnetic permeability by a fitting function	$\mu_{fitting}$	Unknown	H/m
48	Magnetic permeability of the test magnet	μ_{rt_mag}	1.05	H/m
49	The angle between magnets	θ_i	30	Deg
50	The angle of cylindrical magnet	θ_m	8.46	Deg

4.4 Results

4.4.1 B-H curve fitting function

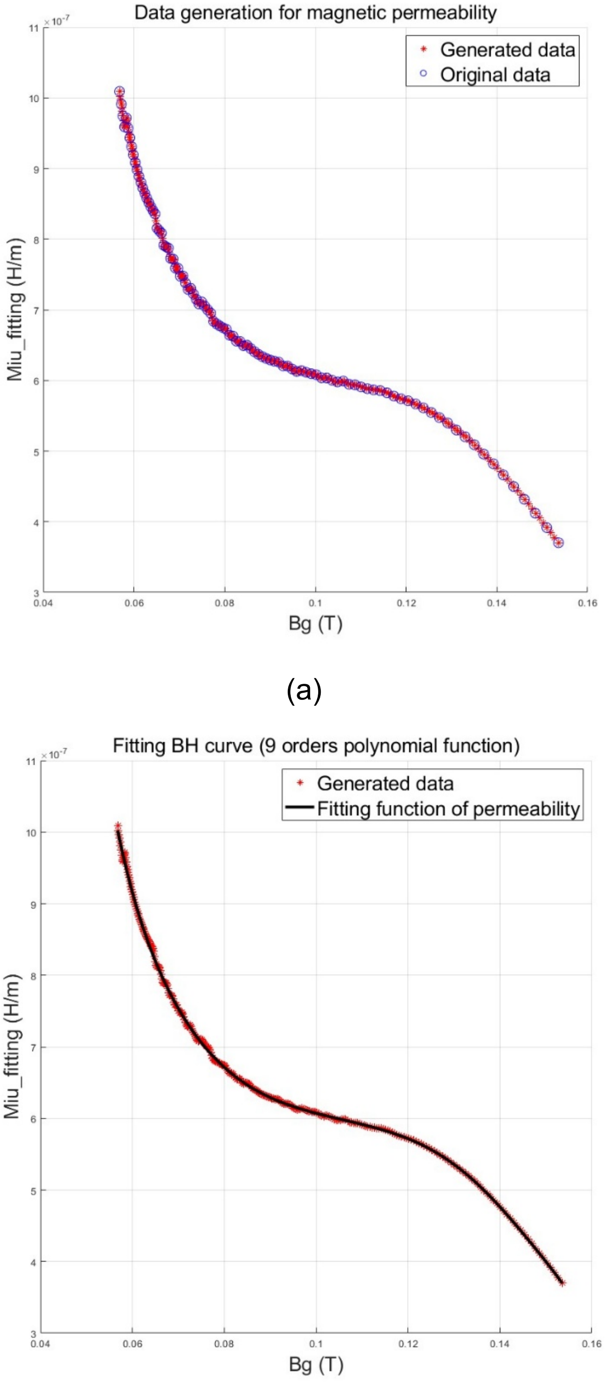

(a)

(b)

Figure 4-4 Plots of the fitting function: (a) data generation for the B-H curve and (b) fitting function for the B-H curve.

The blue circles represent the original points determined from the experiment (Figure 4-4 (a)). The red stars represent the generated data, and appropriately generated data help to fit the B–H curve easily (Figure 4-4 (b)). The determinations are not distributed even when the magnet approaches the steel hub, and the magnetic forces are significantly different at small distances from the steel hub; however, the determinations are not sensitive at large distances. Too much or too little data leads to function overfitting or underfitting. Hence, generating additional data points aids in establishing a more even distribution, which facilitates the fitting of the B–H curve. Therefore, 300 data points are generated on the basis of 100 original measuring points from the experiment, and a 9-order polymodal equation, as a fitting function, is employed as a regression function to describe the behaviour of magnetic hysteresis (Eq. 4.11). The R-square (R^2) for this regression of the B–H curve was 0.999. Eq. (4.11) is used in Eq. (4.8), providing magnetic permeability to calculate magnetic forces when the values of magnetic flux density in the airgap are input ($\mathrm{B_g(i, x, y)}$).

$$\begin{aligned}\mu_{\mathrm{fitting}}(\mathrm{B_g}) = {} & -8.594\mathrm{E}4\ \mathrm{B_g}^9 + 8.246\mathrm{E}4\ \mathrm{B_g}^8 - 3.481\mathrm{E}4\ \mathrm{B_g}^7 + 8489\mathrm{B_g}^6 \\ & - 1319\mathrm{B_g}^5 + 135.5\mathrm{B_g}^4 - 9.213\mathrm{B_g}^3 + 0.4009\mathrm{B_g}^2 \\ & - 0.01017\mathrm{B_g} + 0.0001163\end{aligned} \tag{4.11}$$

4.4.2 Magnetic unbalancing pulling problem in motor disassembly

It is very difficult to determine where the resultant magnetic forces are exactly equal to 0 because of unstable magnetic forces, the resolution of the FT sensor and the resolution of the robot in the experiment. Therefore, the positions where the resultant magnetic forces are less than 1 N are considered the force optimised positions so that this area is acceptable for disassembling the motor. To reduce time consumption in the calculation, it is important to know that the MMF model calculates only positions where the resultant magnet forces are most likely minimised rather than calculating the entire area of the air gap within the steel hub.

Overall, most of the experimental results agree well with the plot from the improved MMF model. The success rates reached 90% agreement in the case of full poles (Figure 4-5 (a)) and achieved a 100% match when pole 3 was missing (Figure 4-5 (b)), poles 3 & 9 were missing (Figure 4-5 (c)), and poles 3 & 11 were missing (Figure 4-5 (d)). However, the calculation results demonstrate poorer performance in the case of 1–6 pole missing (Figure 4-5 (e)) because of differences between the MMF model and experiment. To eliminate the removal of magnetic fields in the experimental set up, magnets 1 to 6 were removed from the rotor so that the diameter of the rotor is reduced by the thickness of the magnet. Hence, the rotor enables movement extremely close to the edge of the stator. However, in the MMF model, the magnetic field can be eliminated by setting it to 0 without changing the geometry of the rotor. Therefore, the diameter of the rotor is different between the MMF model and the experiment, leading to calculated results being smaller than the experimental results. Fortunately, the general trend of the plot matches the experimental results; therefore, all the calculated results are acceptable for analysis.

The key findings highlight that reducing the distance between the magnet and the steel hub increases magnetic forces, and when poles are missing, the magnetic forces are decreased, allowing the disassembly movement of the rotor to proceed unaffected by these forces. However, the magnetic forces are still increased significantly because of the magnets in where neighbouring the missing pole when the rotor moves too close to the steel hub. The findings are applied to 5 different cases of the UMPF problem in motor disassembly. First, in the full pole case, the resulting magnetic forces are not unbalanced because the magnetic fields are not distributed evenly across the 12 magnetic poles on the rotor. However, the force-optimised points are still around the centre of the stator. Relative to the motor disassembly process, these slight differences in magnetic fields have limited impacts on the disassembly position, which still remains around the centre of the stator in the case of full poles. Moreover, in the case where pole 3 is missing, the areas are expanded in the direction of pole 3. The same happens in the case of poles 3&9 missing and the case of poles 3&11 missing; the asymmetrical pole missing might lead to a larger disassembly area. Therefore, the force optimised positions increase around the centre of the stator when magnetic poles are missing, considering the motor disassembly process. Finally, the force optimised positions are very offset to the side on which the magnets are removed when poles 1–6 were missing.

Thus, the side of the rotor where the magnets are missing is moved closer to the edge of the stator.

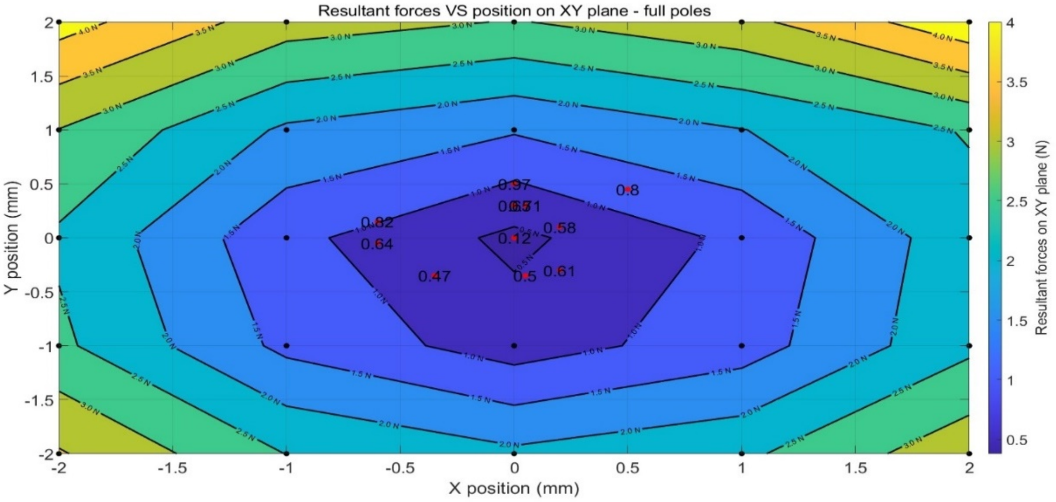

(a) Force prediction and test results in the full pole case

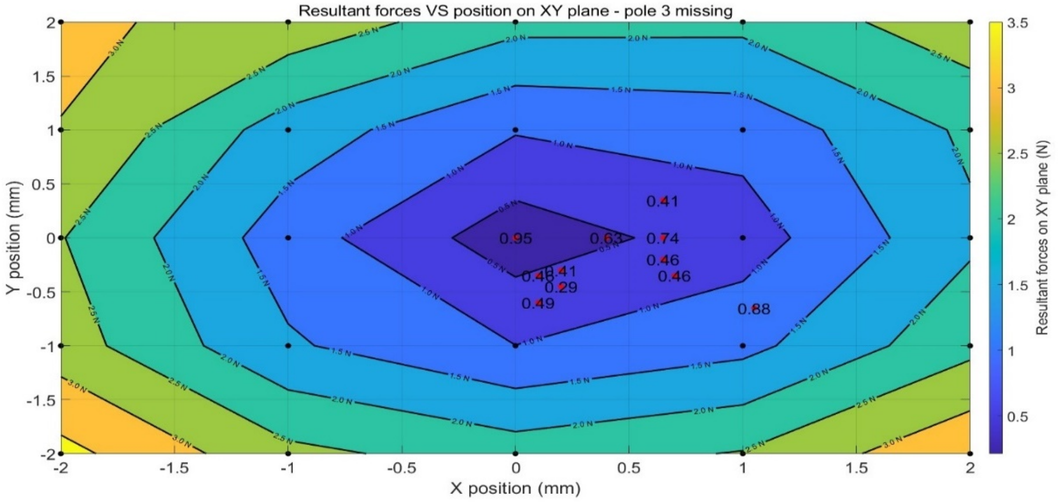

(b) Force prediction and test results in the pole 3 missing case

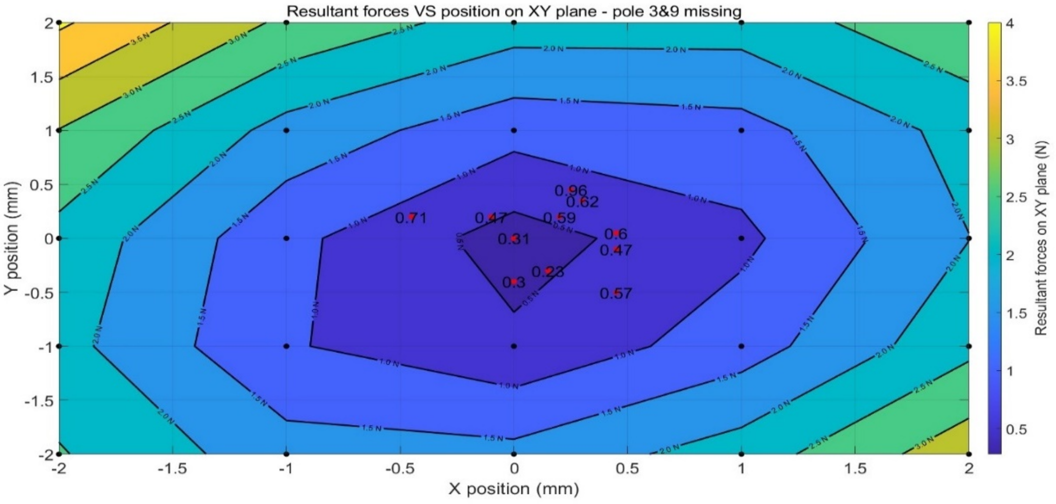

(c) Force prediction and test results in the poles 3&9 missing case

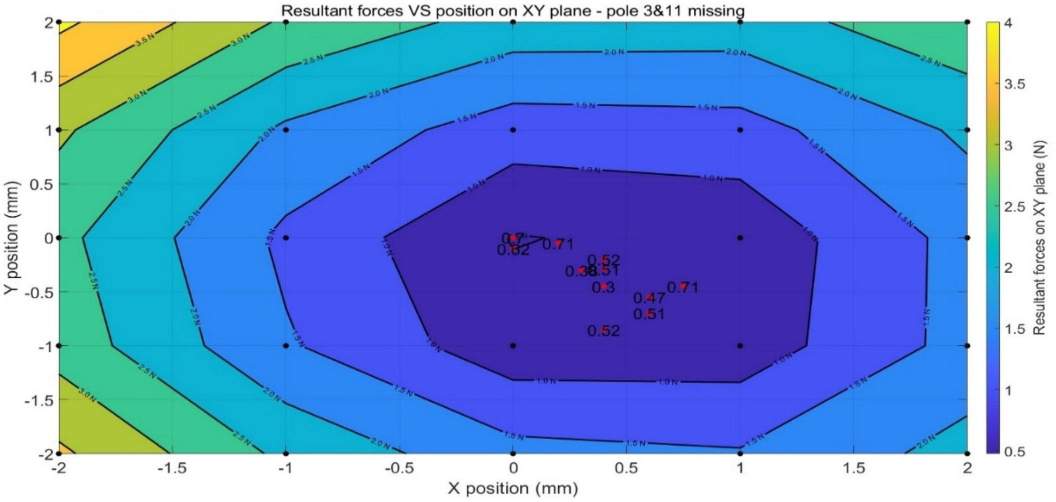

(d) Force prediction and test results in the poles 3&11 missing case

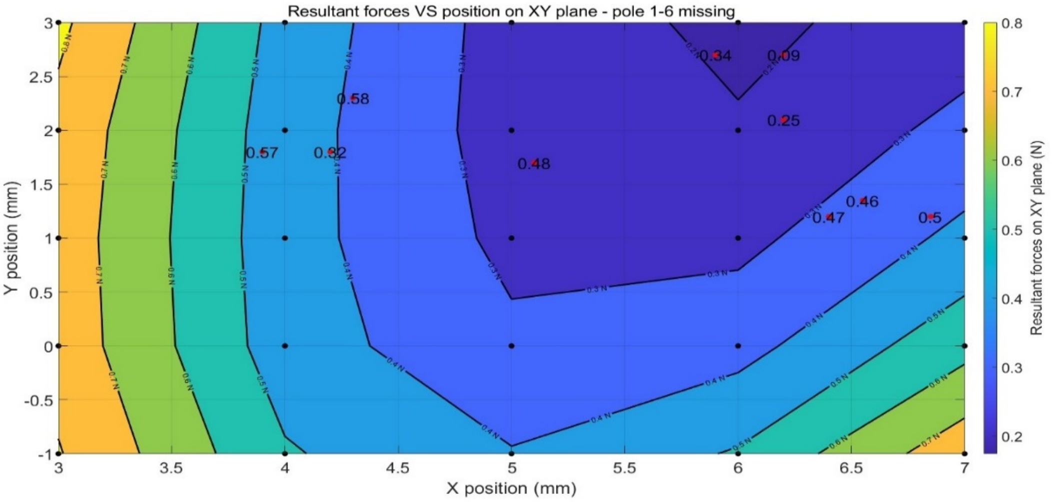

(e) Force prediction and test results in poles 1–6 missing case

Figure 4-5 Plots of the MMF and experimental results. The black points represent the calculated resultant magnetic forces on the X- and Y-planes via the improved MMF method. The red points are the resultant magnetic forces determined from the experiment.

4.5 Summary

This chapter defines 5 different cases of the UMPF problem in motor disassembly. The MMF model is improved by the B–H curve fitting function, which is determined by the FT sensor on the robot. The improved MMF, as a minimum time consumption and reasonable accuracy method, calculates magnetic forces on the basis of the disassembly positions in the airgap. Validating the experiment, 4 cases, including cases of full poles, pole 3 missing, poles 3&9 missing, and poles 3&11 missing, achieved at least a 90% success rate. However, the MMF model has worse performance when 1–6 poles are missing because of the diameter difference between the MMF model and the experiment. However, the trends are in good agreement. Therefore, compared with the FE method, this improved MMF method can be used for large calculation points, considering time consumption and equipment requirements.

The key findings are highlighted as follows: 1. Slightly different magnetic fields have limited impacts on the force optimum positions, so the disassembly positions are still around the centre of the stator. 2. Similarly, when a few magnets are removed, the total area of the force optimum positions increases around the centre of the station. 3. The worst performance in the MMF model is that most magnets are removed on one side because of the difference in the diameter of the rotor between the MMF model and the experiment; thus, the force-optimised position is moved to the edge where magnets are missing. In this case, the robot needs to be adjusted to the rotor to offset the position to reduce the total dissembling force. The improved MMF model can be integrated with robot control software to achieve fully automatic disassembly.

Chapter 5 Press-fit component disassembly and coil disassembly

5.1 Problem description

Following the solutions provided in chapters 3 and 4, the problem of the Unplugging task (T.3) has been addressed. The problems of the Unscrewing task (T.5) and Pick and place task (T.6) have been well studied according to the literature review (Chapter 2). Thus, this chapter addresses the remaining problems in electric motor disassembly, including Press-in task (T.1), Press-on task (T.2) and Coil disassembly task (T.4).

The Press-in task (T.1) and Press-on task (T.2) describe the interference fit components on the motor. In the Press-in task (T.1), is defined that the Bearing (large) (A.2) is installed and hidden in the Front cover (A.1) (Figure 5-1 (a)), and in the Press-on task (T.2), the Rotor set (B) is fixed on the Front cover (A.1) (Figure 5-1 (b)). A bearing puller is a common solution in both the Press-in task (T.1) and Press-on task (T.2) in the manual process, in which the bearing is held by a hook and pulled out by a rotating thread.

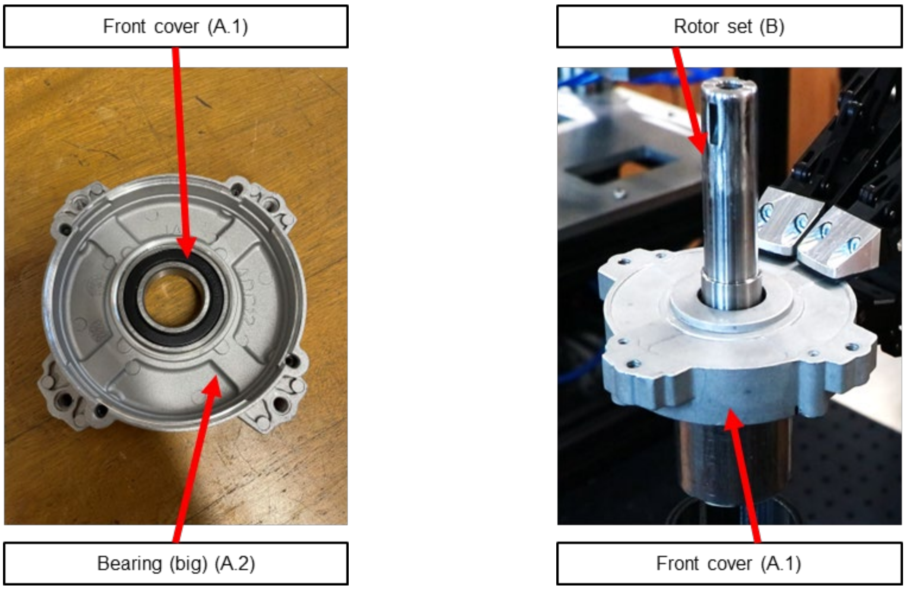

(a) Press-in task (T.1) (b) Press-on task (T.2)

Figure 5-1 Description of Press-in task (T.1) and Press-on task (T.2) on product views.

The Coil disassembly task (T.4) is the remaining unresolved issue; however, the coils, which are made of copper material, are highly valuable in the motor. There are 2 different winding methods: one way is that the copper wires are wound on each slot in the stator (Figure 5-2 (a)), and the other approach is that the copper wires are tight and inserted into the slots in the stator (Figure 5-2 (b)). Owing to difficulties in the disassembly of tangle coils, common solutions in industry are coils burning and cutting.

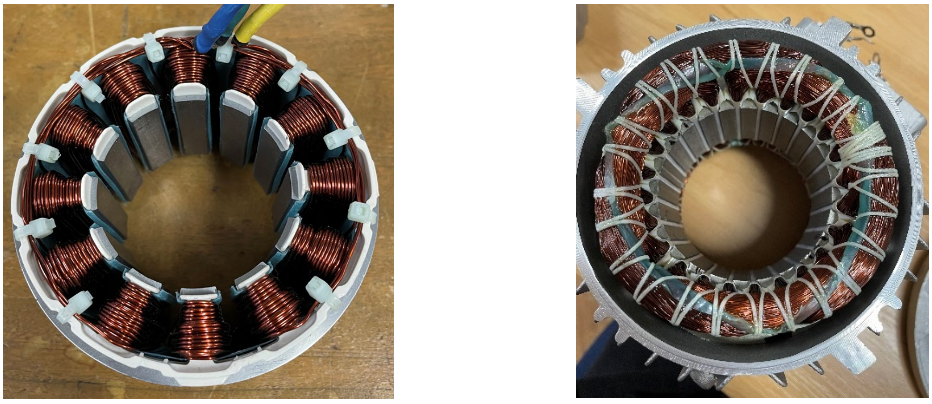

(a) Coil winding on each slot (b) Coil inserted in slots in stator

Figure 5-2 Description of coil disassembly in 2 copper winding methods.

5.2 Methodology

5.2.1 Force analysis for the Press-in task (T.1) and Press-on task (T.2)

To address the disassembly problems associated with the Press-in task (T.1) and Press-on task (T.2), it is necessary to study the disassembly forces to remove press-fit components. The author studies the example of the Press-on task (T.2) disassembly problem, in which the shaft of the Rotor set (B) has pressed into the Bearing (large) (A.2). A potential automated solution in which a puller (red part) applies forces on the shaft (blue part) to push it out from the bearing (green part) (Figure 5-3 (a)). In the left part of the model, the disassembly forces are the pushing force required from the device ($\mathrm{F_p}$) and the force loss ($\mathrm{F_{loss}}$) (Figure 5-3 (b)).

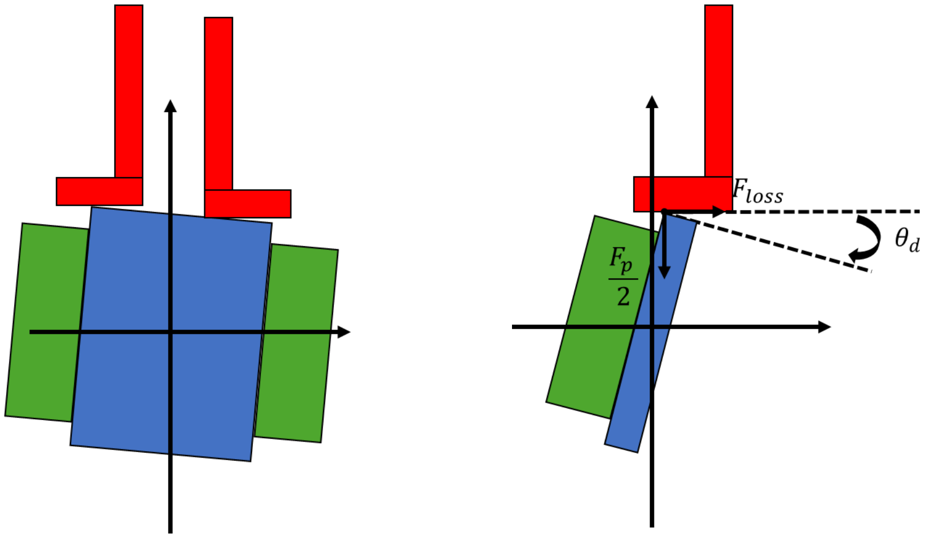

(a) Model of Press-on task (T.2)

(b) Force analysis of Press-on task (T.2)

Figure 5-3 Model of the Press-in disassembly problem.

An analytical model was developed to study interference component assembly, which strongly agreed with both the FEA results and the experimental results (Figure 5-4) (Wang *et al.*, 2017). The same model can also be applied on Press-in task (T.1) and Press-on task (T.2) disassembly problems (Eqs. 5.1-5.4). The resistant forces are negligible in the noncontracting region.

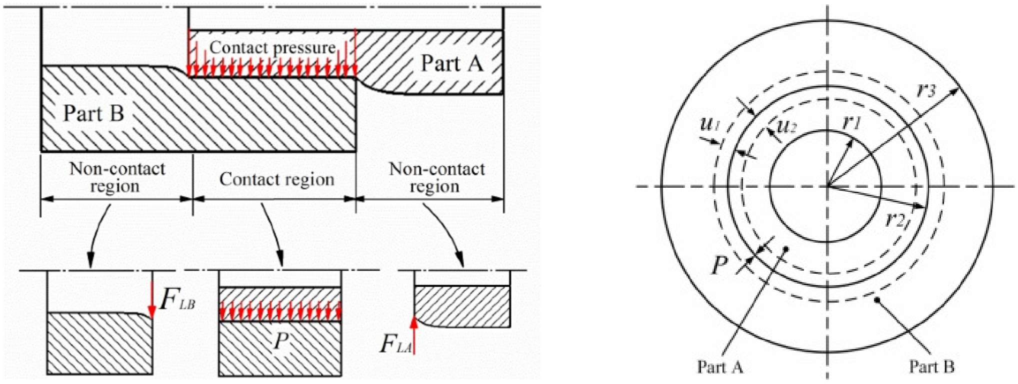

(a) Press-fit model (side view)

(b) Press-fit model (top view)

Figure 5-4 An analytic method for press-fitted component assembly (Wang et al., 2017).

$$\mathrm{P} = \frac{\mathrm{Z}}{\frac{\mathrm{r_2}}{\mathrm{E_1}}\left(\frac{\mathrm{r_1^2 + r_2^2}}{\mathrm{r_2^2 - r_1^2}} + \mathrm{v_1}\right) + \frac{\mathrm{r_2}}{\mathrm{E_2}}\left(\frac{\mathrm{r_3^2 + r_2^2}}{\mathrm{r_3^2 - r_2^2}} - \mathrm{v_2}\right)} \tag{5.1}$$

$$\mathrm{F_f} = 2\pi \mathrm{r_2 L_c P f} \tag{5.2}$$

$$\mathrm{F_{loss}} = \mathrm{F_f} * \cos\theta \tag{5.3}$$

$$\mathrm{F_p} = \mathrm{F_f} * \sin\theta \tag{5.4}$$

where the P is the pressure applied on the contact surface (Pa); Z is the half of interference value; $\mathrm{E_1}$ and $\mathrm{E_2}$ are Young's modulus of the shaft (B) and the bearing (A.2) (GPa); $\mathrm{v_1}$ and $\mathrm{v_2}$ are Poisson's ratios of the shaft (B) and the bearing (A.2); Young's modulus and Poisson's ratios are assumed as the same in the paper (Wang *et al.*, 2017); f is friction coefficient; $\mathrm{L_c}$ is the contact length (mm); $\mathrm{r_1}$, $\mathrm{r_2}$ and $\mathrm{r_3}$ are the inner radius of the Shaft (B) (mm), the outer radius of the Shaft (B) or the inner radius of the Bearing (large) (A.2) and the outer radius of the Bearing (large) (A.2) (mm); θ_d is deflection angle (degrees); $\mathrm{F_f}$ is frictional force (N); $\mathrm{F_{loss}}$ is force loss (N) and $\mathrm{F_p}$ is pulling/pushing force required from device (N).

Table 5-1 summarises the parameters used for the force calculation in the analytical model. The interference value (Z) is assumed to be H7/k6 on the hole basis or K7/h6 on the shaft basis, defined by (Kiraly Tool., 2017) for transition fit. Interference tolerances are among the most common for bearing-to-shaft or bearing-to-case assemblies. In manual assembly processes, the shaft is inserted into the bearing by using a plastic hammer or a pneumatic press. The deflection angle (θ_d) occurs when the pusher is not parallel to the bearing; thus, the maximum deflection angle is assumed to be 5 degrees.

Table 5-1 Parameters for force calculation in the Press-in task (T.1).

NO	**Parameters**	**Symbols**	**Values**	**Unit**
1	Young's modulus of the shaft (B)	E_1	157 (Wang *et al.*, 2017)	GPa
2	Young's modulus of the bearing (A.2)	E_2	186 (Wang *et al.*, 2017)	GPa
3	Poisson's ratio of the shaft (B)	v_1	0.34 (Wang *et al.*, 2017)	-
4	Poisson's ratio the bearing (A.2)	v_2	0.30 (Wang *et al.*, 2017)	-
5	Friction coefficient	f	0.09	-
6	Contact length	L	13.7	mm
7	Contact pressure	P	1.96E7	Pa
8	Inner radius of the shaft (B)	r_1	0	mm
9	Outer radius of the shaft (B) or Inner radius of the bearing (A.2)	r_2	12.5	mm
10	Outer radius of the bearing (A.2)	r_3	16.05	mm
11	Half of interference value	Z	5 (Kiraly Tool, 2017)	μm
12	Deflection angle	θ_d	**5**	Deg
13	Frictional forces	F_f	**2.24E3**	N
14	Force loss	F_{loss}	**195.60**	N
15	Pushing force required from device	F_p	**2.44E3**	N

The results indicate that a frictional force (F_f) of 2.24E3 N is required to disassemble the Rotor set (B) from the Bearing (large) (A.2). The pushing force (F_p), also referred to as the disassembly force, exceeds 2.44E3N from the device. This value will be used in the designs of devices in both the Press-in task (T.1) and Press-on task (T.2) disassembly problems. The designs for the Press-in task (T.1) and Press-on task (T.2) will be validated in the experiment.

5.2.2 Control strategy for the Coil disassembly task (T.4)

One single coil set is wound with a long copper wire. The ideal solution involves cutting one end of the copper wire and rotating it to release winding until the whole coil is removed from the stator. However, winding coils twine and overlap; thus, the main difficulties in non-destructive methods are (1) locating the end of the copper wire and (2) unwinding the twinned coil. Moreover, some coils are adhesively bonded to enhance their structure under high-temperature working conditions. To disassemble the coil in industry, one of the most common methods is to burn copper coils at high temperatures. This burning process weakens and breaks coil sets, allowing them to be easily removed from the stator. However, compared with the industrial solution, a destructive disassembly method is considered a more effective solution. Among the available options, robotic milling is a cost-effective method compared with burning the stator after coil disassembly. Force analyses of the robotic milling process and robotic trajectory are presented below.

5.2.2.1 Force control strategy

A model of coil milling is presented in this section (Figure 5-5). The coil milling process involves a spinning milling bit (orange part) moving through the coils (green part). The target is to cut off the coils without damaging the stator structure (blue part). The main key factors for calculating the cutting force ($\mathrm{F_{cut}}$) include the geometry of the milling tool, depth of cut ($\mathrm{D_{cut}}$), robot feeding speed ($\mathrm{v_{cut}}$) and spinning speed of the milling bit ($\mathrm{v_{spin}}$). To simplify the model, the depth of the cut ($\mathrm{D_{cut}}$), milling tool and spinning speed of the milling bit ($\mathrm{v_{spin}}$) are considered constant and are determined by the milting tool and milling bit, whereas the robot feeding speed ($\mathrm{v_{cut}}$) is variable during the milling process. The force control strategy aims to balance the cutting force ($\mathrm{F_{cut}}$) and robot feeding speed ($\mathrm{v_{cut}}$). If the feed speed is too high, it may damage the cutting tool, whereas if it is too low, it will slow down the coil disassembly process.

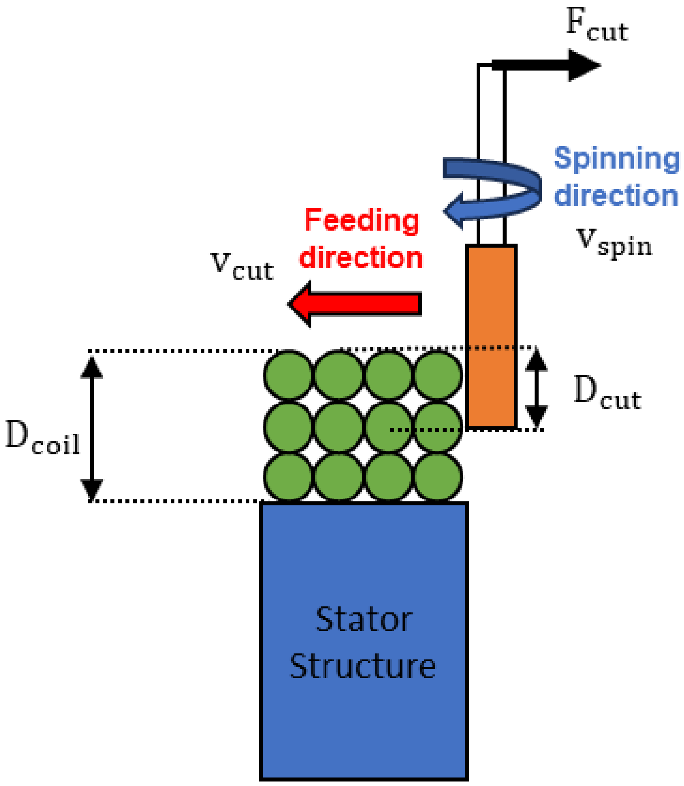

Figure 5-5 Model of coil milling in cross-sessional view.

The milling process has been extensively developed via both analytical models and numerical methods, as highlighted in the literature review. However, these models typically require precise specifications of the workpiece, and the shape of the cutting tool is specified. However, in this case, the shape of the milling bit is not specified, and the material of the copper alloy of coils is undefined. Consequently, these 2 uncertainties make accurate calculation of the cutting forces by existing milling methodologies challenging in the coil cutting process.

The author developed a method to address the problem of balancing the cutting force ($\mathrm{F_{cut}}$) and the robot feeding speed ($\mathrm{v_{cut}}$) during the milling process (Figure 5-6). The maximum cutting force is defined as the force to break the milling bit, which is determined via a finite element model. To ensure safety, this maximum cutting force is set by reducing 30% of the reference force ($\mathrm{F_0}$).The cutting force ($\mathrm{F_{cut}}$) is determined in real time via a force torque sensor during the milling process. The robot starts at an initial speed ($\mathrm{v_0}$). If the cutting force ($\mathrm{F_{cut}}$) is less than the reference force ($\mathrm{F_0}$), the robot's speed is increased by 5% of the current speed. Conversely, if the cutting force ($\mathrm{F_{cut}}$) exceeds the reference force ($\mathrm{F_0}$), the robot stops moving, resets its speed to the initial speed ($\mathrm{v_0}$) and restarts its motion. The robot moves towards a series of target positions ($\mathrm{P_n}$), and it stops when the target position ($\mathrm{P_n}$) matches the end position ($\mathrm{P_e}$). Further details regarding the milling path planned for the robot are provided in the next section. The key parameters for the milling process are shown in Table 5-2.

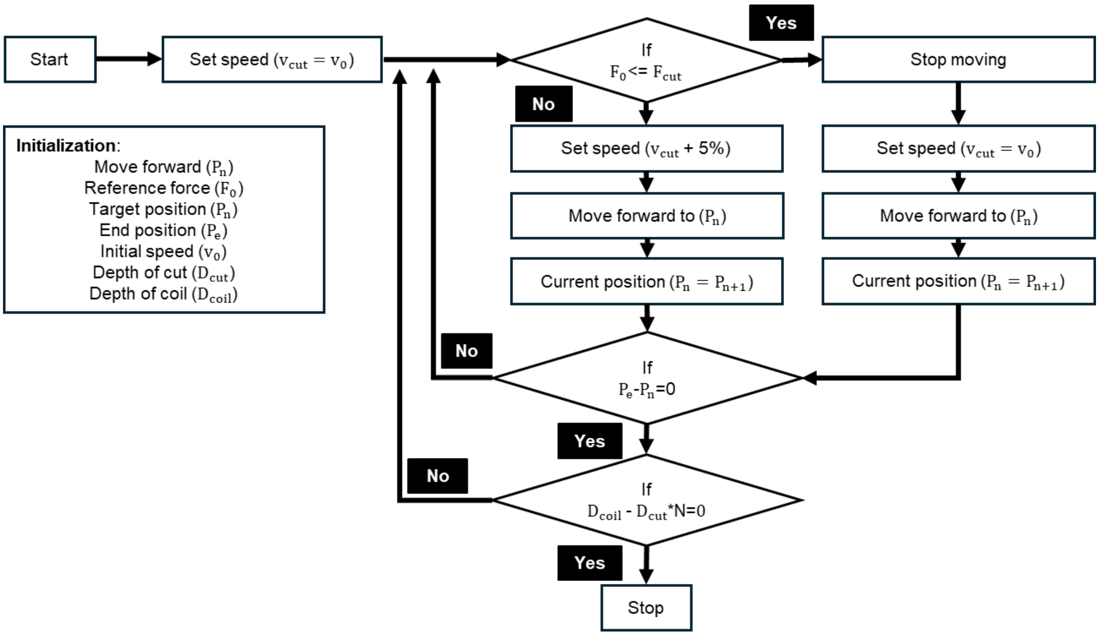

Figure 5-6 Flowchart of the force control strategy during the Coil disassembly task (T.4).

Table 5-2 Key parameters for the Coil disassembly task (T.4).

No	Parameters	Symbol	Values	Unit
1	Spinning speed	v_{spin}	35000	RPM
2	Depth of cut	D_{cut}	0.55	mm
3	Max cut of coil	D_{coil}	5.5	mm
4	Initial speed	v_0	5	%
5	Feeding speed	v_{cut}	Variable	%
6	Cutting force	F_{cut}	Reading by FT sensor during milling process	N

5.2.2.2 Milling path

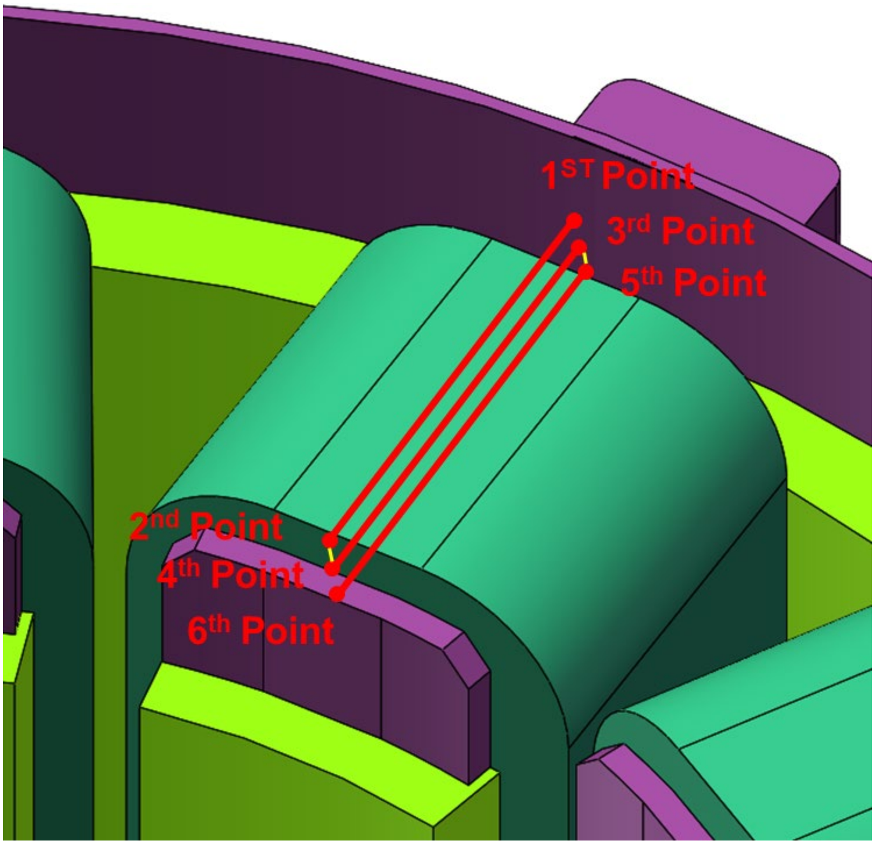

Figure 5-7 Robotic milling path on a single coil.

The milling path on a single coil is programmed by point-to-point (PTP) movement in the robotic system (Figure 5-7). The robot starts at the 1st point, moves linearly to the 2nd point linearly (red line), and then moves downwards to the 4th point before moving back to the 3rd point. This zigzag milling path is repeated until all the designed points are processed. The robotic trajectories of the Coils (C.1–C.12) on the Stator set (C.13) are explained in Appendix G.

5.2.3 Experiment set up for Press-in task (T.1) and Press-on task (T.2)

Based on the proposed model, a device is designed for both Press-in task (T.1) and Press-on task (T.2). Functions of the device are summarised as:

(1) Hook mechanism: Two hooks are designed to either hold and pull out the bearing or push the bearing out. Both hooks can move toward the centre into a closed position or move outwards into an opened position. These movements are powered by 2 pneumatic cylinders, each delivering a maximum force of 3057.4 N at 10-bar air pressure (YHDFA, n.d.).

(2) Bearing pusher: the bearing pusher controls the vertical movements of the hooks. It is driven by a single pneumatic cylinder, which provides a maximum force of 4929.4 N at 10-bar air pressure (YHDFA, n.d.).

(3) The plate is designed to hold one component and remove the other components. In the press-in task (T.1), the Front cover (A.1) is held by the plate, and the Rotor set (B.1) is pulled out (Figure 5-8 (a)). In the Press-on task (T.2), the Front cover (A.1) is held by the plate, and the Bearing (large) (A.2) is pushed out (Figure 5-8 (b)).

(4) All pneumatic cylinders are operated via solenoid valves controlled by a robotic controller.

Further details regarding the device's design are provided in Appendix C.

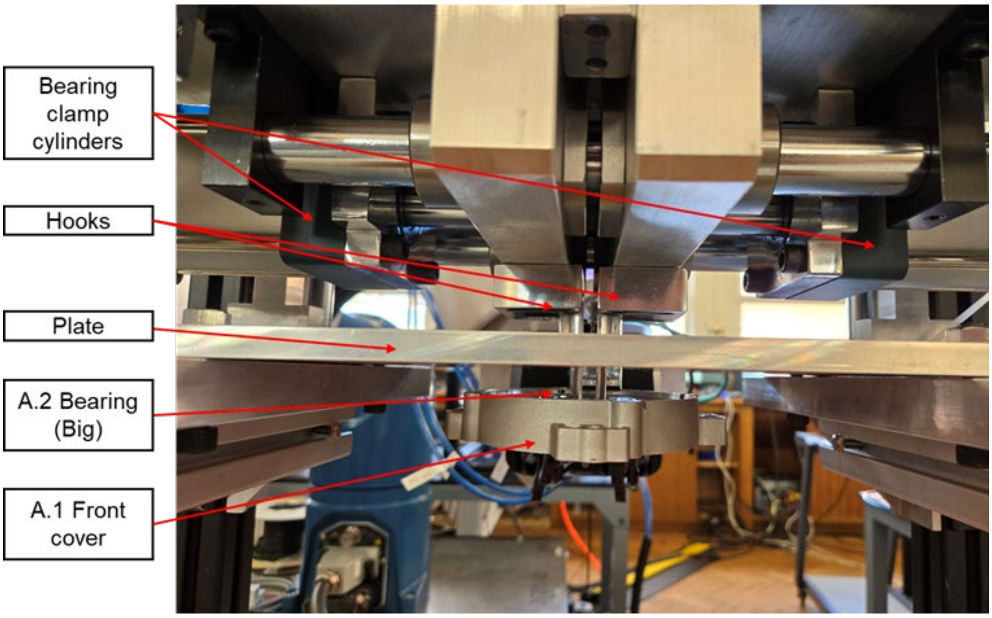

(a) Experiment set up for Press-in task (T.1)

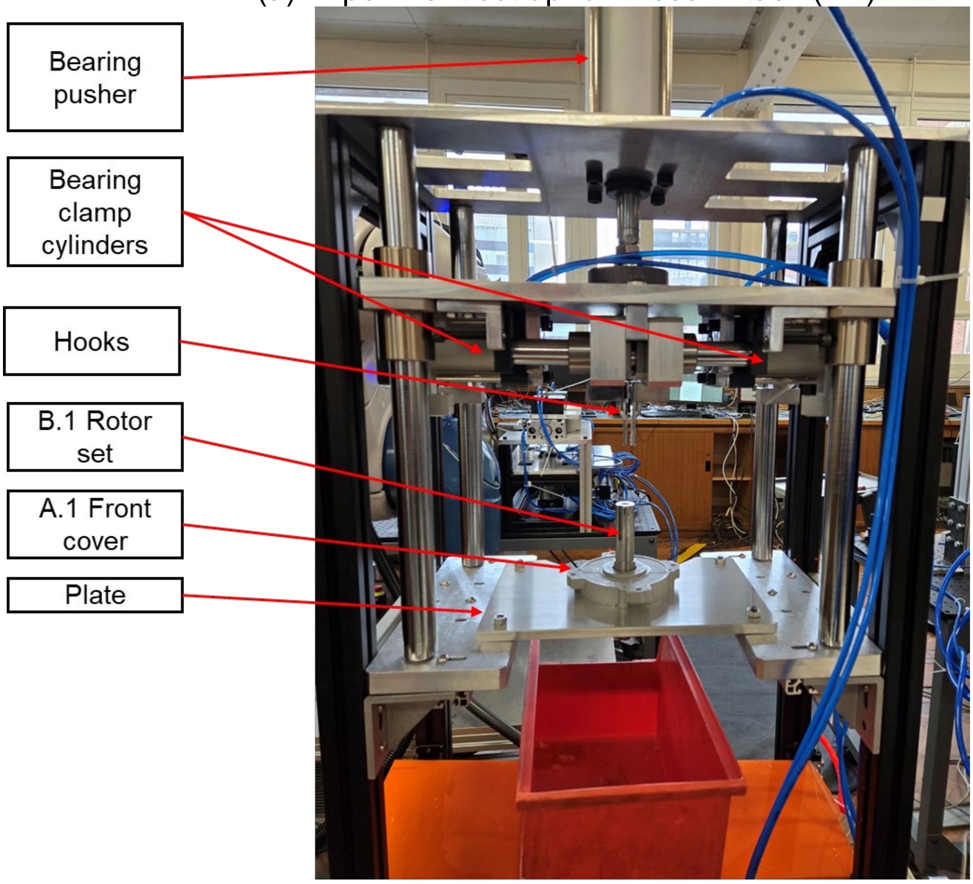

(b) Experimental set-up for Press-on task (T.2)

Figure 5-8 Experimental set-up for the Press-in task (T.1) and Press-on task (T.2).

5.2.4 Experiment set up for Coil disassembly tasks (T.4)

Two tests are designed to validate coil disassembly in this section, as described in this section:

- **Test 1**: This test focuses on milling a single wire at 50% and 100% of the robot speed (Figure 5-9 (a)). The goal is to evaluate the milling tool, robotic speed and FT sensor response during the milling process.
- **Test 2**: This test investigates the performance of coil milling on hand-made coils by using the force control strategy or the fixed-speed strategy (Figure 5-9 (b)).

The key components used in this experiment are as follows (Figure 5-9 (c)):

(i) **Robot**: the TechMan (TM) robot 14;

(ii) **Force Toque sensor**: ATI Axia80-M50;

(iii) **Milling tool**: Dremel 4250 Rotary Tool 175 W, which runs at 35000 RPM spinning speed;

(iv) **Milling bit**: a general end mill from the Dremel tool for copper material cutting;

(v) **Milling fixture**: a customised aluminium fixture designed to fix the milling tool on the robot;

(vi) **Coil**: this is wound by a diameter 1 mm copper wire, which represents typical wire dimensions used in coil winding;

(vii) **Wire/coil fixture**: A 3D-printed plastic fixture is designed to hold the wires for the single wire test. The same setup was used for the coil milling test above. The coil winding is handmade on the fixture.

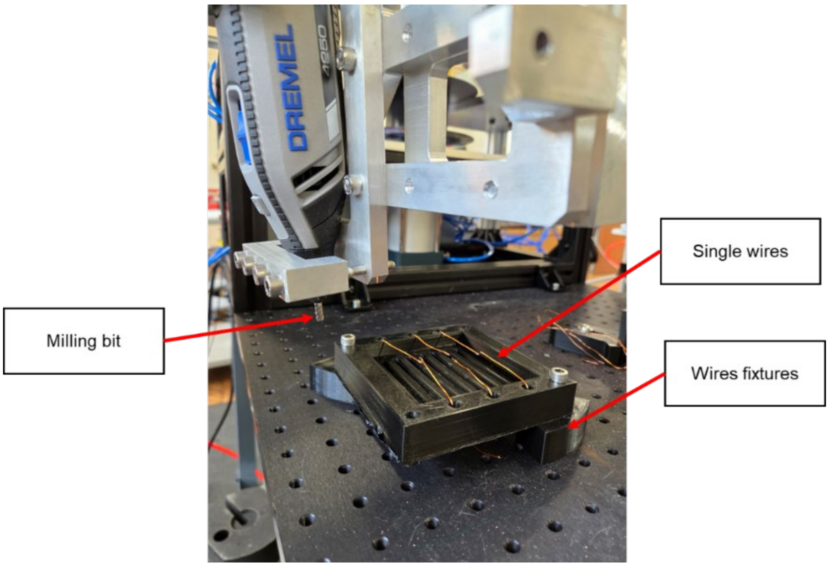

(a) Experiment setup for the single wires milling

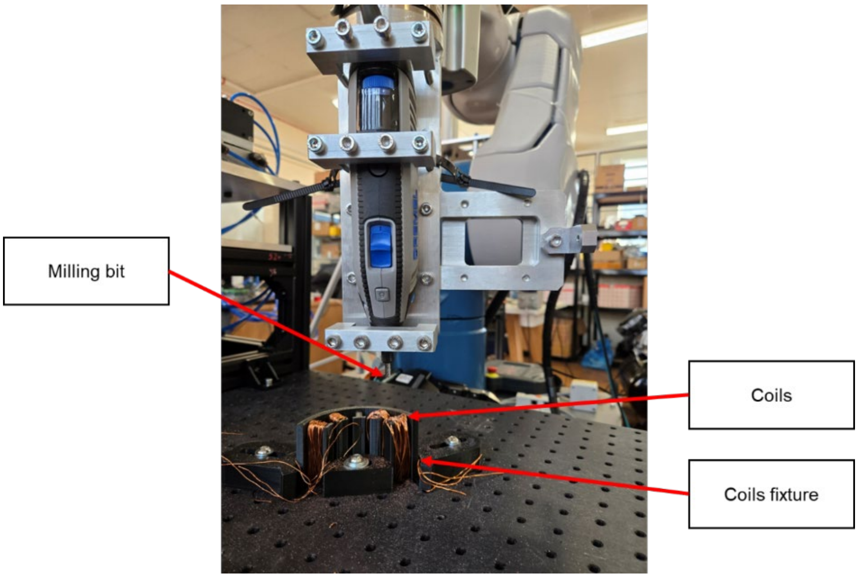

(b) Experiment setup for the coil milling

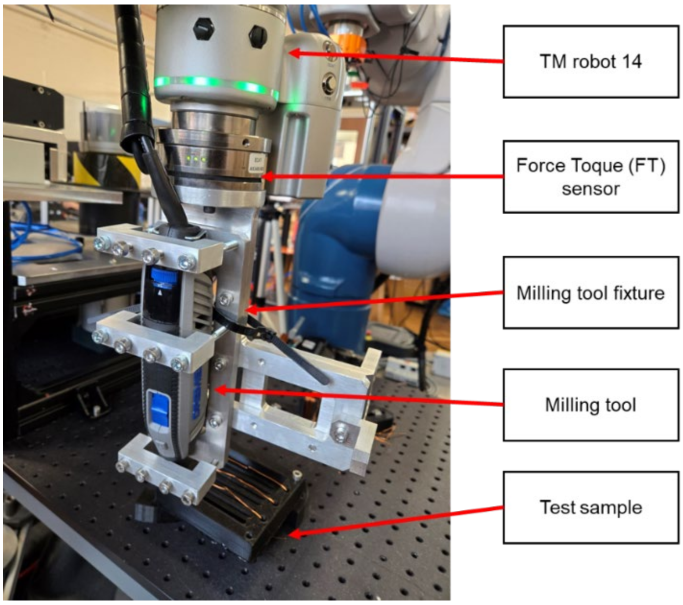

(c) Overview equipment set-up

Figure 5-9 Experimental setup for single wire milling and coil milling.

5.3 Results

5.3.1 Results of the Press-in task (T.1) and Press-on task (T.2)

This section presents key funding for the Press-in task (T.1) and Press-on task (T.2). The disassembly process is summarised as follows: In the Press-in task (T.1), (a) the hooks are initially closed and positioned to be inserted into the Bearing (large) (A.2), whereas the Front cover (A.1) is held by an electric gripper on the Staubli robot; (b) Once the hooks are fully inserted, they open to grip the Bearing (large) (A.2), and the robot releases its hold on the bearing; and (c) the bearing pusher then moves upwards and pushes out the Bearing (large) (A.2), while the Front cover (A.1) is retrained by the plate (Figure 5-10 (a)). In contrast, a reverse process is implemented to push out the Rotor set (B) in the Press-on task (T.2). In this case, the bearing pusher moves hooks downwards to push the Rotor set (B) out from the Bearing (large) (A.2), while the Front cover (A.1) is held in place by the plate (Figure 5-10 (b)). However, the maximum force applied during operation is calculated as 2240 N in the section 5.2.1. Unfortunately, the disassembly force is far greater than the range of the FT sensor in our lab. Video 1 about the Press-in task (T.1) and Video 2 about the Pess-on task (T.2) are available to show this link: https://doi.org/10.6084/m9.figshare.27934512.v2

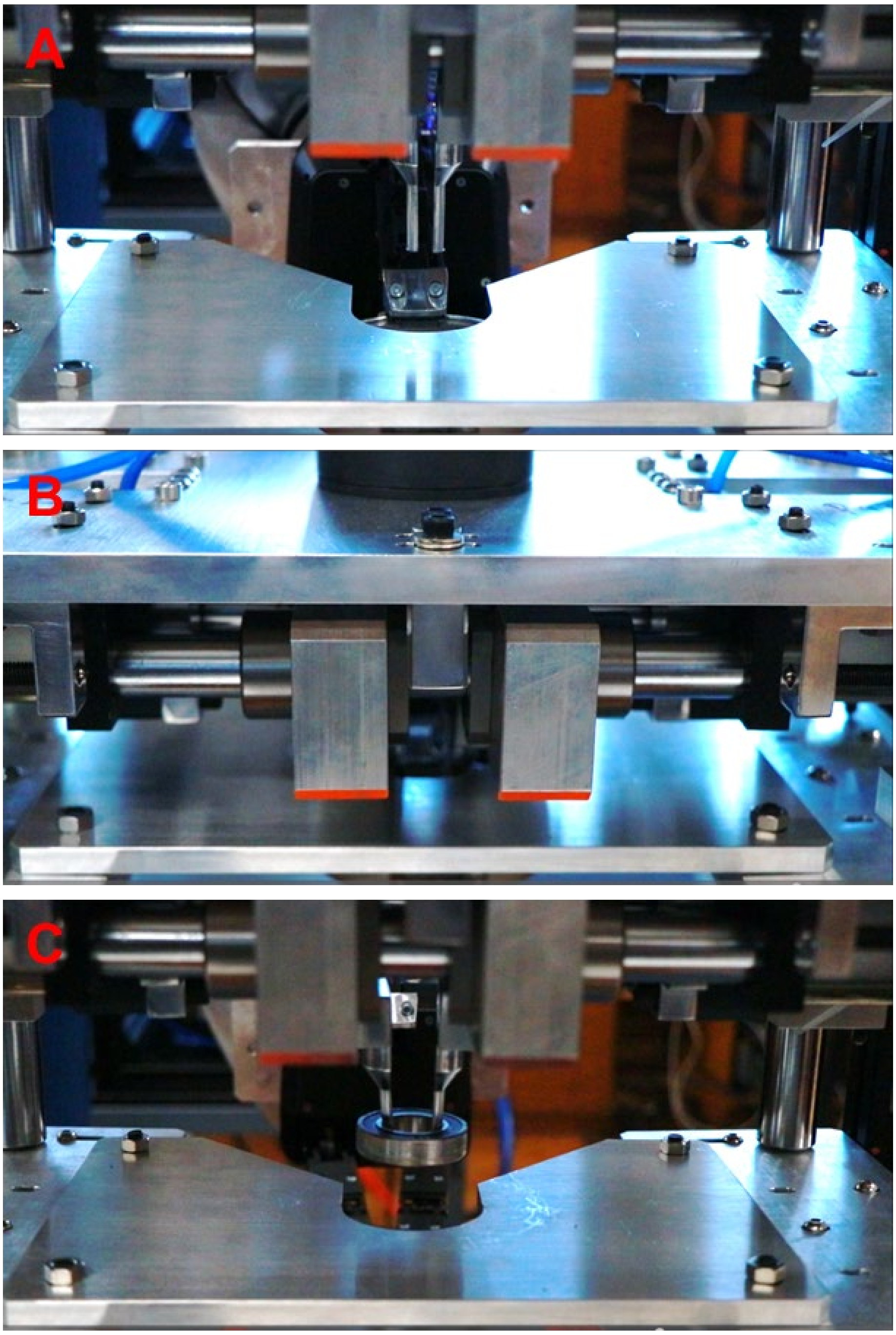

(a) Disassembly process of the Press-in task (T.1)

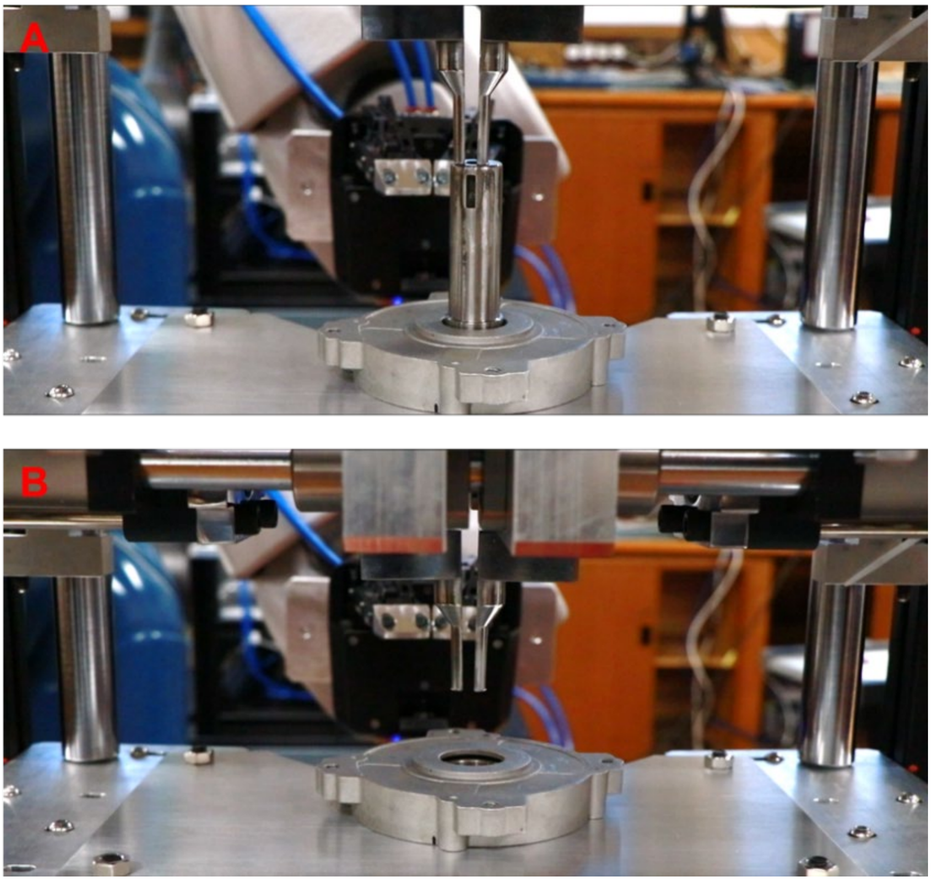

(b) Disassembly process of the Press-on task (T.2)

Figure 5-10 Press-in task (T.1) and Press-on task (T.2) results.

Several aspects of the design of the test setup could be improved. First, the pneumatic cylinder, which is used to remove the Bearing (Large) (A.2) or the Rotor set (B), may suddenly move at high speed when these components are released. This likely occurs when the required pushing or pulling force $(\mathrm{F_p})$ is very large. This issue arises because the airflow continues to be charged into the cylinder, resulting in a significant increase in the force. When the pushing/pulling force $(\mathrm{F_p})$ exceeds the frictional force $(\mathrm{F_f})$, the Bearing (large) (A.2) or Rotor set (B) is pulled out or pushed down. The cylinder continues moving momentarily at a high speed, which poses a risk of damage, such as the hooks colliding with the plate during the Press-on task (T.2). To address this issue, linear motors or hydraulic cylinders should be considered alternatives to pneumatic cylinders. These 2 options provide superior position control, particularly in applications requiring high disassembly forces, thus enhancing system reliability and safety. Second, the hooks are opened unevenly on the left and right sides. This issue occurs because the left and right hooks are individually driven by separate pneumatic cylinders, which may operate under differing pressure levels. An imbalance in air pressure causes the hooks to shift to one side during opening. To improve this design, pressure stabilisers might be implemented to balance the 2 different cylinders. Alternatively, replacing pneumatic cylinders with linear electric motors would provide improved position control and greater precision during operation. Third, most bearings are manufactured from metallic materials (steel), while the hooks are also made of steel. The friction of steel-on-steel conditions is relatively low, with a friction coefficient ranging from 0.5–0.8 (Engineering ToolBox, n.d.). Therefore, in the Press-in task (T.1), the bearing has a risk of slipping out from the hooks due to low friction between the 2 steel surfaces when the hooks are opened. To solve this problem, a friction-enhancing solution can be applied. For example, hooks can be coated with high-friction materials such as rubber. Alternatively, knurling could be machined on the surface of the hooks to improve grip strength and reduce the risk of slippage during operation.

5.3.2 Results of coil disassembly tasks (T.4)

This section discusses the results of coil milling through 2 different tests, including single copper wire milling and coil milling.

Test 1 evaluated the milling performance of a single copper wire at 50% and 100% robotic speeds (Figure 5-11). The resulting milling forces are determined by the FT sensor, while the positions logged by the robot correspond to Cartesian coordinates. First, Zone A demonstrates that robot movement has no significant effect on the milling force at 50% robotic speed. The slight vibration observed in the force is attributed to the spinning motion of the cutting tool. Second, Zone B indicates that the robot moves forward, pulling the copper wire before the milling process begins. A significant increase in the milling force is observed once the milling tool engages with the wire (Figure 5-11 (a)). Finally, the wire breaks when the milling force reaches the peak (approximately 18 N) in Zone C. After the wire breaks, the milling force decreases back to the baseline. In contrast, at 100% robotic speed, Zone A shows that the robot's movements influence the milling force at the start because of high acceleration. A similar observation is made in Zone C, where the robot moves away after the milling process (Figure 5-11 (b)). Notably, the maximum milling force at 100% robotic speed is approximately 14 N, which is lower than the value of approximately 18 N at 50% robotic speed. This shows that wire pulling is reduced as the milling bit approaches. Block 1 shows that copper melting occurs when the wire is pulled by the milling bit. However, no material melting is observed in block 2 when the pulling is decreased (Figure 5-11 (c)). Video 3 about single wire cutting at 50% speed and Video 4 about single wire cutting at 100% speed are available on this link:

https://doi.org/10.6084/m9.figshare.27934512.v2

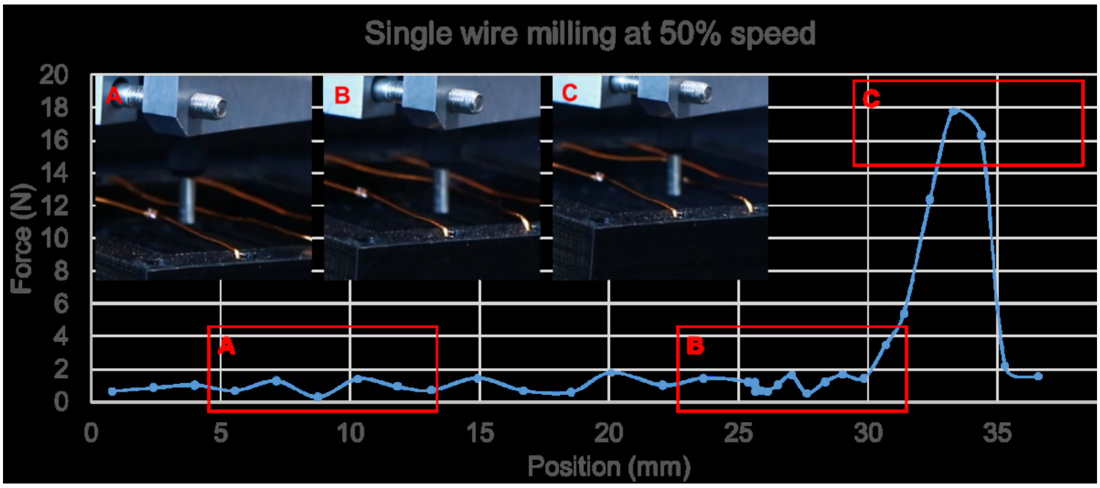

(a) Cutting forces and positions in single wire milling at 50% robot speed

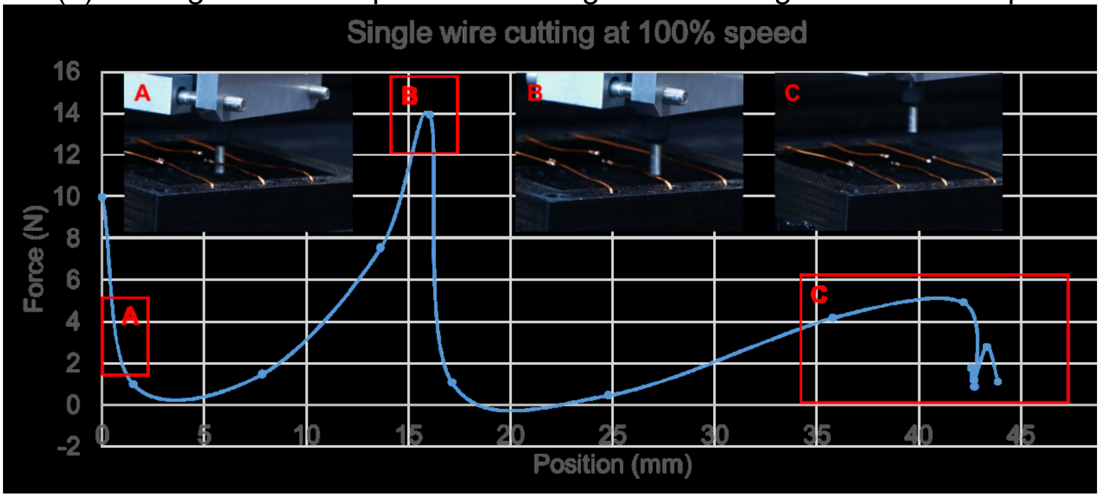

(b) Cutting force and positions in single wire milling at 100% robot speed

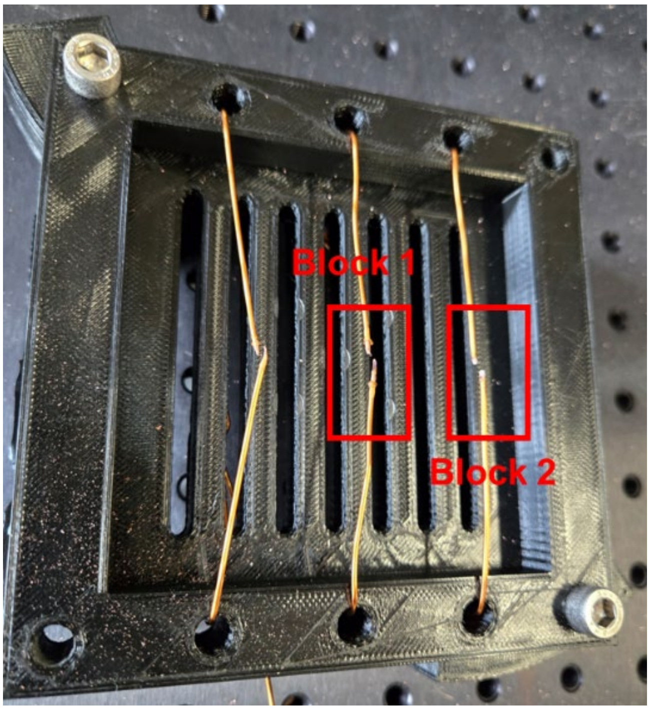

(c) Results of wire cutting at 50% and 100% speed

Figure 5-11 Results for single wire milling.

Test 2 evaluates 2 scenarios in coil milling: (1) running the TM robot via the force control strategy, where the robotic speed adjusts dynamically on the basis of the milling force, and (2) running the robot at a fixed speed.

In terms of the force control strategy, the robot has difficulty moving forward at a high speed (100% robot speed) in the milling process, even with a cutting depth of 0.55 mm. At 100% robot speed, the milling tool hits the coil and jumps between wires. Consequently, the robot is stuck by copper wires of coils even if the milling bit continues spinning. This leads to the stopping of robot execution and errors in the robotic operation system. All recorded data are lost because of errors in the system. The reason why “hits” and “jumps” occur at high robotic speeds is because of communication delays between the robot and the FT sensor. To explain this error, the author reviewed robot operations during the coil milling process. The process operates by the robot reading force data from the FT sensor; then, the robot adjusts its speed on the basis of the force data to control its movements. This feedback loop continues until the milling process is completed. However, even when the robot detects large forces, there is a delay of several seconds before the speed adjustment is made. During this interval, the robot continues to move at high speeds, resulting in “hits” and “jumps”. Owing to unstable robot performance and data loss, this force control strategy is considered an unsuccessful solution for coil disassembly.

With respect to coil milling at a fixed robotic speed of 5% and a 0.55 mm depth of cut, the robot’s performance is significantly more stable than that of the force control strategy. The final second of the milling process and the last process are analysed in terms of positions and forces (Figure 5-12). Zone A represents the milling operation during the last second process. Zone B illustrates a significant increase in force along the Z direction (Figure 5-12 (a)). This force increase is caused by the inability of the end mill (milling bit) to cut vertically, resulting in the bit being milled to “sit” on the coils when the robot moves downwards. The same happens in the last milling loop (Figure 5-12 (b)). Zone C corresponds to the moment when the milling bit contacts the wires being cut. The wires vibrate because of the spinning milling bits, which is further evident in Zone A, where the resultant force decreases significantly when the milling bit is not in contact with the wires (Figure 5-12 (b)). The vibration results in an increase in the cutting force again while the milling bit touches the wires in Zone

C (Figure 5-12 (b)). The videos of the coil cutting handmade coil, operating with the force control strategy (Video 5) and with the fixed-speed strategy (Video 6), are available on this link: https://doi.org/10.6084/m9.figshare.27934512.v2

Blocks 1 and 2 show the milling results achieved via the force control strategy and the fixed-speed strategy (Figure 5-12 (c)), respectively. In block 2, approximately 90% of the copper wires, as highlighted in the yellow circle, are successfully cut off. However, only approximately 20% of the wires (highlighted in the yellow circle) are cut off in block 1. This is because “hits” and “jumps” occur in the force control strategy so that only limited areas of wires are cut off, leaving most of the areas unprocessed. Additionally, approximately 10% of the wires near the edge of the fixture are not processed to prevent damage to the fixture (highlighted green cycle). One potential solution is to use a smaller milling bit to cut the wires in these areas near the edge of the fixture. Nevertheless, this approach carries the risk of damaging other components during the process, such as the stator. As a result, manual cutting is necessary to remove the remaining wires from the stator.

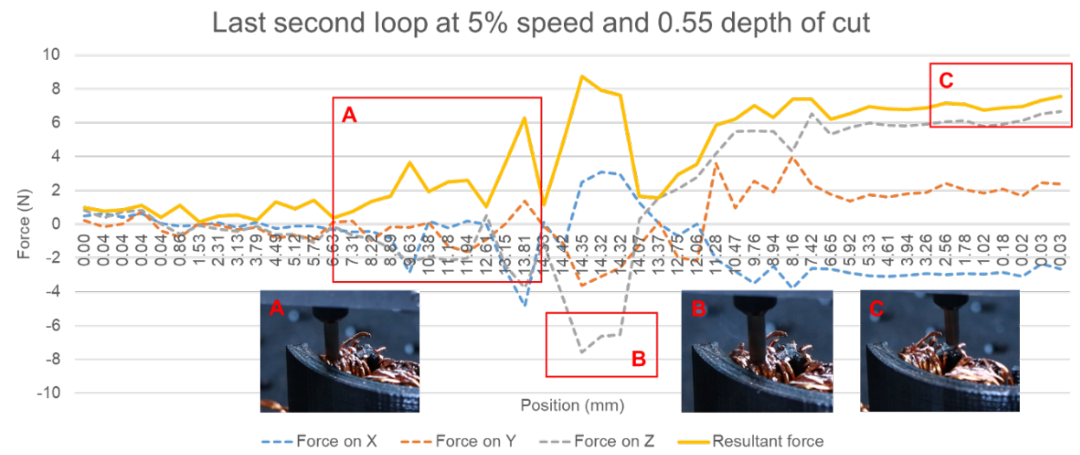

(a) Milling process in the last second loop at 5% robotic speed and 0.55 mm depth of cut

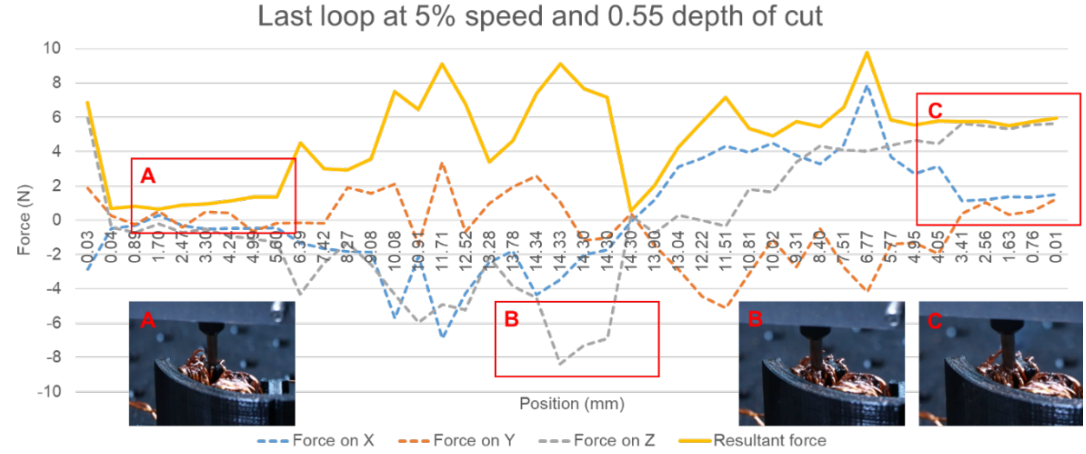

(b) Milling process in the last loop at 5% robotic speed and 0.55 mm depth of cut

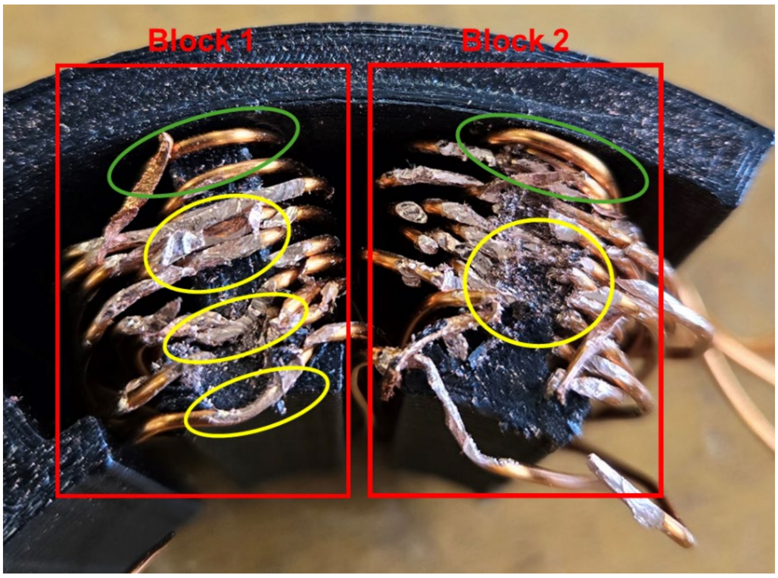

(c) Coils after milling

Figure 5-12 Results for coil dummy milling.

5.4 Summary

In conclusion, this chapter focuses on 3 different tasks in motor disassembly, including the Press-in task (T.1), the Press-on task (T.2) and the Coil disassembly tasks (T.4). The Press-in task (T.1) investigates the disassembly of the bearing (large) (A.2), which is pressed into the Front cover (A.1). The Press-on task (T.2) studies the disassembly of the Rotor set (B), which is pressed onto the Front cover (A.1). The calculated disassembly force is 2240 N between the Rotor set (B) and the Bearing (large) (A.2), assuming that the interference value (Z) of 10 is H7/k6 in hole-based tolerance or K7/h6 in shaft-based tolerance. The experiments successfully validated the Press-in task (T.1) and Press-on task (T.2). However, a force sensor capable of determining a large force of 2240 N was unavailable for recording the disassembly force in the laboratory.

Improvements should be considered in the design of the Press-on task (T.1) or Press-in task (T.2). The pneumatic cylinders demonstrate low positional accuracy because of unstable pressures. Future designs could consider linear electric motors, which offer higher precision despite being more expensive. Additionally, metallic hooks can slip, making it difficult to hold the inner surfaces of the steel bearing so that high-friction materials, e.g., rubber, might be considered for use on the hooks' contact surfaces to improve grip strength and reliability.

This chapter also introduces the Coil disassembly task (T.4), focusing on single copper wire cutting at different robotic speeds and the performance of various control strategies for coil cutting. Compared with that at 100% robotic speed, the cutting force at 50% robotic speed is increased by approximately 22.22% because of wire pulling. There are 2 conditions for increasing the cutting force without milling. (i) During robot movement, high acceleration causes the cutting force to increase from approximately 2 N to 6 N at 100% robotic speed, even when the milling process has not started. (ii) The milling bit contacts the cut wires, leading to an increase in the cutting force from approximately 2 N to 10 N.

The author developed two methods for the coil disassembly process. One is a milling coil at a constant robotic speed of 5%, and the other is a force control strategy in which the robotic speed is dynamically adjusted on the basis of the cutting force determined by the FT sensor during the milling process.

The maximum cutting force, set to 80% of the force of material failure, was determined via the FE method, which was based on the milling bit. Both methods were validated on a dummy coil made of 0.8 mm diameter copper wires. The robot exhibited unstable motion at a depth of 0.55 mm at 100% speed, causing “hits” and “jumps” during the milling process. These uncertain movements led to uncertain damage to the stator and only partial cutting of wires. Therefore, the instability and risk of damage render this method unsuccessful for coil milling on the TM robot.

Fortunately, the fixed-speed method demonstrated superior performance in robotic coil disassembly. The robot's motion remained stable at lower speeds (5% robotic speed and 0.55 mm depth of cut), effectively eliminating unpredictable milling actions that could damage other components. This method successfully cuts most of the wires, demonstrating its reliability for the task. However, wires located near the outer edge of the stator are difficult to cut off and risk damaging stators. This might require manual cutting by using pliers to fully remove the coils from the stator after robotic coil disassembly.

Chapter 6 Design of a robotic cell for electric motor disassembly

6.1 Problem description

Each task for DC brushless motor disassembly has been reviewed and studied in previous chapters. In this chapter, a robotic cell is developed to automate electric motor disassembly. Both manual disassembly and robotic disassembly processes for the DC brushless motor are presented and critically analysed, highlighting the advantages, challenges, and potential improvements for automation.

6.2 Methodology

All the tasks are analysed in chapters 3, 4 and 5. This section highlights how these developed methodologies and models are implemented in the design of a robotic cell for automating the disassembly process of a DC brushless motor:

- First, to automate the Press-in task (T.1) and Press-on task (T.2), the developed model provides the disassembly force required from the actuators. The clamping force to hold the stator and the holding force to hook the bearing are also calculated based on the disassembly force. These calculations, which are integrated with at least a 30% safety factor, guide the selection of actuators suitable for these tasks.

- Second, to automate the removal of the Rotor set (B) with permanent magnets from the Stator set (C.13) in the Unplugging task (T.3), the key parameters are the disassembly force and the optimised position where the disassembly force is minimised. These factors are considered in the design: (i) the material magnetic permeability of the stator is calculated by measuring the forces as a single magnet approaches the stator and recoding the distances between them. (ii) Then, the magnetic permeability data are used to calculate the disassembly force and locate the optimal position for force application on the Stator set (C.13) in the developed MMF model. Actuators are then selected to meet the required disassembly forces. (iii) The robot calculates the exact position based on the relative position and its frame coordinates. It then moves to this position to remove the Rotor set (B) from the Stator set (C.13).

- Third, to automate the Coil disassembly task (T.4), key parameters are set on the basis of the results in Chapter 5, including 5% robotic speed, a 0.55 mm cutting depth and a zigzag milling path (Figure 5-7).

- Fourth, the Unscrewing task (T.5) is well developed and involves positioning and unfastening processes. The TM robot provides a camera positioning function and I/O control for the external device (screwdriver). In the setting process, one of the screws is marked for identification by the camera. In the robotic operation process, the camera provides the positions of all the screws after it identifies all the screws on the motor. The camera relays the screw positions to the robot, which then activates an external screwdriver to unfasten four screws based on the provided coordinates.

- Fifth, the robotic Pick and place task (T.6) is well developed and uses a robot-teaching method, in which the human operator controls the robot to grip different objects and record positions.
- Finally, these tasks are sequenced according to the order in section 1.2 to generate a disassembly sequence for the robots. Both robots are then programmed to follow this sequence systematically.

6.3 Experiments

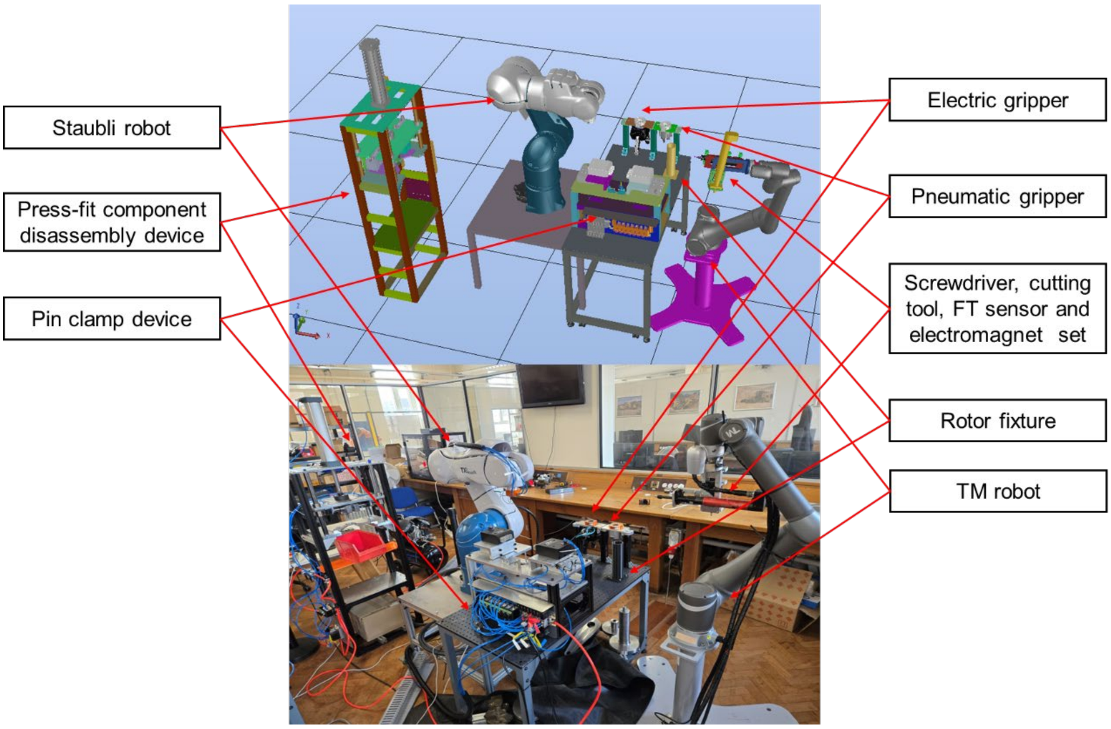

Figure 6-1 Overview of a robotic cell for motor disassembly.

A robotic cell is designed for the automated disassembly of DC brushless motors (Figure 6-1), including key components: 1 Staubli collaborative robot, 1 Techman (TM) collaborative robot, 1 electric gripper, 1 pneumatic gripper, 1 rotor fixture, 1 press-fit component disassembly device, 1 pin clamp device and a set of tools of 1 screwdriver, 1 cutting tool, 1 force torque (FT) sensor and 1 electromagnet. The Staubli robot is designed to execute the Pick and place task (T.6) and the Unplugging task (T.3) with precision and adaptability. The Stabuli is equipped with a tool changer, enabling it to operate with 2 grippers (the electric gripper and the pneumatic gripper) to grasp different objects. The electric gripper has 3 fingers, facilitating flexible gripping poses to accommodate objects with irregular geometries. Its wide gripping range makes it particularly suitable for handling complex components, such as the Front cover (A.1). However, the gripping force is only 70 N (Robotiq, n.d.). In contrast, for a gripping cylinder-shaped object, the Rotor set (B), e.g., the pneumatic gripper, provides a maximum 1,005 N gripping force (YHDFA, n.d.). This is particularly used on the Unplugging task (T.3) to remove the Rotor set (B) with permanent magnets from the Stator set (C.13).

The TM robot is specifically designed to address the Coil disassembly task (T.4) and Unscrewing task (T.5). It is equipped with a set of tools, including 1 screwdriver, 1 cutting tool, 1 electromagnet and 1 Force Torque (FT) sensor. The pin clamp device and press-fit component disassembly device are designed to address the Press-in task (T.1) and Press-on task (T.2). The Pin clamp device functions as a pneumatic vice to clamp the motor from the sides while simultaneously pushing the Rotor set (B) out from the Stator set (C.13). The Press-fit component disassembly device is designed to push out the Rotor set (B) from the Front cover (A.1) and pull-out Bearing (large) (A.2) from the Front cover (A.1). The rotor fixture is a 3D-printed component that stores the Rotor set (B) with the Front cover (A.1) once they are disassembled from the stator. The detailed designs of this robotic cell are shown in Appendices A - F, including the mechanical system, electric system, pneumatic system and robot programme. This robotic cell fully disassembles the DC brushless motor. The time required for the robotic disassembly process and manual disassembly process are analysed.

6.4 Results

This section outlines the process of motor disassembly within the designed robotic cell and provides a comparative analysis of robotic disassembly versus the manual process.

6.4.1 Robotic disassembly process

(a) Step1: Staubli robot moves to home position

(b) Step 2: Staubli robot picks the pneumatic gripper

(c) Step 3: Staubli robot grips the electric motor

(d) Step 4: Unscrewing task

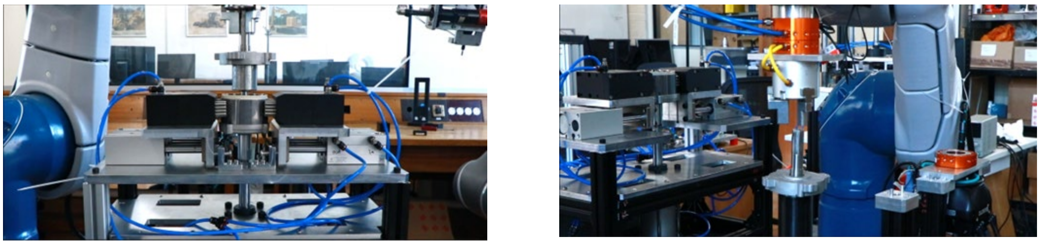

(e) Step 5: Unplugging task

(f) Step 6: Staubli robot places the front cover and rotor set

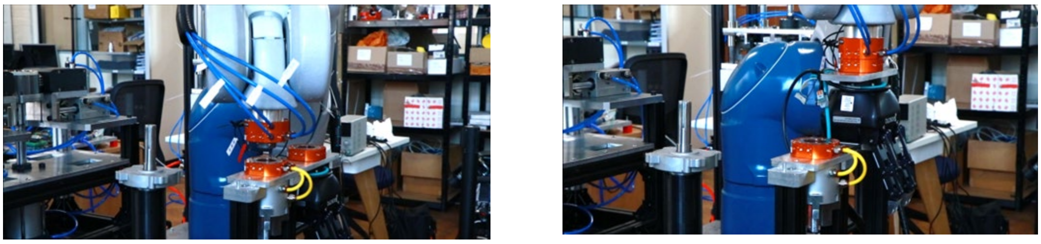

(g) Step 7: Staubli robot places the pneumatic gripper

(h) Step 8: Staubli robot picks the electric gripper

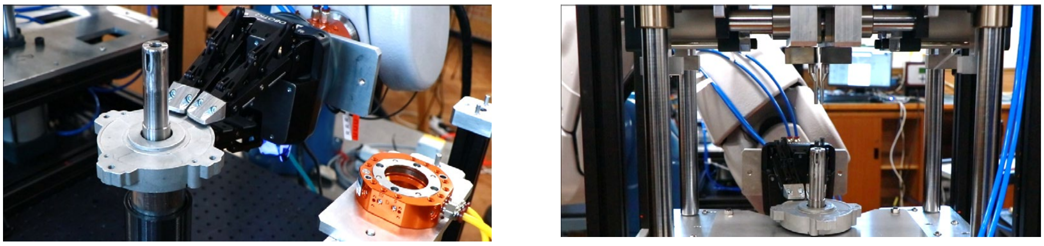

(i) Step 9: Staubli robot picks the front cover and rotor set

(j) Step 10: Staubli robot places the front cover and rotor set

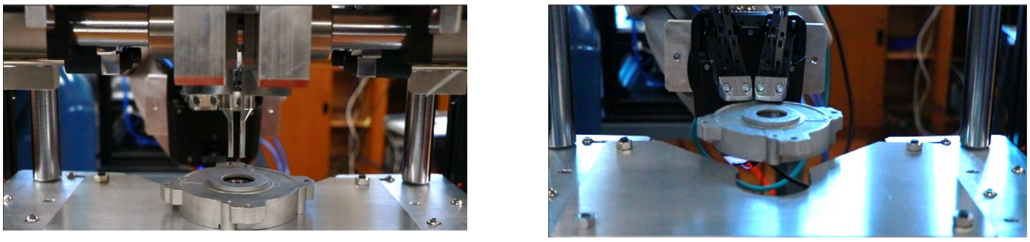

(k) Step 11: Press-on task

(l) Step 12: Staubli robot picks the front cover

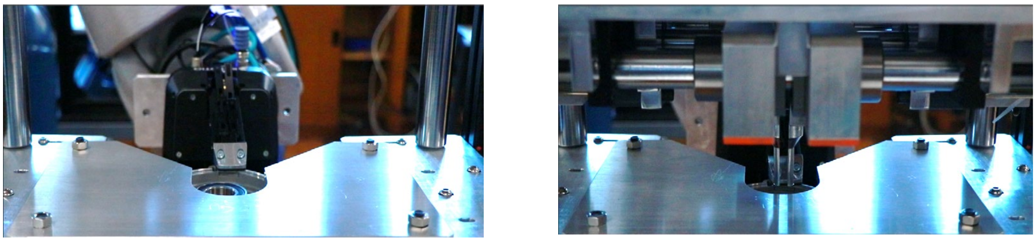

(m) Step 13: Staubli robot places the front cover underneath the place

(n) Step 14: Press-in task: hooks inserting

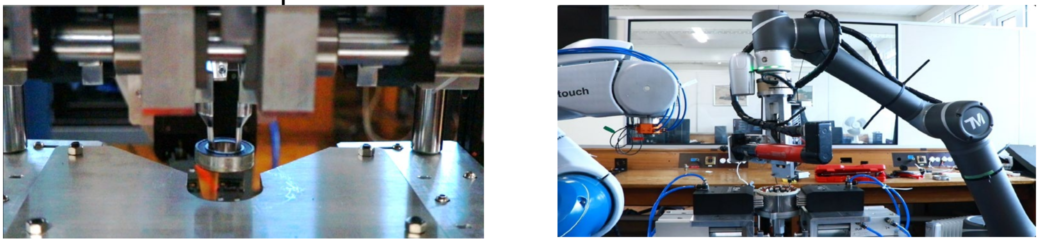

(o) Step 15: Press-in task: hooks pulling out

(p) Step 16: coil disassembly: overview

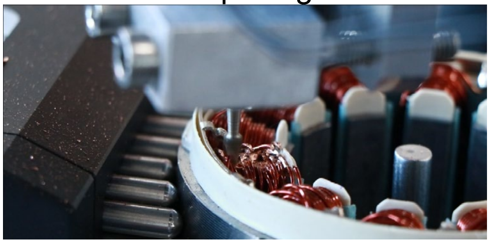

(q) Step 16: coil disassembly: view in details

Figure 6-2 Robotic disassembly process.

The robotic disassembly process is introduced in detail below (Figure 6-2).

1. **Step 1**: The process begins with the initialisation program for the Staubli robot (M.1). Before executing tasks, the Staubli robot (M.1) moves to the home position, preparing for motor disassembly (Figure 6-2 (a));
2. **Step 2**: The Staubli robot (M.1) picks up the pneumatic gripper (M.10) and returns to its home position (Figure 6-2 (b)). The attachment mechanism involves a tool change (robot side) (M.2) inserting into the tool change (tool side) (M.9), where locking balls are engaged by airflow. The pneumatic gripper (M.10) is driven via airflow through both tool changes (M.2 and M.9).
3. **Step 3**: The Stabuli robot (M.1) moves pneumatic grippers (M.10) to grip the shaft of the motor (Figure 6-2 (c)).
4. **Step 4**: A collaborative operation in 2 robots is performed to execute the Unscrewing tasks (T.5) (Figure 6-2 (d)). The Stabuli robot (M.1) holds the motor in a certain position until the TM robot (M.3) finishes the Unscrewing task (T.5). The TM robot (M.3) locates the positions of 4 screws (E.1 - E.2) with a 2D camera (M.4) and engages an electric screwdriver (M.5) for unfastening. This process is repeated 4 times to remove all 4 screws (E.1 - E.2).
5. **Step 5**: The Staubli robot (M.1) and Pin clamp device execute the Unplugging task (T.3) to separate the Rotor set (B) with permanent magnets from the Stator set (C.13) (Figure 6-2 (e)). The clamps cylinders (M.15) push 2 pin clamps (M.14) to hold the motor, whereas the Staubli

robot (M.1) moves the motor in position. Then, the Staubli robot (M.1) and the Push cylinder (M.16) simultaneously move up to plug out the Rotor set (B) with the Front cover (A.1) and the Bearing (large) (A.2).

6. **Step 6**: The Rotor set (B), which is fixed with the Front cover (A.1) and Bearing (large) (A.2), is placed into a Rotor fixture (M.13) by the Staubli robot (M.1) (Figure 6-2 (f)). Simultaneously, the Stator set (C.13) remains clamped until the coil disassembly task (T.4) is completed.
7. **Steps 7 and 8**: The Staubli robot (M.1) places down the pneumatic gripper (M.10) (Figure 6-2 (g)) and picks up the electric gripper (M.10) (Figure 6-2 (h)). Two grippers are designed for different purposes. The pneumatic gripper (M.10) generates a very large gripping force (approximately 359 N) to hold the cylindrical objects in the high-payload task, grip the shaft and remove the Rotor set (B) with permanent magnets in the Unplugging task (T.3), e.g., In contrast, the electric gripper (M.11) has a larger range (approximately 155 mm) to grip different shapes of components, such as the Front cover (A.1); however, it only offers an approximately 70 N gripping force.
8. **Steps 9 and 10**: The Staubli robot (M.1) moves to grip the Front cover (A.1) with the Rotor set (B) from the rotor fixture (M.13) by using the electric gripper (M.11) (Figure 6-2 (i)). These components are then placed onto the plate (M.25) of the Press-fit component disassembly device (Figure 6-2 (j)).

9. **Step 11**: This is the Press-on task (T.2) to remove the Rotor set (B) from the Front cover (A.1) (Figure 6-2 (k)). The hooks (M.21) are closed by the bearing clamp cylinders, and the Rotor set (B) is pushed out by the hooks driven by the bearing pusher (M.19). The Front cover (A.1) with the Bearing (large) (A.2) still remains on the plate (M.25).
10. **Steps 12 and 13**: Staubli (M.1) grips the Front cover (A.1) (Figure 6-2 (l)) and the Bearing (large) (A.2) and then holds them underneath the plate (M.25) (Figure 6-2 (m)).
11. **Steps 14 and 15**: This is the Press-in task (T.1) to remove the Bearing (large) (A.2) from the Front cover (A.1). First, the hooks (M.21) are closed by the bearing clamp cylinders (M.20) and are moved downwards by the bearing pusher (M.19) to be inserted into the Bearing (large) (A.2) (Figure 6-2 (n)). Second, the hooks are opened by the bearing clamp cylinders (M.20) to hold the Bearing (large) (A.2); meanwhile, the Staubli robot (M.1) releases the Front cover (A.1) and moves back to a safe position. Finally, the Bearing (large) (A.2) is pulled up by the bearing pusher (M.19) (Figure 6-2 (o)).
12. **Step 16**: Coil disassembly (T.4) is completed by the TM robot (M.2) via the cutting tool (M.7) (Figure 6-2 (p) and (q)).

A video (Video.7) demonstrating the robotic disassembly process can be accessed via the provided link:
https://doi.org/10.6084/m9.figshare.27934512.v2

6.4.2 Manual disassembly process

(a) Manual step 1: Unscrewing task (T.3)

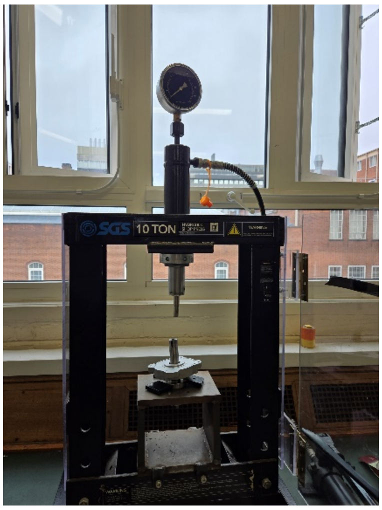

(b) Manual step 3: Press-on task (T.2)

(c) Manual step 4: Press-in task (T.1) - A

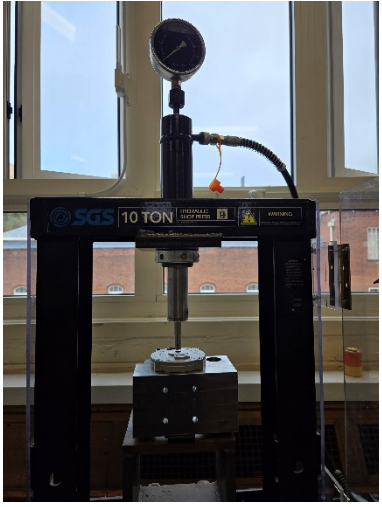

(d) Manual step 4: Press-in task (T.1) - B

(e) Manual step 4: Press-in task (T.1) - C

(f) Manual step 5: Coil disassembly

Figure 6-3 Manual disassembly process.

The manual disassembly process for this motor is introduced as follows (Figure 6-3):

1. **Manual step 1**: Four screws (E.1 - E.4) are unfastened via an M5 Allen key, completing the Unscrewing task (T.5) (Figure 6-3 (a));
2. **Manual step 2**: This is the Unplugging task (T. 3) used to separate the Rotor set (B) from the Stator set (C.13). The shaft on the Rotor set (B) is held with one hand, and the Stator set (C.13) is held with the other hand. The Rotor set (B) is manually unplugged (Figure 6-3 (b));
3. **Manual step 3**: For the Press-on task (T.1) to remove the Rotor set (B) from the Front cover (A.1), the rotor set (B) is pushed out via a manual hydraulic pump (Figure 6-3 (c));
4. **Manual step 4**: This Press-in task (T.2) removes the Bearing (small) (D.1) from the End cover (D.2). In action 1, a bearing holder is inserted into the Bearing (small) (D.1). Action 2 rotates the end of the holder clockwise to expand it until the inner surface of the Bearing (small) (D.1) is held tightly (Figure 6-3 (c)). Action 3 pushes out the bearing holder with the Bearing (small) (D.1) via a manual hydraulic pump (Figure 6-3 (d) and (e)). Action 4 rotates the end of the bearing holder anticlockwise to release the Bearing (small) (D.1);
5. **Manual step 5**: The manual Coil disassembly task (T.4) involves removing the copper Coils (C.1 - C.12) from the Stator set (C.13). The

Dremel 4250 Rotary Tool (175 W) operating at 35,000 RPM is used to cut through the coils (Figure 6-3 (f)).

The videos for both robotic coil disassembly (Video 8) and manual processing (Video 9) are available on this link:

https://doi.org/10.6084/m9.figshare.27934512.v2

6.4.3 Discussion: Both robotic and manual disassembly

This section analyses the outcomes of the robotic disassembly and manual disassembly processes. All the components of the motor were successfully disassembled (Figure 6-4 (a)). First, the cut-off Coils (C.1 - C.12) are easily detached from the Stator set (C.13). Compared with the manual milling process, the robotic milling process eliminates approximately 90% of the copper wires on the coil. Three wires are not fully cut off near the outer edge of the Stator set (C.13); thus, these wires require manual removal via pliers (Figure 6-4 (b)). Despite this limitation, the robotic milling process is stable (shown in Appendix H for the cutting force and position recording), ensuring that other components are not damaged. Additionally, the robotic milling process produced uniformly shaped cut-off coils, which were easier to remove entirely. The manual milling process achieved complete removal of all the copper wires; nevertheless, owing to the instability of hand-controlled operations, the Stator set (C.13) sustained damage during the process. After unfastening, all Screws (E.1–E.4) remained locked within the End cover (D.2). This finding indicates that further handling steps are required to fully extract the screws during both processes. A steel ring was installed between the Bearing (small) (D.1) and the End cover (D.2). However, the purpose or function of this ring is unclear, suggesting the need for further investigation. Finally, lubricants, which are applied during the bearing installation process, become sticky solids on the inner surface of the hole and outer surface of the bearing. This condition may affect the ease of bearing removal and could necessitate additional cleaning procedures after disassembly.

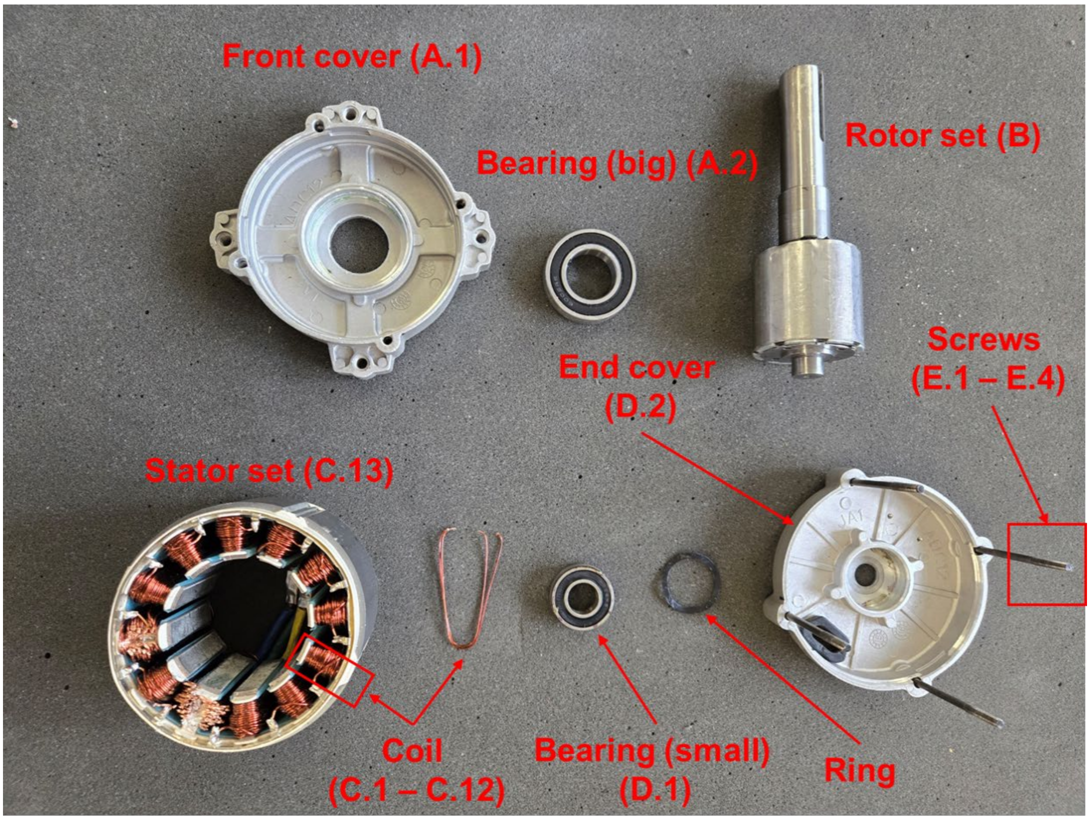

(a) Components after disassembly

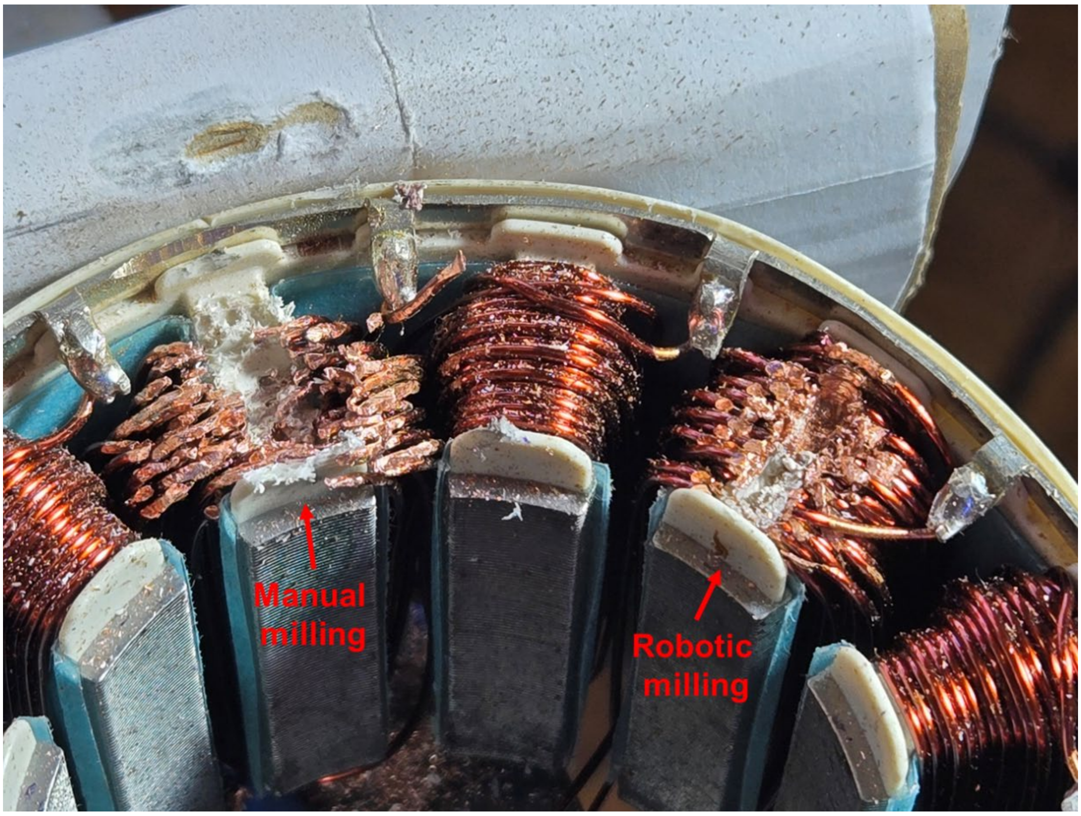

(b) Manual milling process and robotic milling process

Figure 6-4 Components after disassembly.

The disassembly time for the robotic process was recorded and is illustrated in Figure 6-5. The robotic disassembly covers all tasks (T.1 - T.6) in steps 1 - 16. Some assumptions are made to simplify the experiment. In step 16 (Coil disassembly (T.4)), the robot cut off one coil during the milling process. The time required for this single operation was recorded, and it was assumed that the remaining 11 coils would require the same amount of time for milling. Similar to the Unscrewing task (T.5) in step 4, the robot unfastens only 1 screw. The disassembly times for the remaining 3 screws are assumed to be identical to that of the first screw. The robotic disassembly excludes step 17, which is the Press-in task (T.2) to remove the Bearing (small) (D.1) from the End cover (D.2). Step 17 should be performed manually to determine time. The robotic disassembly time of steps 13–15 (Press-in task (T.1) to remove the Bearing (large) (A.2) from the Front cover (A.1)) is assumed to be the same as that of step 17 (Press-in task (T.1) to remove the Bearing (small) (D.1) from the End cover (D.2)).

However, the manual disassembly process only repeats partially to determine time, including step 4 (Unscrewing task (T.5)), step 5 (Unplugging task (T.3) to remove the Rotor set (B) from the Stator set (C.13)), steps 10 - 12 (Press-on task (T.2) to remove the Rotor set (B) the Front cover (A.1), step 16 (Coil disassembly task (T.4)) and step 17 (Press-in task (T.1) to remove from Bearing (small) (D.1) from the End cover (D.2)). To reduce the experiment time, the manual process only unfastens 1 screw and cuts 1 coil. The remaining processes are assumed to be the same. The manual disassembly time for step 17 (Press-in task (T.1) to remove the Bearing (small) (D.1) from the End cover (D.2)) is assumed to be the same as that for steps 13 - 15 (Press-in task (T.1) to remove the Bearing (large) (A.2) from the Front cover (A.1)).

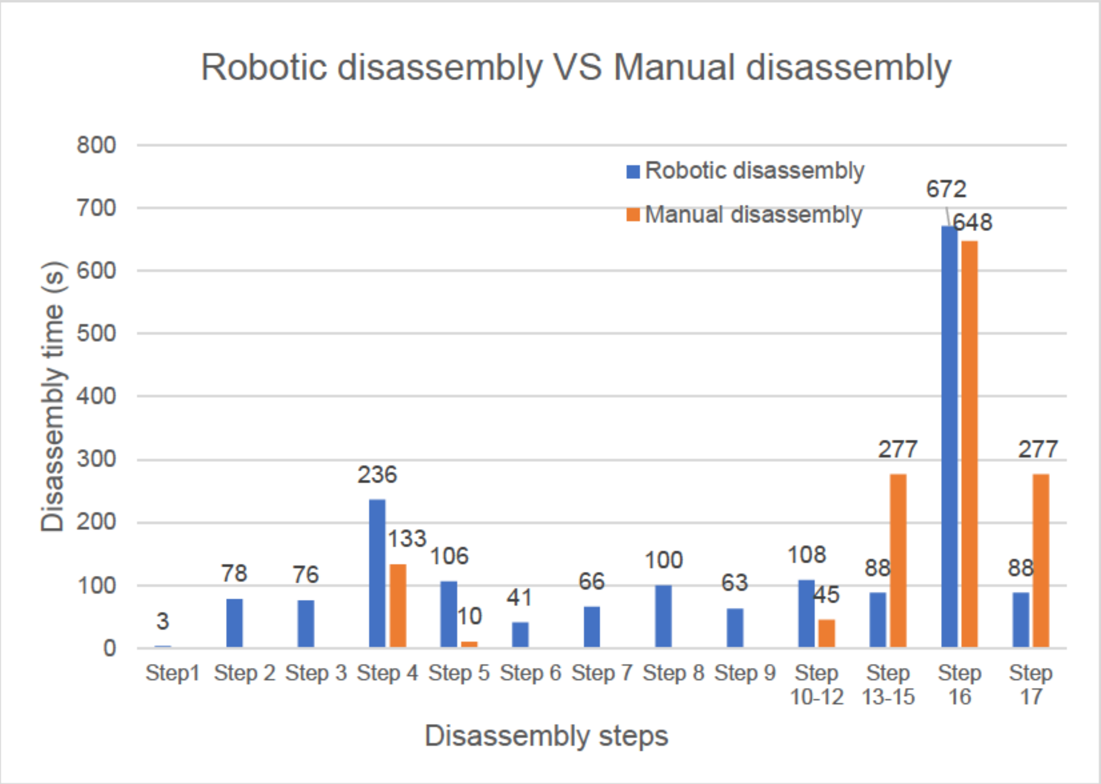

Figure 6-5 Robotic and manual disassembly times.

The total time for the robotic disassembly is approximately 1725 s, the Staubli robot operates at 25% speed, all pneumatic components in both the pin clamp device and the press-fit component disassemble at approximately 25% linear speed, and the TM robot operates at 5% robotic speed. The manual disassembly process takes approximately 1390 seconds. The time can be reduced to 885.69 s if the speed is increased to 100% for both robots and all pneumatic cylinders, excluding the Coil disassembly task (T.4), which remains at 5% robotic speed for safety considerations. As a result, the robotic disassembly process could be 56.93% faster than the manual process.

In summary, the manual disassembly process offers several advantages over the robotic disassembly process:

1. Reduced setup time: Manual disassembly does not require the time for (1) initialisation (step 1), tool changing (steps 2, 7 and 8) or Pick and place tasks (T.6) (step 3, step 9, step 10, step 12 and step 13);
2. Faster Unscrewing process: the manual Unscrewing process (T.5) is more efficient because it does not require camera positioning before unfastening execution;
3. The equipment costs are lower: manual disassembly only costs general hand tools and personal protective equipment (PPE). In contrast, robotic disassembly of electric motors requires specialised engineering designs and costly equipment, resulting in significantly higher overall costs.

However, robotic disassembly offers several key advantages:

1. Stable coil disassembly: Robotic coil disassembly provides a stable milling process operating with a fixed speed strategy, reducing the risk of damaging other components. Even if the time in manual coil disassembly is slightly faster (approximately 3.7% faster), it is unstable, resulting in damage to surrounding components, such as the Stator set (C.13). Additionally, copper-cutting chips present potential safety hazards to the eyes and breathing system, requiring workers to wear PPE such as glasses, gloves and masks properly. However, the robot struggles with cutting wires near the edge stator.
2. Quality in the Unplugging task (T.3): In step 5, manual disassembly takes approximately 10 seconds rather than approximately 106 seconds in the

robotic disassembly process. However, during manual disassembly, there is a risk of the Rotor set (B) contacting the inner surface of the Stator set (C.13). This is very risky for breaking both magnets on the Rotor set (B) and the Stator set (C.13). However, robotic disassembly ensures that the Rotor set (B) is removed at the force-optimised position without contacting the Stator set (C.13) to prevent damage.

3. Reduced time in the Press-in tasks (T.1): To remove the Bearing (large) (A.2) from the Front cover (A.1), robotic disassembly is significantly faster, requiring only approximately one-third of the time compared with manual disassembly. This efficiency is due to the specialised design of the Press-fit component disassembly device, which automates the process. In manual disassembly, workers have to rotate the bearing holder to hold the bearing and then push both the bearing and the holder out via a hydraulic pump. Robotic disassembly simplifies the manual process by using hooks driven by bearing clamp cylinders (M.20) to hold the bearing and a bearing pusher (M.19) to remove it.

6.5 Summary

In conclusion, this chapter introduces and compares both robotic disassembly and manual disassembly processes. A robotic cell is designed to automate disassembly tasks T.1 - T.6 via methodologies developed in Chapters 3 - 5. In terms of time efficiency, robotic disassembly is approximately 56.93% faster than manual disassembly when operating at 100% robotic speed. However, the manual disassembly process has advantages in specific areas: time efficiency for task initialisation, tool changing, Unscrewing task (T.5) and Place and pick tasks (T.6), and cost efficiency due to the limited need for specialised equipment.

In contrast, with respect to disassembly quality, robotic disassembly offers greater stability in the Unplugging (T.3) and Coil disassembly (T.4), minimising the risk of damage to other components. Additionally, robotic disassembly significantly outperforms manual processes in the Press-in task (T.1), requiring only one-third of the time due to its specialised design for handling bearings.

For future development, it is recommended that this robotic cell be tested with different types of electric motors to evaluate its versatility. Replacing pneumatic cylinders with electric actuators could improve position control and overall performance. Further advancements could focus on developing commercial-grade robotic cells suitable for industrial use.

Chapter 7 Conclusion

7.1 Conclusions

This research investigates the robotic disassembly of DC brushless motors, identifying six common disassembly tasks and developing a robotic solution for these tasks. The key tasks addressed are the Press-in task (T.1), Press-on task (T.2), Unplugging task (T.3), Coil disassembly task (T.4), Unscrewing task (T.5) and Pick and place task (T.6). On the basis of the literature review, the Unscrewing task (T.5) and Pick and place task (T.6) have been well studied in prior research, whereas the remaining tasks are explored in detail in this work.

The Unplugging task (T.3) aims to remove the Rotor set (B) with permanent magnets from the Stator set (C.13). In Chapter 3, an analytical model and an FE model are developed to determine the resultant magnetic force. The analytical model employs the MMF method, and the FE model employs 3D partial differential equations. Experimental validation shows that the resultant magnetic force is minimised at the centre of the stator when the magnetic fields are balanced. While the FE model provided highly accurate results in 3D models via COMSOL software on high-performance computing systems, the analytical MMF method offers a computationally efficient alternative with reasonable accuracy, requiring 99% fewer calculations. The MMF model can be implemented in a robotic program to calculate magnetic forces dynamically via robotic positioning.

To improve the accuracy of the MMF model, material hysteresis is determined experimentally in Chapter 4. A single magnet fixed on the robot is moved incrementally toward a steel hub while the distances and magnetic forces are recorded by the robot system and an FE sensor. These data were fitted to a 9th-order polynomial equation to model material hysteresis. Learned material hysteresis is then imported to an MMF model to predict the optimal positions where the magnetic forces are minimised. This improved MMF model can also solve the UMFP problem caused by uneven distributions of magnetic fields in 5 different scenarios. A 90% success rate for position prediction was validated in 10 tests in 5 defined UMFP problems. However, when half of the magnets are missing, prediction is less accurate in calculating magnetic forces because of geometry mismatches between the MMF model and the experimental setup.

The remaining 3 problems of Press-in task (T.1), Press-on task (T.2) and Coil disassembly task (T.4) are studied in Chapter 5. The Press-in task (T.1) defines that components are press-fitted and hidden in the other components, such as the Bearing (Large) (A.2) that is press-fitted into the Front cover (A.1). The Press-on task (T.2) represents the components that are press-fitted on the other components; for example, the Rotor set (B) is press-fitted on the Front cover (A.1). A model is developed to calculate the disassembly force to remove press-fit components, and the disassembly force is used to design 2 devices to remove these press-fit components, including the pin clamp device and the Press-fit component disassembly device. Both devices performed effectively in the experiments; unfortunately, the force determination during disassembly could not be recorded because of the absence of an FT sensor. Additionally, the Coil disassembly task (T.4) focuses on removing copper Coils (C.1 - C.12) from the stator set (C.13). Robotic milling using a standard cutting tool was identified as an effective method. Two control strategies were examined: the fixed-speed strategy and the force-control strategy. The force control strategy aims to minimise the cutting time by adjusting the robot’s speed based on the cutting force determined by the FT sensor; however, communication delays cause the robot to "hit" or "jump" during cutting, leading to robotic system errors. Thus, this force control strategy is unsuccessful. Fortunately, the fixed-speed strategy performs reliably to cut off wires on the coil, operating with 5% robotic speed and a 0.55 mm depth of cut. The fixed-speed strategy is considered an efficient method to remove the coil from the stator, preventing unnecessary damage to the components due to unpredictable motions.

Chapter 6 introduces how these developed models help design a robotic cell for DC brushless motor disassembly. Experiments validated both robotic disassembly and manual disassembly, and their differences were analysed. In terms of disassembly efficiency, the times for the robot and human operators are 885.69 s at 100% robotic speed and 1390 s, respectively. Additionally, robotic disassembly achieves superior quality in specific tasks, such as the Unplugging task (T.3) and Coil disassembly task (T.4). In the Unplugging task (T.3), the Rotor set (B) with permanent magnets is removed in the contactless condition from the Stator set (C.13), preventing damage to the magnets and stator caused by slipping. In the Coil disassembly task (T.4), robotic cutting operating with a fixed-speed strategy is more stable than manual cutting, preventing overcutting on the stator structure. However, the robotic system failed to cut 10% of the coil wires near the stator edge because of limited accessibility. These wires require manual cutting with pliers.

In conclusion, this study demonstrates the feasibility and advantages of robotic disassembly for DC brushless electric motors, particularly in terms of efficiency and component preservation. Limitations, such as inaccessible cutting areas and the absence of force determinations, highlight areas for future research. Further work is discussed in the next section.

7.2 Summary of contributions

The research work presented in this thesis made the following contributions:

- Identification of tasks of disassembly for permanent magnet DC brushless motor disassembly and investigation of difficulties and potential solutions in disassembly;
- Development of an analytical model for calculating the magnetic forces in the removal of a rotor with permanent magnets from a stator. This model has reasonable accuracy without requiring powerful computers and calculation time compared with the finite element method.
- Improved analytical model by implementing determination of magnetic hysteresis (B-H curve) can predicts the force optimal positions of disassembly.
- Potential solutions of the Press-fit component disassembly task and Coil disassembly task were developed and validated by experiments.
- A robotic cell was designed to compare manual and robotic disassembly. The robotic disassembly has advantages in quantities, precise and stable disassembly process, safety and disassembly time.

7.3 Future work

Although this thesis systematically studies the robotic disassembly of electric motors, several areas for future development are proposed to address limitations and further advance the field. First, the magnetic fields of magnets are determined by disassembling an assumption that the magnetic field distribution remains consistent across motors of the same model. However, the magnetic fields might differ in the same model because of manufacturing qualities, magnet damage and high-temperature damage. The ideal solution is to develop a determination method for magnetic fields without the disassembly of motors. Second, related to the coils removed from the stator, this paper develops a model to adjust the cutting force and cutting speed in the force control strategy, minimising the total cutting time. Unfortunately, the TM robot used in the experiments could not execute this force control strategy stably, exhibiting behaviours such as "hitting" and "jumping" during the cutting process. Future research should explore implementing this force control strategy on robots with superior dynamic performance, such as ABB, KUKA, or FANUC robots, to assess whether stability and precision can be enhanced. Finally, to transition this robotic cell to industrial applications, it is essential to test its performance on a variety of motor types, including induction motors, stepper motors with encoders, and others. These tests help identify the adaptability of the robotic cell to different designs and functionalities. Iterative product development on the basis of these evaluations would further optimise the system for broader industrial adoption.

7.4 Publication from this thesis

Part of the work undertaken in this thesis has already been published in the following journal:

Liang, C., & Pham, D. T. (2025). Robotic disassembly of permanent magnet electric motors. Royal Society Open Science.

References

Abdi, S., Abdi, E. and McMahon, R. (2015) ‘A Study of Unbalanced Magnetic Pull in Brushless Doubly Fed Machines’, *IEEE Transactions on Energy Conversion*, 30(3), pp. 1218–1227. Available at: https://doi.org/10.1109/TEC.2015.2394912.

Al Assadi, A. *et al.* (2022) ‘Machine learning based screw drive state detection for unfastening screw connections’, *Journal of Manufacturing Systems*, 65, pp. 19–32. Available at: https://doi.org/10.1016/j.jmsy.2022.07.013.

Andhare, P. and Rawat, S. (2016) ‘Pick and place industrial robot controller with computer vision’, in *2016 International Conference on Computing Communication Control and automation (ICCUBEA)*. *2016 International Conference on Computing Communication Control and automation (ICCUBEA)*, pp. 1–4. Available at: https://doi.org/10.1109/ICCUBEA.2016.7860048.

Bai, Z. *et al.* (2018) ‘Contact Pressure Algorithm of Multi-Layer Interference Fit Considering Centrifugal Force and Temperature Gradient’, *Applied Sciences*, 8(5), p. 726. Available at: https://doi.org/10.3390/app8050726.

Bdiwi, M., Rashid, A. and Putz, M. (2016) ‘Autonomous disassembly of electric vehicle motors based on robot cognition’, in *2016 IEEE International Conference on Robotics and Automation (ICRA)*. *2016 IEEE International Conference on Robotics and Automation (ICRA)*, pp. 2500–2505. Available at: https://doi.org/10.1109/ICRA.2016.7487404.

Bogue, R. (2008) ‘Cutting robots: a review of technologies and applications’, *Industrial Robot: An International Journal*. Edited by J. Franks, 35(5), pp. 390–396. Available at: https://doi.org/10.1108/01439910810893554.

Borrell Méndez, J. *et al.* (2020) ‘Robotic Pick-and-Place Time Optimization: Application to Footwear Production’, *IEEE Access*, 8, pp. 209428–209440. Available at: https://doi.org/10.1109/ACCESS.2020.3037145.

Casper, R. and Sundin, E. (2021) ‘Electrification in the automotive industry: effects in remanufacturing’, *Journal of Remanufacturing*, 11(2), pp. 121–136. Available at: https://doi.org/10.1007/s13243-020-00094-8.

Cen, L. and Melkote, S.N. (2017) ‘Effect of Robot Dynamics on the Machining Forces in Robotic Milling’, *Procedia Manufacturing*, 10, pp. 486–496. Available at: https://doi.org/10.1016/j.promfg.2017.07.034.

Chen, W.H., Wegener, K. and Dietrich, F. (2014) ‘A robot assistant for unscrewing in hybrid human-robot disassembly’, in *2014 IEEE International Conference on Robotics and Biomimetics (ROBIO 2014)*. *2014 IEEE International Conference on Robotics and Biomimetics (ROBIO 2014)*, pp. 536–541. Available at: https://doi.org/10.1109/ROBIO.2014.7090386.

Chen, Y. and Dong, F. (2013) ‘Robot machining: recent development and future research issues’, *The International Journal of Advanced Manufacturing Technology*, 66(9), pp. 1489–1497. Available at: https://doi.org/10.1007/s00170-012-4433-4.

Climate Watch and Data-Driven EnviroLab. (n.d.). Net Zero Tracker. Available at: https://zerotracker.net/ [Accessed 11 Dec. 2024].

Cordes, M., Hintze, W. and Altintas, Y. (2019) ‘Chatter stability in robotic milling’, *Robotics and Computer-Integrated Manufacturing*, 55, pp. 11–18. Available at: https://doi.org/10.1016/j.rcim.2018.07.004.

Cuellar, C. *et al.* (2012) ‘Measurement method of the complex magnetic permeability of ferrites in high frequency’, in *2012 IEEE International Instrumentation and Measurement Technology Conference Proceedings*. *2012 IEEE International Instrumentation and Measurement Technology Conference Proceedings*, pp. 63–68. Available at: https://doi.org/10.1109/I2MTC.2012.6229697.

Curti, M., Paulides, J.J.H. and Lomonova, E.A. (2015) ‘An overview of analytical methods for magnetic field computation’, in *2015 Tenth International Conference on Ecological Vehicles and Renewable Energies (EVER)*. *2015 Tenth International Conference on Ecological Vehicles and Renewable Energies (EVER)*, pp. 1–7. Available at: https://doi.org/10.1109/EVER.2015.7112938.

Denkena, B. and Lepper, T. (2015) ‘Enabling an Industrial Robot for Metal Cutting Operations’, *Procedia CIRP*, 35, pp. 79–84. Available at: https://doi.org/10.1016/j.procir.2015.08.100.

DiFilippo, N.M. and Jouaneh, M.K. (2018) ‘A System Combining Force and Vision Sensing for Automated Screw Removal on Laptops’, *IEEE Transactions on Automation Science and Engineering*, 15(2), pp. 887–895. Available at: https://doi.org/10.1109/TASE.2017.2679720.

DiFilippo, N.M., Jouaneh, M.K. and Jedson, A.D. (2024) ‘Optimizing Automated Detection of Cross-Recessed Screws in Laptops Using a Neural Network’, *Applied Sciences*, 14(14), p. 6301. Available at: https://doi.org/10.3390/app14146301.

Dorrell, D.G. and Kayani, O. (2014) ‘Measurement and Calculation of Unbalanced Magnetic Pull in Wound Rotor Induction Machine’, *IEEE Transactions on Magnetics*, 50(11), pp. 1–4. Available at: https://doi.org/10.1109/TMAG.2014.2326414.

Engel-Herbert, R. and Hesjedal, T. (2005) ‘Calculation of the magnetic stray field of a uniaxial magnetic domain’, *Journal of Applied Physics*, 97(7), p. 074504.

Engineering ToolBox (n.d.) Friction coefficients. Available at: https://www.engineeringtoolbox.com/friction-coefficients-d_778.html (Accessed: 24 November 2024).

Erdmann, J.G. *et al.* (2023) ‘Assessment of the disassemblability of electric bicycle motors for remanufacturing’, *Journal of Remanufacturing*, 13(2), pp. 137–159. Available at: https://doi.org/10.1007/s13243-023-00124-1.

Foo, G., Kara, S. and Pagnucco, M. (2021) ‘Screw detection for disassembly of electronic waste using reasoning and re-training of a deep learning model’, *Procedia CIRP*, 98, pp. 666–671. Available at: https://doi.org/10.1016/j.procir.2021.01.172.

Gaul, L., Kögl, M. and Wagner, M. (2013) *Boundary Element Methods for Engineers and Scientists: An Introductory Course with Advanced Topics*. Springer Science & Business Media.

Goel, R. (1978) ‘Analysis of an Interference-Fit Pin Connection’, *IEEE Transactions on Components, Hybrids, and Manufacturing Technology*, 1(3), pp. 248–251. Available at: https://doi.org/10.1109/TCHMT.1978.1135281.

Golbakhshi, H., Namjoo, M. and Mohammadi, M. (2013) ‘A 3D comprehensive finite element based simulation for best Shrink Fit design process’, *Mechanics & Industry*, 14(1), pp. 23–30. Available at: https://doi.org/10.1051/meca/2013051.

Gomes, N.M. *et al.* (2022) ‘Reinforcement Learning for Collaborative Robots Pick-and-Place Applications: A Case Study’, *Automation*, 3(1), pp. 223–241. Available at: https://doi.org/10.3390/automation3010011.

Gonzalez, A.G. *et al.* (2018) ‘Validation of Efficiency Maps of an Outer Rotor Surface Mounted Permanent Magnet Machine for Evaluation of Recyclability of Magnets’, in *2018 IEEE International Magnetics Conference (INTERMAG). 2018 IEEE International Magnetics Conference (INTERMAG)*, pp. 1–6. Available at: https://doi.org/10.1109/INTMAG.2018.8508142.

Guo, K., Zhang, Y. and Sun, J. (2022) ‘Towards stable milling: Principle and application of active contact robotic milling’, *International Journal of Machine Tools and Manufacture*, 182, p. 103952. Available at: https://doi.org/10.1016/j.ijmachtools.2022.103952.

Handong, Z. *et al.* (2017) ‘Analysis of development status of electric motor remanufacturing in China’, *Modern Manufacturing Engineering*, 437(2), p. 153. Available at: https://doi.org/10.16731/j.cnki.1671-3133.2017.02.031.

Hansjosten, M., Baumgärtner, J. and Fleischer, J. (2024) ‘Generalized Partially Destructive Disassembly Planning for Robotic Disassembly’, in *2024 IEEE International Conference on Robotics and Automation (ICRA)*. *2024 IEEE International Conference on Robotics and Automation (ICRA)*, pp. 1978–1984. Available at: https://doi.org/10.1109/ICRA57147.2024.10610546.

Hansjosten, M. and Fleischer, J. (2023) ‘Towards autonomous adaptive disassembly of permanent-magnet synchronous motors with industrial robots’, *Manufacturing Letters*, 35, pp. 1336–1346. Available at: https://doi.org/10.1016/j.mfglet.2023.08.084.

Hao, D. *et al.* (2020) ‘Experimental study of stability prediction for high-speed robotic milling of aluminum’, *Journal of Vibration and Control*, 26(7–8), pp. 387–398. Available at: https://doi.org/10.1177/1077546319880376.

Hawken, P., Lovins, A.B. and Lovins, L.H. (2013) *Natural Capitalism: The Next Industrial Revolution*. Routledge.

Heim, M. *et al.* (2023) ‘An Approach for the Disassembly of Permanent Magnet Synchronous Rotors to Recover Rare Earth Materials’, *Procedia CIRP*, 116, pp. 71–76. Available at: https://doi.org/10.1016/j.procir.2023.02.013.

Holehouse, R.C. *et al.* (2014) ‘Unbalanced Magnetic Pull in Permanent Magnet Machines’, in *7th IET International Conference on Power Electronics, Machines and Drives (PEMD 2014)*. *7th IET International Conference on Power Electronics, Machines and Drives (PEMD 2014)*, Manchester, UK: Institution of Engineering and Technology, p. 2.1.01-2.1.01. Available at: https://doi.org/10.1049/cp.2014.0277.

Huang, J. *et al.* (2020) ‘A case study in human–robot collaboration in the disassembly of press-fitted components’, *Proceedings of the Institution of Mechanical Engineers, Part B: Journal of Engineering Manufacture*, 234(3), pp. 654–664. Available at: https://doi.org/10.1177/0954405419883060.

Huang, J. *et al.* (2021) ‘Strategies for Dealing with Problems in Robotised Unscrewing Operations’, in S. Ratchev (ed.) *Smart Technologies for Precision Assembly*. Cham: Springer International Publishing, pp. 93–107. Available at: https://doi.org/10.1007/978-3-030-72632-4_7.

Huynh, H.N. *et al.* (2020) ‘Modelling the dynamics of industrial robots for milling operations’, *Robotics and Computer-Integrated Manufacturing*, 61, p. 101852. Available at: https://doi.org/10.1016/j.rcim.2019.101852.

Ihne, T. *et al.* (2024) ‘Recycling Concept for Electric Vehicle Drives in the Context of Rare Earth Recovery’, *2024 1st International Conference on Production Technologies and Systems for E-Mobility (EPTS)*, pp. 1–9. Available at: https://doi.org/10.1109/EPTS61482.2024.10586730.

International Conference on Assembly Automation (1982) *Proceedings of the 3rd International Conference on Assembly Automation, and, 14th IPA Conference, Boeblingen, nr. Stuttgart, W. Germany, 25th-27th May, 1982 / organised jointly by: Institute of Production Automation (IPA)... and IFS (Conferences) Ltd. ....* Kempston: IFS Publications.

Jin, H. *et al.* (2018) ‘Life Cycle Assessment of Neodymium-Iron-Boron Magnet-to-Magnet Recycling for Electric Vehicle Motors’, *Environmental Science & Technology*, 52(6), pp. 3796–3802. Available at: https://doi.org/10.1021/acs.est.7b05442.

Jørgensen, T.B. *et al.* (2019) ‘An Adaptive Robotic System for Doing Pick and Place Operations with Deformable Objects’, *Journal of Intelligent & Robotic Systems*, 94(1), pp. 81–100. Available at: https://doi.org/10.1007/s10846-018-0958-6.

Kerin, M. and Pham, D.T. (2019) ‘A review of emerging industry 4.0 technologies in remanufacturing’, *Journal of Cleaner Production*, 237, p. 117805. Available at: https://doi.org/10.1016/j.jclepro.2019.117805.

Kerin, M. and Pham, D.T. (2020) ‘Smart remanufacturing: a review and research framework’, *Journal of Manufacturing Technology Management*, 31(6), pp. 1205–1235. Available at: https://doi.org/10.1108/JMTM-06-2019-0205.

Kimiabeigi, M. *et al.* (2018) ‘Production and Application of HPMS Recycled Bonded Permanent Magnets for a Traction Motor Application’, *IEEE Transactions on Industrial Electronics*, 65(5), pp. 3795–3804. Available at: https://doi.org/10.1109/TIE.2017.2762625.

Kis, P. *et al.* (2004) ‘Hysteresis measurement in LabView’, *Physica B: Condensed Matter*, 343(1), pp. 357–363. Available at: https://doi.org/10.1016/j.physb.2003.08.069.

Kotthauser, T. and Mauer, G.F. (2009) ‘Vision-based autonomous robot control for pick and place operations’, in *2009 IEEE/ASME International Conference on Advanced Intelligent Mechatronics*. *2009 IEEE/ASME International Conference on Advanced Intelligent Mechatronics*, pp. 1851–1855. Available at: https://doi.org/10.1109/AIM.2009.5229792.

Kovan, V. (2011) ‘Separation frequency analysis of interference fitted hollow shaft–hub connections by finite element method’, *Advances in Engineering Software*, 42(9), pp. 644–648. Available at: https://doi.org/10.1016/j.advengsoft.2011.05.001.

Kovetz, A. (2000) *Electromagnetic Theory*. Oxford University Press. Available at: https://doi.org/10.1093/oso/9780198506041.001.0001.

Kumar, R. *et al.* (2014) ‘Object detection and recognition for a pick and place Robot’, in *Asia-Pacific World Congress on Computer Science and Engineering*. *Asia-Pacific World Congress on Computer Science and Engineering*, pp. 1–7. Available at: https://doi.org/10.1109/APWCCSE.2014.7053853.

Li, R. *et al.* (2020) ‘Unfastening of Hexagonal Headed Screws by a Collaborative Robot’, *IEEE Transactions on Automation Science and Engineering*, pp. 1–14. Available at: https://doi.org/10.1109/TASE.2019.2958712.

Li, Z. *et al.* (2019) ‘Direct reuse strategies of rare earth permanent magnets for PM electrical machines – an overview study’, *The European Physical Journal Applied Physics*. Edited by A. Razek, 86(2), p. 20901. Available at: https://doi.org/10.1051/epjap/2019180289.

Li, Z. *et al.* (2021) ‘Implementation and analysis of remanufacturing large-scale asynchronous motor to permanent magnet motor under circular economy conditions’, *Journal of Cleaner Production*, 294, p. 126233. Available at: https://doi.org/10.1016/j.jclepro.2021.126233.

Li, Z. *et al.* (2022) ‘Recycling and remanufacturing technology analysis of permanent magnet synchronous motor’, *Clean Technologies and Environmental Policy*, 24(6), pp. 1727–1740. Available at: https://doi.org/10.1007/s10098-022-02279-0.

Liu, J. *et al.* (2020) ‘Service Platform for Robotic Disassembly Planning in Remanufacturing’, *Journal of Manufacturing Systems*, 57, pp. 338–356. Available at: https://doi.org/10.1016/j.jmsy.2020.10.005.

Liu, Q. *et al.* (2023) ‘A Two-Stage Screw Detection Framework for Automatic Disassembly Using a Reflection Feature Regression Model’, *Micromachines*, 14(5), p. 946. Available at: https://doi.org/10.3390/mi14050946.

Lobbezoo, A. and Kwon, H.-J. (2023) ‘Simulated and Real Robotic Reach, Grasp, and Pick-and-Place Using Combined Reinforcement Learning and Traditional Controls’, *Robotics*, 12(1), p. 12. Available at: https://doi.org/10.3390/robotics12010012.

Lobbezoo, A., Qian, Y. and Kwon, H.-J. (2021) ‘Reinforcement Learning for Pick and Place Operations in Robotics: A Survey’, *Robotics*, 10(3), p. 105. Available at: https://doi.org/10.3390/robotics10030105.

Lu, H.Y., Zhu, J.G. and Hui, S.Y.R. (2007) ‘Measurement and Modeling of Thermal Effects on Magnetic Hysteresis of Soft Ferrites’, *IEEE Transactions on Magnetics*, 43(11), pp. 3952–3960. Available at: https://doi.org/10.1109/TMAG.2007.904942.

Lu, M. *et al.* (2021) ‘A high-frequency phase feature for the measurement of magnetic permeability using eddy current sensor’, *NDT & E International*, 123, p. 102519. Available at: https://doi.org/10.1016/j.ndteint.2021.102519.

MacArthur, E. (2013) ‘Towards the circular economy’, *Journal of Industrial Ecology*, 2(1), pp. 23–44.

Magnet DC motor. (n.d.) Available at: https://item.taobao.com/item.htm?app=chrome&bxsign=scdy_uTkuWpOwYHjwNrU6pHEt4Enux3uYCzSFl-ysb9MgUTTrEPCPrqR3YziyHVBJnibzUcQvxyeVaz7YEtBVCbsALWG04mpdG3IePQD670RE69KdhMHDVy_KMzFHAvTRqi&cpp=1&id=777791274666&price=400&share_crt_v=1&shareurl=true&short_name=h.Trfi7lPQSEZdpGc&sourceType=item&sp_tk=NWtNdWU3amk3OTQ%3D&spm=a2159r.13376460.0.0&suid=e9c1f3b8-4ab3-47ee-a95e-2a581669649b&tbSocialPopKey=shareItem&tk=5kMue7ji794&un=2253a3d3f924dff3a8fb54add16a2d54&un_site=0&ut_sk=1.ZpjA0jRyt0MDAIUqm6Cey%2B5b_21646297_1739701212730.Copy.ShareGlobalNavigation_1.

Mangold, S. *et al.* (2022) ‘Vision-Based Screw Head Detection for Automated Disassembly for Remanufacturing’, *Procedia CIRP*, 105, pp. 1–6. Available at: https://doi.org/10.1016/j.procir.2022.02.001.

Matsuoka, S. *et al.* (1999) ‘High-speed end milling of an articulated robot and its characteristics’, *Journal of Materials Processing Technology*, 95(1), pp. 83–89. Available at: https://doi.org/10.1016/S0924-0136(99)00315-5.

Mousavi, S. *et al.* (2018) ‘Stability optimization in robotic milling through the control of functional redundancies’, *Robotics and Computer-Integrated Manufacturing*, 50, pp. 181–192. Available at: https://doi.org/10.1016/j.rcim.2017.09.004.

Myint, K.M. and Htun, Z.M.M. (2016) ‘Position Control Method For Pick And Place Robot Arm For Object Sorting System’, 5(06).

Nguyen, V., Johnson, J. and Melkote, S. (2020) ‘Active vibration suppression in robotic milling using optimal control’, *International Journal of Machine Tools and Manufacture*, 152, p. 103541. Available at: https://doi.org/10.1016/j.ijmachtools.2020.103541.

Ni, R. *et al.* (2016) ‘Efficiency Enhancement of General AC Drive System by Remanufacturing Induction Motor With Interior Permanent-Magnet Rotor’, *IEEE Transactions on Industrial Electronics*, 63(2), pp. 808–820. Available at: https://doi.org/10.1109/TIE.2015.2477478.

Nordelöf, A. *et al.* (2019) ‘Life cycle assessment of permanent magnet electric traction motors’, *Transportation Research Part D: Transport and Environment*, 67, pp. 263–274. Available at: https://doi.org/10.1016/j.trd.2018.11.004.

Ocak, C. (2018) ‘DESIGN AND PERFORMANCE COMPARISON OF FOUR-POLE BRUSHLESS DC MOTORS WITH DIFFERENT POLE/SLOT COMBINATIONS’, *Engineering Sciences* [Preprint].

Pachauri, R.K. *et al.* (2014) *Climate Change 2014: Synthesis Report. Contribution of Working Groups I, II and III to the Fifth Assessment Report of the Intergovernmental Panel on Climate Change*, *EPIC3Geneva, Switzerland, IPCC, 151 p., pp. 151, ISBN: 978-92-9169-143-2*. Edited by R.K. Pachauri and L. Meyer. Geneva, Switzerland: IPCC, p. 151. Available at: https://epic.awi.de/id/eprint/37530/ (Accessed: 16 November 2024).

Pellicciari, M. *et al.* (2013) ‘A method for reducing the energy consumption of pick-and-place industrial robots’, *Mechatronics*, 23(3), pp. 326–334. Available at: https://doi.org/10.1016/j.mechatronics.2013.01.013.

Peng, Y. *et al.* (2024) ‘Robotic disassembly of screws for end-of-life product remanufacturing enabled by deep reinforcement learning’, *Journal of Cleaner Production*, 439, p. 140863. Available at: https://doi.org/10.1016/j.jclepro.2024.140863.

Perumaal, S.S. and Jawahar, N. (2013) ‘Automated Trajectory Planner of Industrial Robot for Pick-and-Place Task’, *International Journal of Advanced Robotic Systems*, 10(2), p. 100. Available at: https://doi.org/10.5772/53940.

Qiu, J. (2016) ‘Analytical Solution for Interference Fit for Multi-Layer Thick-Walled Cylinders and the Application in Crankshaft Bearing Design’, in. Available at: https://www.semanticscholar.org/paper/Analytical-Solution-for-Interference-Fit-for-and-in-Qiu/992b10332ffe686b522234db5cd814c2bf2cb0e4 (Accessed: 4 November 2024).

Ramakrishnan, K. *et al.* (2017) ‘Comparative analysis of various methods for modelling surface permanent magnet machines’, *IET Electric Power Applications*, 11(4), pp. 540–547.

Rastegarpanah, A. *et al.* (2021) ‘Nut Unfastening by Robotic Surface Exploration’, *Robotics*, 10(3), p. 107. Available at: https://doi.org/10.3390/robotics10030107.

Robotiq. (n.d.) 3-Finger Adaptive Robot Gripper. Available at: https://robotiq.com/products/3-finger-adaptive-robot-gripper (Accessed: 6 December 2024).

Salah, A.A., Dorrell, D.G. and Guo, Y. (2019) ‘A Review of the Monitoring and Damping Unbalanced Magnetic Pull in Induction Machines Due to Rotor Eccentricity’, *IEEE Transactions on Industry Applications*, 55(3), pp. 2569–2580. Available at: https://doi.org/10.1109/TIA.2019.2892359.

Shubbar, A. *et al.* (2021) ‘Towards Net Zero Carbon Economy: Improving the Sustainability of Existing Industrial Infrastructures in the UK’, *Energies*, 14(18), p. 5896. Available at: https://doi.org/10.3390/en14185896.

Staubli. (2018) VAL 3 reference manual version 8. Staubli Robotics.

Sun, M.Y. *et al.* (2010) ‘Three-dimensional finite element method simulation and optimization of shrink fitting process for a large marine crankshaft’, *Materials & Design*, 31(9), pp. 4155–4164. Available at: https://doi.org/10.1016/j.matdes.2010.04.027.

Surati, S. *et al.* (2021) ‘Pick and Place Robotic Arm: A Review Paper’, 08(02).

Tiwari, D. *et al.* (2021) ‘A Review of Circular Economy Research for Electric Motors and the Role of Industry 4.0 Technologies’, *Sustainability*, 13(17), p. 9668. Available at: https://doi.org/10.3390/su13179668.

Vosniakos, G.-C. and Matsas, E. (2010) ‘Improving feasibility of robotic milling through robot placement optimisation’, *Robotics and Computer-Integrated Manufacturing*, 26(5), pp. 517–525. Available at: https://doi.org/10.1016/j.rcim.2010.04.001.

Wang, W. *et al.* (2023) ‘A state-of-the-art review on robotic milling of complex parts with high efficiency and precision’, *Robotics and Computer-Integrated Manufacturing*, 79, p. 102436. Available at: https://doi.org/10.1016/j.rcim.2022.102436.

Wang, Xingyuan *et al.* (2017) ‘A new analytical method for press-fit curve prediction of interference fitting parts’, *Journal of Materials Processing Technology*, 250, pp. 16–24. Available at: https://doi.org/10.1016/j.jmatprotec.2017.06.022.

Wuebbles, D.J., Fahey, D.W. and Hibbard, K.A. (no date) ‘Climate Science Special Report: Fourth National Climate Assessment, Volume I’. Available at: https://repository.library.noaa.gov/view/noaa/19486 (Accessed: 16 November 2024).

Xu, S., Pham, D.T. and Su, S. (2024) ‘Robotized unplugging of a cylindrical peg press-fitted into a cylindrical hole’, *Royal Society Open Science*, 11(1), p. 230872. Available at: https://doi.org/10.1098/rsos.230872.

Yang, Z. *et al.* (2020) ‘Analysis and optimisation of a bearingless induction motor’s suspension force and unbalanced magnetic pulling force mathematical model’, *IET Electric*

Power Applications, 14(7), pp. 1247–1255. Available at: https://doi.org/10.1049/iet-epa.2019.0817.

Abdi, S., Abdi, E., McMahon, R., 2015. A Study of Unbalanced Magnetic Pull in Brushless Doubly Fed Machines. IEEE Transactions on Energy Conversion 30, 1218–1227. https://doi.org/10.1109/TEC.2015.2394912

Al Assadi, A., Holtz, D., Nägele, F., Nitsche, C., Kraus, W., Huber, M.F., 2022. Machine learning based screw drive state detection for unfastening screw connections. Journal of Manufacturing Systems 65, 19–32. https://doi.org/10.1016/j.jmsy.2022.07.013

Andhare, P., Rawat, S., 2016. Pick and place industrial robot controller with computer vision, in: 2016 International Conference on Computing Communication Control and Automation (ICCUBEA). Presented at the 2016 International Conference on Computing Communication Control and automation (ICCUBEA), pp. 1–4. https://doi.org/10.1109/ICCUBEA.2016.7860048

Bai, Z., Wang, J., Ning, K., Hou, D., 2018. Contact Pressure Algorithm of Multi-Layer Interference Fit Considering Centrifugal Force and Temperature Gradient. Applied Sciences 8, 726. https://doi.org/10.3390/app8050726

Bdiwi, M., Rashid, A., Putz, M., 2016. Autonomous disassembly of electric vehicle motors based on robot cognition, in: 2016 IEEE International Conference on Robotics and Automation (ICRA). Presented at the 2016 IEEE International Conference on Robotics and Automation (ICRA), pp. 2500–2505. https://doi.org/10.1109/ICRA.2016.7487404

Bogue, R., 2008. Cutting robots: a review of technologies and applications. Industrial Robot: An International Journal 35, 390–396. https://doi.org/10.1108/01439910810893554

Borrell Méndez, J., Perez-Vidal, C., Segura Heras, J.V., Pérez-Hernández, J.J., 2020. Robotic Pick-and-Place Time Optimization: Application to Footwear Production. IEEE Access 8, 209428–209440. https://doi.org/10.1109/ACCESS.2020.3037145

Casper, R., Sundin, E., 2021. Electrification in the automotive industry: effects in remanufacturing. Jnl Remanufactur 11, 121–136. https://doi.org/10.1007/s13243-020-00094-8

Cen, L., Melkote, S.N., 2017. Effect of Robot Dynamics on the Machining Forces in Robotic Milling. Procedia Manufacturing, 45th SME North American Manufacturing Research Conference, NAMRC 45, LA, USA 10, 486–496. https://doi.org/10.1016/j.promfg.2017.07.034

Chen, W.H., Wegener, K., Dietrich, F., 2014. A robot assistant for unscrewing in hybrid human-robot disassembly, in: 2014 IEEE International Conference on Robotics and Biomimetics (ROBIO 2014). Presented at the 2014 IEEE International Conference on Robotics and Biomimetics (ROBIO 2014), pp. 536–541. https://doi.org/10.1109/ROBIO.2014.7090386

Chen, Y., Dong, F., 2013. Robot machining: recent development and future research issues. Int J Adv Manuf Technol 66, 1489–1497. https://doi.org/10.1007/s00170-012-4433-4

Cordes, M., Hintze, W., Altintas, Y., 2019. Chatter stability in robotic milling. Robotics and Computer-Integrated Manufacturing 55, 11–18. https://doi.org/10.1016/j.rcim.2018.07.004

Cuellar, C., Tan, W., Margueron, X., Benabou, A., Idir, N., 2012. Measurement method of the complex magnetic permeability of ferrites in high frequency, in: 2012 IEEE International Instrumentation and Measurement Technology Conference Proceedings. Presented at the 2012 IEEE International Instrumentation and Measurement Technology Conference Proceedings, pp. 63–68. https://doi.org/10.1109/I2MTC.2012.6229697

Curti, M., Paulides, J.J.H., Lomonova, E.A., 2015. An overview of analytical methods for magnetic field computation, in: 2015 Tenth International Conference on Ecological Vehicles and Renewable Energies (EVER). Presented at the 2015 Tenth International Conference on Ecological Vehicles and Renewable Energies (EVER), pp. 1–7. https://doi.org/10.1109/EVER.2015.7112938

Denkena, B., Lepper, T., 2015. Enabling an Industrial Robot for Metal Cutting Operations. Procedia CIRP, MIC2015 – 15th Machining Innovations Conference for Aerospace Industry 35, 79–84. https://doi.org/10.1016/j.procir.2015.08.100

DiFilippo, N.M., Jouaneh, M.K., 2018. A System Combining Force and Vision Sensing for Automated Screw Removal on Laptops. IEEE Transactions on Automation Science and Engineering 15, 887–895. https://doi.org/10.1109/TASE.2017.2679720

DiFilippo, N.M., Jouaneh, M.K., Jedson, A.D., 2024. Optimizing Automated Detection of Cross-Recessed Screws in Laptops Using a Neural Network. Applied Sciences 14, 6301. https://doi.org/10.3390/app14146301

Climate Watch and Data-Driven EnviroLab. (n.d.). Net Zero Tracker. Available at: https://zerotracker.net/ [Accessed 11 Dec. 2024].

Dorrell, D.G., Kayani, O., 2014. Measurement and Calculation of Unbalanced Magnetic Pull in Wound Rotor Induction Machine. IEEE Trans. Magn. 50, 1–4. https://doi.org/10.1109/TMAG.2014.2326414

Engel-Herbert, R., Hesjedal, T., 2005. Calculation of the magnetic stray field of a uniaxial magnetic domain. Journal of Applied Physics 97, 074504.

Engineering ToolBox (n.d.) Friction coefficients. Available at: https://www.engineeringtoolbox.com/friction-coefficients-d_778.html (Accessed: 24 November 2024).

Erdmann, J.G., Koller, J., Brimaire, J., Döpper, F., 2023. Assessment of the disassemblability of electric bicycle motors for remanufacturing. Jnl Remanufactur 13, 137–159. https://doi.org/10.1007/s13243-023-00124-1

Foo, G., Kara, S., Pagnucco, M., 2021. Screw detection for disassembly of electronic waste using reasoning and re-training of a deep learning model. Procedia CIRP, The 28th CIRP Conference on Life Cycle Engineering, March 10 – 12, 2021, Jaipur, India 98, 666–671. https://doi.org/10.1016/j.procir.2021.01.172

Gaul, L., Kögl, M., Wagner, M., 2013. Boundary Element Methods for Engineers and Scientists: An Introductory Course with Advanced Topics. Springer Science & Business Media.

Goel, R., 1978. Analysis of an Interference-Fit Pin Connection. IEEE Transactions on Components, Hybrids, and Manufacturing Technology 1, 248–251. https://doi.org/10.1109/TCHMT.1978.1135281

Golbakhshi, H., Namjoo, M., Mohammadi, M., 2013. A 3D comprehensive finite element based simulation for best Shrink Fit design process. Mechanics & Industry 14, 23–30. https://doi.org/10.1051/meca/2013051

Gomes, N.M., Martins, F.N., Lima, J., Wörtche, H., 2022. Reinforcement Learning for Collaborative Robots Pick-and-Place Applications: A Case Study. Automation 3, 223–241. https://doi.org/10.3390/automation3010011

Gonzalez, A.G., Jha, A.K., Li, Z., Upadhayay, P., Rasmussen, P., 2018. Validation of Efficiency Maps of an Outer Rotor Surface Mounted Permanent Magnet Machine for Evaluation of Recyclability of Magnets, in: 2018 IEEE International Magnetics Conference (INTERMAG). Presented at the 2018 IEEE International Magnetics Conference (INTERMAG), pp. 1–6. https://doi.org/10.1109/INTMAG.2018.8508142

Guo, K., Zhang, Y., Sun, J., 2022. Towards stable milling: Principle and application of active contact robotic milling. International Journal of Machine Tools and Manufacture 182, 103952. https://doi.org/10.1016/j.ijmachtools.2022.103952

Handong, Z., Peijing, S., Enzhong, L., Binshi, X., 2017. Analysis of development status of electric motor remanufacturing in China. Modern Manufacturing Engineering 437, 153. https://doi.org/10.16731/j.cnki.1671-3133.2017.02.031

Hansjosten, M., Baumgärtner, J., Fleischer, J., 2024. Generalized Partially Destructive Disassembly Planning for Robotic Disassembly, in: 2024 IEEE International Conference on Robotics and Automation (ICRA). Presented at the 2024 IEEE International Conference on Robotics and Automation (ICRA), pp. 1978–1984. https://doi.org/10.1109/ICRA57147.2024.10610546

Hansjosten, M., Fleischer, J., 2023. Towards autonomous adaptive disassembly of permanent-magnet synchronous motors with industrial robots. Manufacturing Letters, 51st SME North American Manufacturing Research Conference (NAMRC 51) 35, 1336–1346. https://doi.org/10.1016/j.mfglet.2023.08.084

Hao, D., Wang, W., Liu, Z., Yun, C., 2020. Experimental study of stability prediction for high-speed robotic milling of aluminum. Journal of Vibration and Control 26, 387–398. https://doi.org/10.1177/1077546319880376

Hawken, P., Lovins, A.B., Lovins, L.H., 2013. Natural Capitalism: The Next Industrial Revolution. Routledge.

Heim, M., Wirth, F., Boschert, L., Fleischer, J., 2023. An Approach for the Disassembly of Permanent Magnet Synchronous Rotors to Recover Rare Earth Materials. Procedia CIRP, 30th CIRP Life Cycle Engineering Conference 116, 71–76. https://doi.org/10.1016/j.procir.2023.02.013

Holehouse, R.C., Atallah, K., Michon, M., Jiabin Wang, 2014. Unbalanced Magnetic Pull in Permanent Magnet Machines, in: 7th IET International Conference on Power Electronics, Machines and Drives (PEMD 2014). Presented at the 7th IET International Conference on Power Electronics, Machines and Drives (PEMD 2014), Institution of Engineering and Technology, Manchester, UK, p. 2.1.01-2.1.01. https://doi.org/10.1049/cp.2014.0277

Huang, J., Pham, D.T., Li, R., Jiang, K., Lyu, D., Ji, C., 2021. Strategies for Dealing with Problems in Robotised Unscrewing Operations, in: Ratchev, S. (Ed.), Smart Technologies for Precision Assembly. Springer International Publishing, Cham, pp. 93–107. https://doi.org/10.1007/978-3-030-72632-4_7

Huang, J., Pham, D.T., Wang, Y., Qu, M., Ji, C., Su, S., Xu, W., Liu, Q., Zhou, Z., 2020. A case study in human–robot collaboration in the disassembly of press-fitted components. Proceedings of the Institution of Mechanical Engineers, Part B: Journal of Engineering Manufacture 234, 654–664. https://doi.org/10.1177/0954405419883060

Ihne, T., Hahn, R., Wieprecht, N., Franke, J., Kühl, A., 2024. Recycling Concept for Electric Vehicle Drives in the Context of Rare Earth Recovery. 2024 1st International Conference on Production Technologies and Systems for E-Mobility (EPTS) 1–9. https://doi.org/10.1109/EPTS61482.2024.10586730

International Conference on Assembly Automation, 1982. Proceedings of the 3rd International Conference on Assembly Automation, and, 14th IPA Conference, Boeblingen, nr. Stuttgart, W. Germany, 25th-27th May, 1982 / organised jointly by: Institute of Production Automation (IPA)... and IFS (Conferences) Ltd. .... IFS Publications, Kempston.

Jin, H., Afiuny, P., Dove, S., Furlan, G., Zakotnik, M., Yih, Y., Sutherland, J.W., 2018. Life Cycle Assessment of Neodymium-Iron-Boron Magnet-to-Magnet Recycling for Electric Vehicle Motors. Environ. Sci. Technol. 52, 3796–3802. https://doi.org/10.1021/acs.est.7b05442

Jørgensen, T.B., Jensen, S.H.N., Aanæs, H., Hansen, N.W., Krüger, N., 2019. An Adaptive Robotic System for Doing Pick and Place Operations with Deformable Objects. J Intell Robot Syst 94, 81–100. https://doi.org/10.1007/s10846-018-0958-6

Kerin, M., Pham, D.T., 2020. Smart remanufacturing: a review and research framework. Journal of Manufacturing Technology Management 31, 1205–1235. https://doi.org/10.1108/JMTM-06-2019-0205

Kerin, M., Pham, D.T., 2019. A review of emerging industry 4.0 technologies in remanufacturing. Journal of Cleaner Production 237, 117805. https://doi.org/10.1016/j.jclepro.2019.117805

Kimiabeigi, M., Sheridan, R.S., Widmer, J.D., Walton, A., Farr, M., Scholes, B., Harris, I.R., 2018. Production and Application of HPMS Recycled Bonded Permanent Magnets for a Traction Motor Application. IEEE Trans. Ind. Electron. 65, 3795–3804. https://doi.org/10.1109/TIE.2017.2762625

Kiraly Tool. (2017) Hole and shaft tolerance chart. Available at: https://kiralytool.com/wp-content/uploads/2017/05/hole-shaft-tolerance-chart.pdf (Accessed: 6 December 2024).

Kis, P., Kuczmann, M., Füzi, J., Iványi, A., 2004. Hysteresis measurement in LabView. Physica B: Condensed Matter, Proceedings of the Fourth Intional Conference on Hysteresis and Micromagnetic Modeling 343, 357–363. https://doi.org/10.1016/j.physb.2003.08.069

Kotthauser, T., Mauer, G.F., 2009. Vision-based autonomous robot control for pick and place operations, in: 2009 IEEE/ASME International Conference on Advanced Intelligent Mechatronics. Presented at the 2009 IEEE/ASME International Conference on Advanced Intelligent Mechatronics, pp. 1851–1855. https://doi.org/10.1109/AIM.2009.5229792

Kovan, V., 2011. Separation frequency analysis of interference fitted hollow shaft–hub connections by finite element method. Advances in Engineering Software 42, 644–648. https://doi.org/10.1016/j.advengsoft.2011.05.001

Kovetz, A., 2000. Electromagnetic Theory. Oxford University Press. https://doi.org/10.1093/oso/9780198506041.001.0001

Kumar, R., Lal, S., Kumar, S., Chand, P., 2014. Object detection and recognition for a pick and place Robot, in: Asia-Pacific World Congress on Computer Science and Engineering. Presented at the Asia-Pacific World Congress on Computer Science and Engineering, pp. 1–7. https://doi.org/10.1109/APWCCSE.2014.7053853

Li, R., Ji, C., Liu, Q., Zhou, Z., Pham, D.T., Huang, J., Tan, Y., Qu, M., Wang, Y., Kerin, M., Jiang, K., Su, S., 2020. Unfastening of Hexagonal Headed Screws by a Collaborative Robot. IEEE Trans. Automat. Sci. Eng. 1–14. https://doi.org/10.1109/TASE.2019.2958712

Li, Z., Che, S., Wang, P., Du, S., Zhao, Y., Sun, H., Li, Y., 2021. Implementation and analysis of remanufacturing large-scale asynchronous motor to permanent magnet motor under circular economy conditions. Journal of Cleaner Production 294, 126233. https://doi.org/10.1016/j.jclepro.2021.126233

Li, Z., Kedous-Lebouc, A., Dubus, J.-M., Garbuio, L., Personnaz, S., 2019. Direct reuse strategies of rare earth permanent magnets for PM electrical machines – an overview study. Eur. Phys. J. Appl. Phys. 86, 20901. https://doi.org/10.1051/epjap/2019180289

Li, Z., Wang, P., Che, S., Du, S., Li, Y., Sun, H., 2022. Recycling and remanufacturing technology analysis of permanent magnet synchronous motor. Clean Techn Environ Policy 24, 1727–1740. https://doi.org/10.1007/s10098-022-02279-0

Liu, J., Zhou, Z., Pham, D.T., Xu, W., Cui, J., Yang, C., 2020. Service Platform for Robotic Disassembly Planning in Remanufacturing. Journal of Manufacturing Systems 57, 338–356. https://doi.org/10.1016/j.jmsy.2020.10.005

Liu, Q., Deng, W., Pham, D.T., Hu, J., Wang, Y., Zhou, Z., 2023. A Two-Stage Screw Detection Framework for Automatic Disassembly Using a Reflection Feature Regression Model. Micromachines 14, 946. https://doi.org/10.3390/mi14050946

Lobbezoo, A., Kwon, H.-J., 2023. Simulated and Real Robotic Reach, Grasp, and Pick-and-Place Using Combined Reinforcement Learning and Traditional Controls. Robotics 12, 12. https://doi.org/10.3390/robotics12010012

Lobbezoo, A., Qian, Y., Kwon, H.-J., 2021. Reinforcement Learning for Pick and Place Operations in Robotics: A Survey. Robotics 10, 105. https://doi.org/10.3390/robotics10030105

Lu, H.Y., Zhu, J.G., Hui, S.Y.R., 2007. Measurement and Modeling of Thermal Effects on Magnetic Hysteresis of Soft Ferrites. IEEE Transactions on Magnetics 43, 3952–3960. https://doi.org/10.1109/TMAG.2007.904942

Lu, M., Meng, X., Huang, R., Chen, L., Peyton, A., Yin, W., 2021. A high-frequency phase feature for the measurement of magnetic permeability using eddy current sensor. NDT & E International 123, 102519. https://doi.org/10.1016/j.ndteint.2021.102519

MacArthur, E., 2013. Towards the circular economy. Journal of Industrial Ecology 2, 23–44.

Mangold, S., Steiner, C., Friedmann, M., Fleischer, J., 2022. Vision-Based Screw Head Detection for Automated Disassembly for Remanufacturing. Procedia CIRP, The 29th CIRP

Conference on Life Cycle Engineering, April 4 – 6, 2022, Leuven, Belgium. 105, 1–6. https://doi.org/10.1016/j.procir.2022.02.001

Matsuoka, S., Shimizu, K., Yamazaki, N., Oki, Y., 1999. High-speed end milling of an articulated robot and its characteristics. Journal of Materials Processing Technology 95, 83–89. https://doi.org/10.1016/S0924-0136(99)00315-5

Myint, K.M., Htun, Z.M.M., 2016. Position Control Method For Pick And Place Robot Arm For Object Sorting System 5.

Nguyen, V., Johnson, J., Melkote, S., 2020. Active vibration suppression in robotic milling using optimal control. International Journal of Machine Tools and Manufacture 152, 103541. https://doi.org/10.1016/j.ijmachtools.2020.103541

Ni, R., Xu, D., Wang, G., Gui, X., Zhang, G., Zhan, H., Li, C., 2016. Efficiency Enhancement of General AC Drive System by Remanufacturing Induction Motor With Interior Permanent-Magnet Rotor. IEEE Transactions on Industrial Electronics 63, 808–820. https://doi.org/10.1109/TIE.2015.2477478

Nordelöf, A., Grunditz, E., Lundmark, S., Tillman, A.-M., Alatalo, M., Thiringer, T., 2019. Life cycle assessment of permanent magnet electric traction motors. Transportation Research Part D: Transport and Environment 67, 263–274. https://doi.org/10.1016/j.trd.2018.11.004

Ocak, C., 2018. DESIGN AND PERFORMANCE COMPARISON OF FOUR-POLE BRUSHLESS DC MOTORS WITH DIFFERENT POLE/SLOT COMBINATIONS. Engineering Sciences.

Pachauri, R.K., Allen, M.R., Barros, V.R., Broome, J., Cramer, W., Christ, R., Church, J.A., Clarke, L., Dahe, Q., Dasgupta, P., Dubash, N.K., Edenhofer, O., Elgizouli, I., Field, C.B., Forster, P., Friedlingstein, P., Fuglestvedt, J., Gomez-Echeverri, L., Hallegatte, S., Hegerl, G., Howden, M., Jiang, K., Jimenez Cisneroz, B., Kattsov, V., Lee, H., Mach, K.J., Marotzke, J., Mastrandrea, M.D., Meyer, L., Minx, J., Mulugetta, Y., O'Brien, K., Oppenheimer, M., Pereira, J.J., Pichs-Madruga, R., Plattner, G.-K., Pörtner, H.-O., Power, S.B., Preston, B., Ravindranath, N.H., Reisinger, A., Riahi, K., Rusticucci, M., Scholes, R., Seyboth, K., Sokona, Y., Stavins, R., Stocker, T.F., Tschakert, P., van Vuuren, D., van Ypserle, J.-P., 2014. Climate Change 2014: Synthesis Report. Contribution of Working Groups I, II and III to the Fifth Assessment Report of the Intergovernmental Panel on Climate Change, EPIC3Geneva, Switzerland, IPCC, 151 p., pp. 151, ISBN: 978-92-9169-143-2. IPCC, Geneva, Switzerland.

Pellicciari, M., Berselli, G., Leali, F., Vergnano, A., 2013. A method for reducing the energy consumption of pick-and-place industrial robots. Mechatronics 23, 326–334. https://doi.org/10.1016/j.mechatronics.2013.01.013

Peng, Y., Li, W., Liang, Y., Pham, D.T., 2024. Robotic disassembly of screws for end-of-life product remanufacturing enabled by deep reinforcement learning. Journal of Cleaner Production 439, 140863. https://doi.org/10.1016/j.jclepro.2024.140863

Perumaal, S.S., Jawahar, N., 2013. Automated Trajectory Planner of Industrial Robot for Pick-and-Place Task. International Journal of Advanced Robotic Systems 10, 100. https://doi.org/10.5772/53940

Qiu, J., 2016. Analytical Solution for Interference Fit for Multi-Layer Thick-Walled Cylinders and the Application in Crankshaft Bearing Design.

Ramakrishnan, K., Curti, M., Zarko, D., Mastinu, G., Paulides, J.J., Lomonova, E.A., 2017. Comparative analysis of various methods for modelling surface permanent magnet machines. IET Electric Power Applications 11, 540–547.

Rastegarpanah, A., Ner, R., Stolkin, R., Marturi, N., 2021. Nut Unfastening by Robotic Surface Exploration. Robotics 10, 107. https://doi.org/10.3390/robotics10030107

Robotiq. (n.d.) 3-Finger Adaptive Robot Gripper. Available at: https://robotiq.com/products/3-finger-adaptive-robot-gripper (Accessed: 6 December 2024).

Salah, A.A., Dorrell, D.G., Guo, Y., 2019. A Review of the Monitoring and Damping Unbalanced Magnetic Pull in Induction Machines Due to Rotor Eccentricity. IEEE Transactions on Industry Applications 55, 2569–2580. https://doi.org/10.1109/TIA.2019.2892359

Shubbar, A., Nasr, M., Falah, M., Al-Khafaji, Z., 2021. Towards Net Zero Carbon Economy: Improving the Sustainability of Existing Industrial Infrastructures in the UK. Energies 14, 5896. https://doi.org/10.3390/en14185896

Staubli. (2018) VAL 3 reference manual version 8. Staubli Robotics.

Sun, M.Y., Lu, S.P., Li, D.Z., Li, Y.Y., Lang, X.G., Wang, S.Q., 2010. Three-dimensional finite element method simulation and optimization of shrink fitting process for a large marine crankshaft. Materials & Design 31, 4155–4164. https://doi.org/10.1016/j.matdes.2010.04.027

Surati, S., Hedaoo, S., Rotti, T., Ahuja, V., Patel, N., 2021. Pick and Place Robotic Arm: A Review Paper 08.

Tiwari, D., Miscandlon, J., Tiwari, A., Jewell, G.W., 2021. A Review of Circular Economy Research for Electric Motors and the Role of Industry 4.0 Technologies. Sustainability 13, 9668. https://doi.org/10.3390/su13179668

Vosniakos, G.-C., Matsas, E., 2010. Improving feasibility of robotic milling through robot placement optimisation. Robotics and Computer-Integrated Manufacturing 26, 517–525. https://doi.org/10.1016/j.rcim.2010.04.001

Wang, W., Guo, Q., Yang, Z., Jiang, Y., Xu, J., 2023. A state-of-the-art review on robotic milling of complex parts with high efficiency and precision. Robotics and Computer-Integrated Manufacturing 79, 102436. https://doi.org/10.1016/j.rcim.2022.102436

Wang, Xingyuan, Lou, Z., Wang, Xiaodong, Xu, C., 2017. A new analytical method for press-fit curve prediction of interference fitting parts. Journal of Materials Processing Technology 250, 16–24. https://doi.org/10.1016/j.jmatprotec.2017.06.022

Wuebbles, D.J., Fahey, D.W., Hibbard, K.A., n.d. Climate Science Special Report: Fourth National Climate Assessment, Volume I.

Xu, S., Pham, D.T., Su, S., 2024. Robotized unplugging of a cylindrical peg press-fitted into a cylindrical hole. Royal Society Open Science 11, 230872. https://doi.org/10.1098/rsos.230872

Yang, Z., Ding, Q., Sun, X., Zhao, Q., Luo, J., 2020. Analysis and optimisation of a bearingless induction motor’s suspension force and unbalanced magnetic pulling force mathematical model. IET Electric Power Applications 14, 1247–1255. https://doi.org/10.1049/iet-epa.2019.0817

YHDFA. (n.d.) WGN21 product details. Available at: https://www.yhdfa.com/products/WGN21?productModel=WGN21-63-50-Y-2&searchContent=WGN21-63-50-Y-2 (Accessed: 6 December 2024).

YHDFA. (n.d.) WGN21 product details. Available at: https://www.yhdfa.com/products/WGN21?productModel=WGN21-63-50-Y-2&searchContent=WGN21-63-50-Y-2 (Accessed: 6 December 2024).

YHDFA. (n.d.) WGY02 product details. Available at: https://www.yhdfa.com/products/WGY02?productModel=WGY02-63-16-2&searchContent=WGY02-63-16-2 (Accessed: 6 December 2024).

YHDFA. (n.d.) WGU02 product details. Available at: https://www.yhdfa.com/products/WGU02?productModel=WGU02-40-75-2&searchContent=WGU02-40-75-2 (Accessed: 6 December 2024).

Zaeh, M.F. and Roesch, O. (2014) ‘Improvement of the machining accuracy of milling robots’, *Production Engineering*, 8(6), pp. 737–744. Available at: https://doi.org/10.1007/s11740-014-0558-7.

Zhang, Y. *et al.* (2019) ‘Peg–hole disassembly using active compliance’, *Royal Society Open Science*, 6(8), p. 190476. Available at: https://doi.org/10.1098/rsos.190476.

Zhou, Y. *et al.* (2022) ‘Stackelberg model-based human-robot collaboration in removing screws for product remanufacturing’, *Robotics and Computer-Integrated Manufacturing*, 77, p. 102370. Available at: https://doi.org/10.1016/j.rcim.2022.102370.

Zhu, Z. *et al.* (2022) ‘High precision and efficiency robotic milling of complex parts: Challenges, approaches and trends’, *Chinese Journal of Aeronautics*, 35(2), pp. 22–46. Available at: https://doi.org/10.1016/j.cja.2020.12.030.

Zhu, Z.Q. and Howe, D. (1993) ‘Instantaneous magnetic field distribution in brushless permanent magnet DC motors. III. Effect of stator slotting’, *IEEE Transactions on Magnetics*, 29(1), pp. 143–151. Available at: https://doi.org/10.1109/20.195559.

Appendices

Appenxdix A. Position relationship in the MMF model

Each magnet has an aligned point on the steel hub on the top view (on the XY plane) (Figure A 1 (a)), and the positions of the steel hubs change when the positions of the magnets change (Figure A 1 (b)). The positions of the 4 magnets are projected to a global Cartesian coordinate system (Eq. A1). The magnets are allowed to move in the x or y direction in the hub, creating a new coordinate system (O') (Eq. A6). The magnet and steel points are assumed to always be aligned because misalignments result in a reduction in magnetic forces in this model. The steel point is calculated on the basis of the new coordinates of the magnets. Therefore, linear equations are created to calculate the coordinates of the steel points $(\mathrm{P'}_{\mathrm{B}})$ by using the coordinates of the magnets $(\mathrm{P'}_{\mathrm{M}})$, the inner radius of the hub $(\mathrm{R}_{\mathrm{bi}})$ and the new origin point (O') (Eqs. A7–A9). The air gaps (g) are calculated by using the coordinates of the steel points $(\mathrm{P'}_{\mathrm{B}})$ and the coordinates of the magnets $(\mathrm{P'}_{\mathrm{M}})$ (Eq. A10).

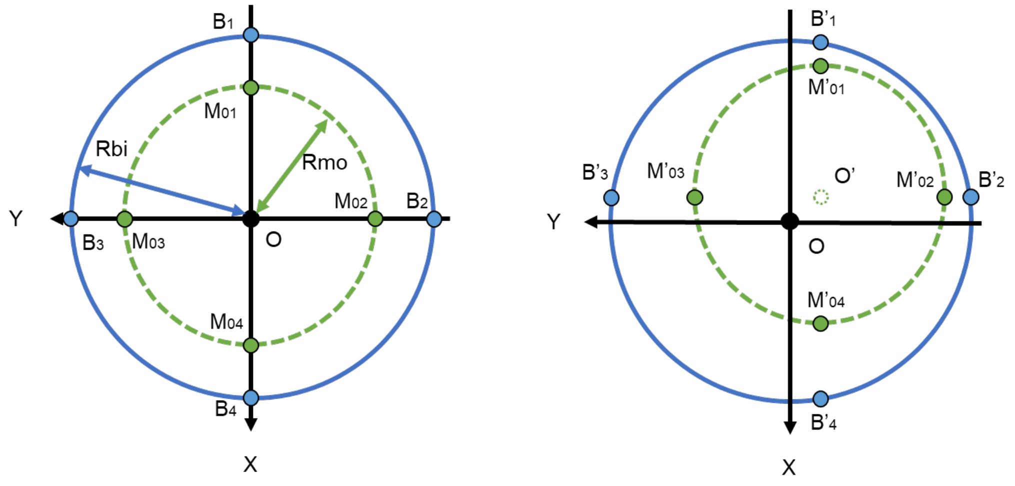

(a) 2D view (concentric position) (b) 2D view (offset position)

Figure A 1 Relative position between points on the magnets and corresponding points on the hub.

$$P'_M(i) = \left(x'_M(i)\sin\theta_{Mp}(i), y'_M(i)\cos\theta_{Mp}(i)\right) \tag{A1}$$

where the coordinate position of each magnet is

$$P'_{M_1} = (x_0 + x - R_{mi}, y_0 + y) \tag{A2}$$

$$P'_{M_4} = (x_0 + x + R_{mi}, y_0 + y) \tag{A3}$$

$$P'_{M_2} = (x_0 + x, y_0 + y - R_{mi}) \tag{A4}$$

$$P'_{M_3} = (x_0 + x, y_0 + y + R_{mi}) \tag{A5}$$

x_M and y_M are the coordinates of the magnets. x_0 and y_0 are 0, representing the origin point of the global coordinate system. x and y are movements of the rotor in the X or Y directions, respectively. R_{mo} is the outer radius of the magnet.

$$O' = \left(x'_0, y'_0\right) = (x_0 + x, y_0 + y) \tag{A6}$$

$$P'_B(i) = \sqrt{(x'_B(i) - x'_0)^2 + (y'_B(i) - y'_0)^2} = R_{bi} \tag{A7}$$

$$y'_B(i) = \frac{x'_B(i) - x'_M(i)}{O'_x} * \left(O'_y - y'_M(i)\right) + y'_M(i) \tag{A8}$$

$$x'_B(i) - x'_0 = \sqrt{{R_{bi}}^2 - (y'_B(i) - y'_0)^2} \tag{A9}$$

$$d_g(i, x, y) = \sqrt{(x'_B(i) - x'_M(i))^2 + (y'_B(i) - y'_M(i))^2} \tag{A10}$$

where O' is the new origin point. x'_M and x'_B are the new X coordinates of the magnet or steel point, respectively, and y'_M and y'_B are the new Y coordinates of the magnet or steel point, respectively.

Appenxdix B. Force analysis of the cutting bit

Owing to the complex geometry of the cutting bit, simulating the entire milling process accurately is challenging. To address this, the material failure force of the cutting bit is determined via the FEM in COMSOL 6.1. In this simulation, the milling bit is assumed to collide with the workpiece without spinning, and loads are applied incrementally until the material reaches its yield strength. This force is used as the reference force (F_0). The loads are applied on the milling contact area, and the tool holding area is where the cutting tool holds the milling bit (Figure B 1 (a)). The area between the tool holding area and the milling contact area is highly deformable when the loads are applied. To capture these deformations accurately, an extremely fine tetrahedral mesh is utilised, with element sizes ranging from 0.0092 mm to 0.92 mm. For the remaining regions, a fine tetrahedral mesh with element sizes between 0.46 mm and 3.68 mm is applied. These mesh configurations are controlled by the software and adapt dynamically to the geometry of the milling bit. To simplify the analysis, the shape of the cutting bit is approximated as a cylinder with a uniform material of 304 stainless steel (Dremel, n.d.).

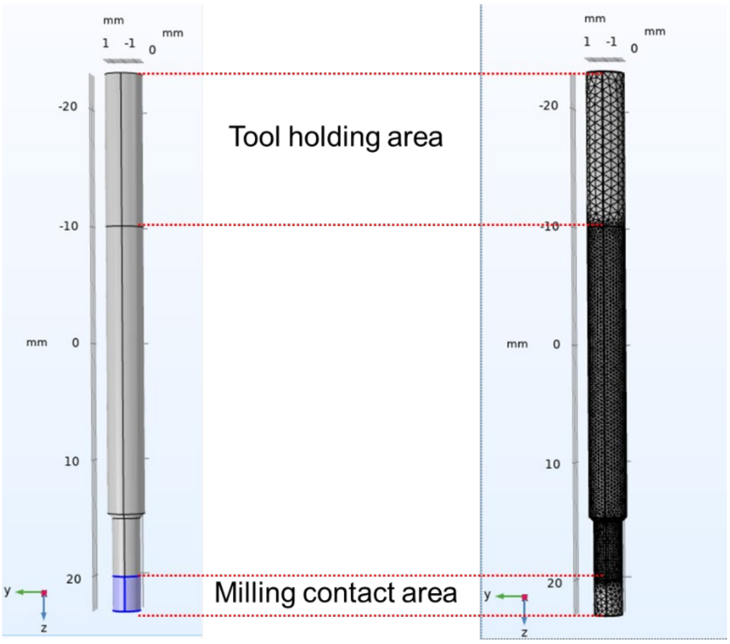

(a) FE model of loads applied on the milling bit

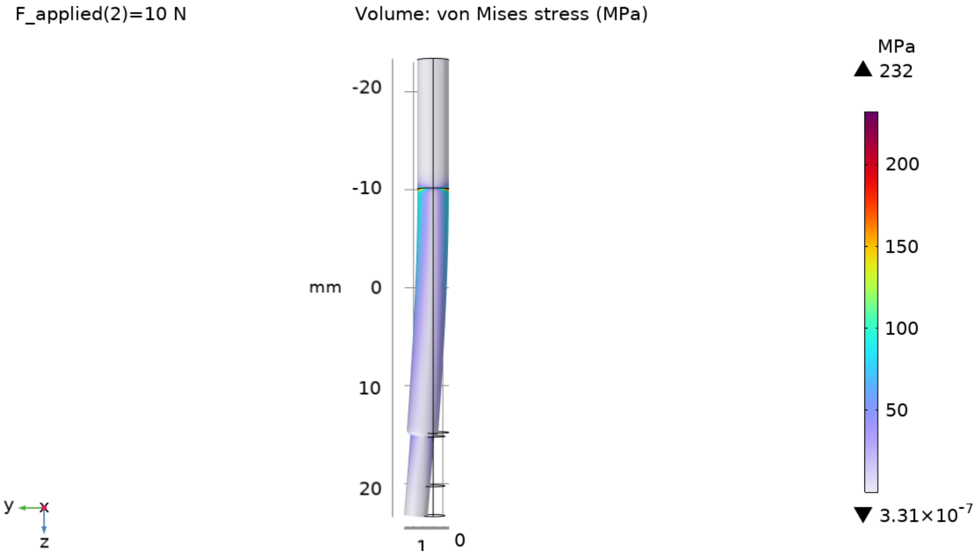

(b) FE result of loading on the milling bit

Figure B 1 FE model and results of force loading on the milling bit.

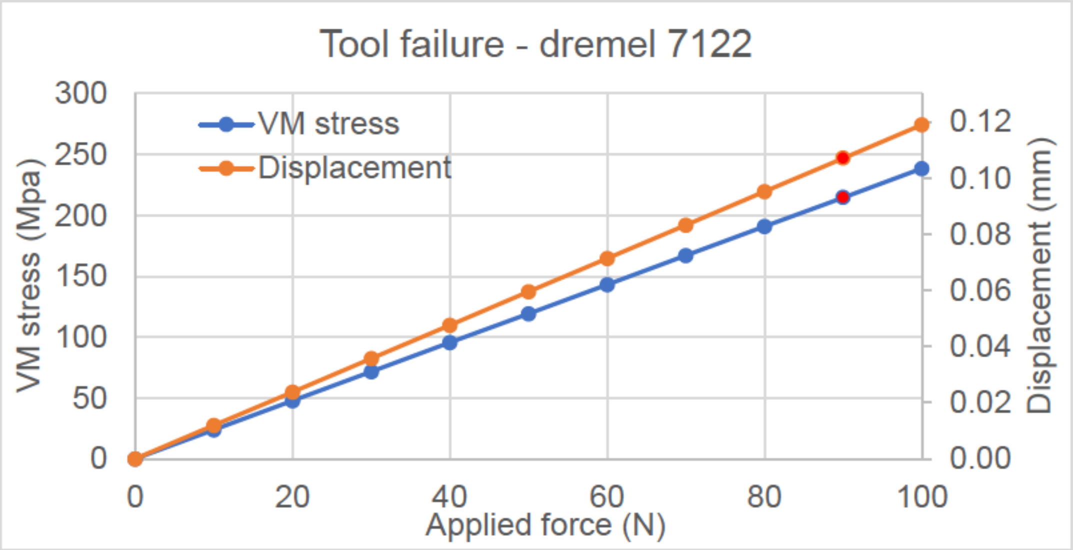

Figure B 2 Results of gradual loading applied to the milling bit.

When the loads are applied on the milling bit, larger deformation occurs between the tool holding area and the milling contact area (Figure B 1 (b)). This deformation generates vibrations in tool spinning during the milling process. The material reaches its yield strength of 204 MPa (Masteel UK Ltd., n.d.) when the load exceeds 90 N (Figure B 2). Given a 30% safety factor for vibrations in the real milling process, the reference force (F_0) is set as 63 N. This reference force is used in the Coil disassembly task (T.4) to validate the control scheme.

Appenxdix C. System design: Mechanical system

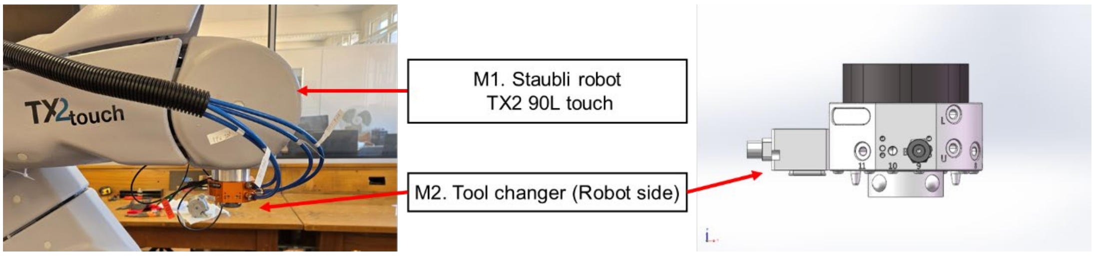

(a) Tool changer (Robot side) installed on the Staubli robot

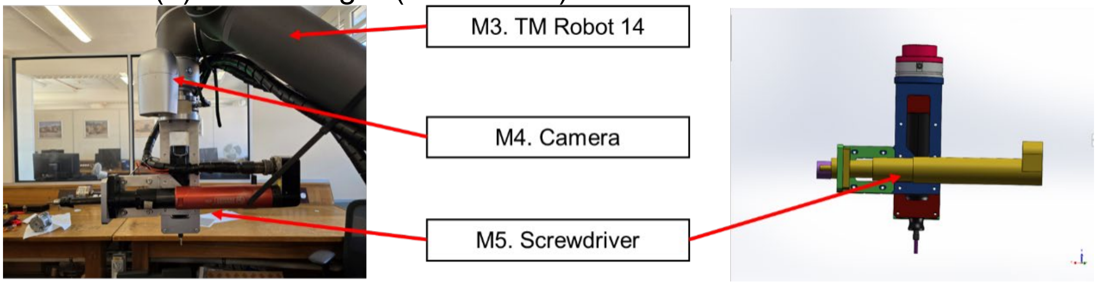

(b) A screwdriver, camera on the TM robot

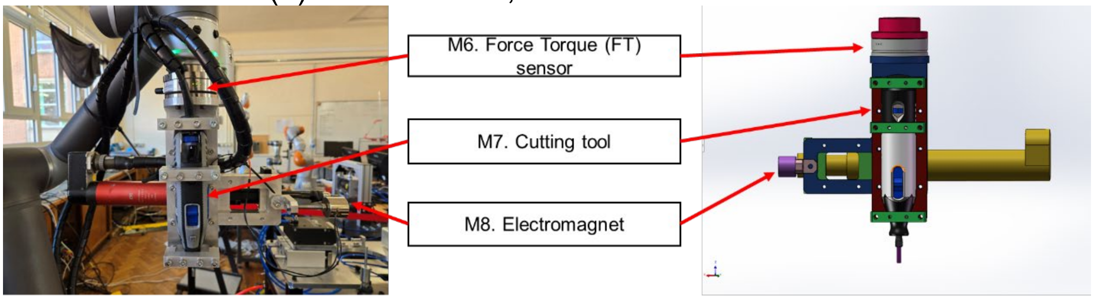

(c) A FT sensor, Cutting tool and electromagnet on TM robot

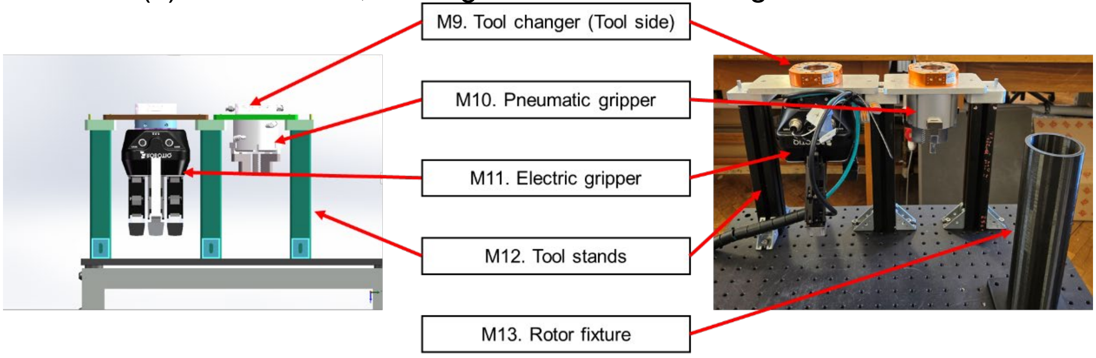

(d) A pneumatic gripper, electric gripper and rotor fixture

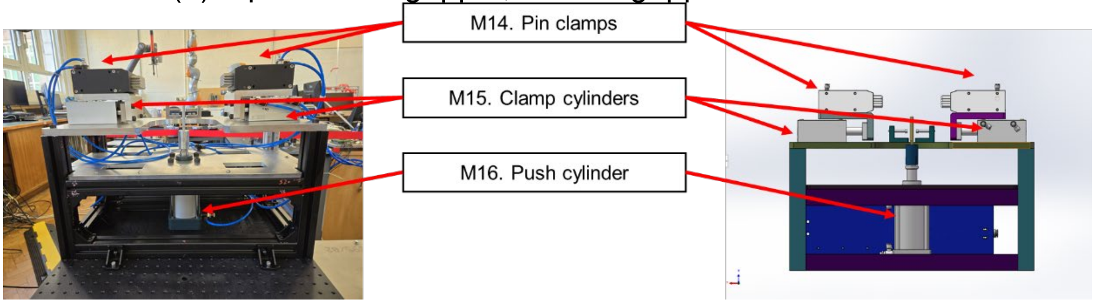

(e) A pin clamp device – front view

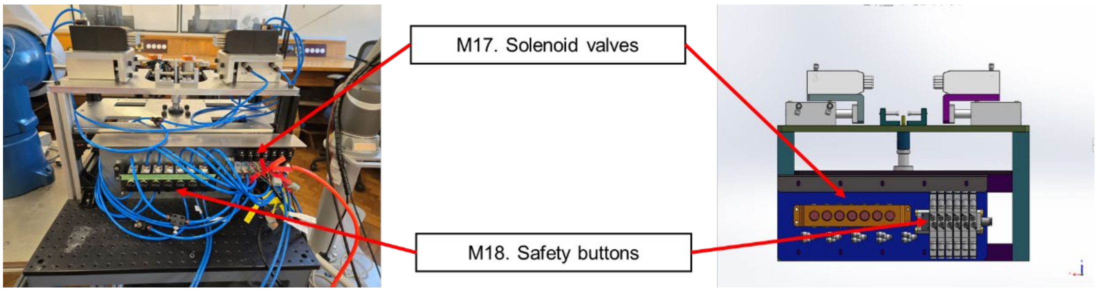

(f) A pin clamp device – back view

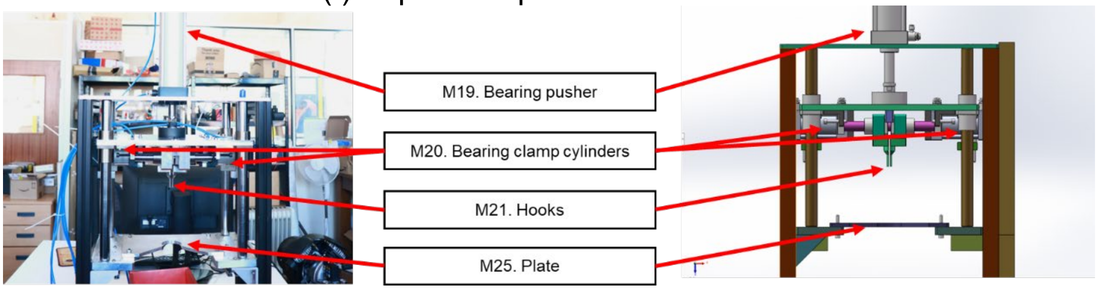

(g) Press-fit components disassembly device – front view

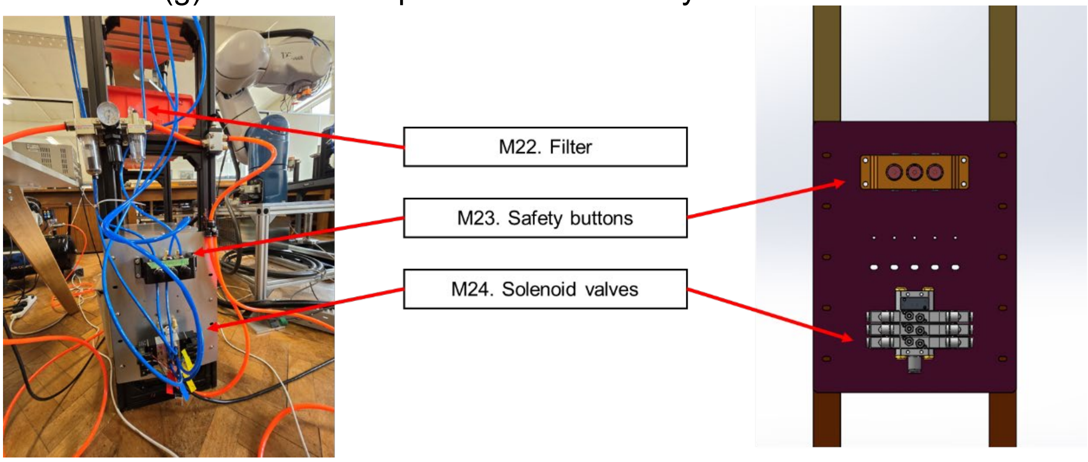

(h) Press-fit components disassembly device – side view

Figure C 1 Detailed design of the mechanical system in the robotic cell.

In this section, the design of the robotic cell for disassembling DC magnet motors is introduced in detail. The cell employs two robots, the Staubli robot (M.1) and the TM robot (M.3), each designated for specific tasks. The Staubli robot (M.1) is allocated for the Unplugging task (T.3) and the Pick and place task (T.6). A tool changer (Robot side) (M.2) is installed on the Staubli robot (M.1) to attach different grippers onto the robot (Figure C 1 (a)). Tool changers (tool side) are installed on a pneumatic gripper (M.10) and an electric gripper

(M.11) (Figure C 1 (d)). The pneumatic gripper (M.10) and electric gripper (M.11) are designed for cylindrical objects and irregularly shaped objects, respectively. During operation, these 2 grippers are stored on tool stands (M.12) on an optical table, allowing the Staubli robot (M.1) to use them as needed. Moreover, the TM robot (M.3) is allocated to the Coil disassembly task (T.4) and the Unscrewing task (T.5) in the disassembly process. A set of tools, including a Screwdriver (M.5), a 2D camera (M.4), an FT sensor (M.6), a cutting tool (M.7) and an electromagnet (M.8), are installed on the TM robot (Figure C 1 (b) and (c)).

There are 2 different functionalities on the Pin clamp device (Figure C 1 (e) and (f)): first, this device clamps the motor from both sides. Typically, the shapes of motors are irregular, e.g., the slotted structure is designed for cooling so that the pin clamps (M.14) adapt to different shapes of motors. The clamp cylinders (M.15) generate a very large holding force to hold the motors. Second, the push cylinder (M.16) is designed to push the Rotor set (B) out of the Stator set (C.13) and can provide 3939.6 N at 0.8Mpa (YHDFA, n.d.).

Regarding the press-fit component disassembly device, this device is designed to address the Press-in task (T.1) and Press-on task (T.2) (Figure C 1 (g) and (h)). For the Press-in task (T.1), the hooks (M.21) are inserted into the Bearing (large) (A.2). The bearing clamp cylinders (M.20) are opened to hold the bearing; then, the bearing pusher (M.19) is moved up to pull out the bearing. For the Press-on task (T.2), the bearing clamp cylinders (M.20) are closed, and the hooks work as push pins. The bearing pusher (M.19) is moved downwards to push the shaft of the Rotor set (B) out of the Bearing (large) (A.2).

The screwdriver (M.5), cutting tool (M.7), electromagnet (M.8) and electric gripper (M.11) are driven by electric signals, as introduced in Appendix D. The tool change (tool side) (M.9), pneumatic gripper (M.10), pin clamp device and press-fit component disassembly device are driven by airflow.

All the components are designed via SolidWorks 2022 software. Bill of material (BOM) is prepared for purchase or manufacturing. Mechanical, electric and pneumatic products are purchased on the industrial market. Machinery components are drawn in 2D views and are sent to manufacturers in factories. The final assembly was carried out by the team at the Autonomous Remanufacturing Laboratory (LF03). Before the experiments were conducted, initial tests were performed to validate the designs following the completion of electrical and pneumatic cabling.

In the subsequent section, the electrical system are discussed.

Appenxdix D. System design: Electric systems

This section provides an overview of the electric systems integrated within the robotic cell. The Staubli robot (M.1) operates as the primary controller (a server), executing the main programs and controlling the electric gripper (M.10). The TM robot (M.3), working as a client, controls devices through I/O ports, including solenoid valves that actuate all pneumatic devices (M.2, M.11, M.14 - M.17, M.19 and M.20), a screwdriver (M.7), a cutting tool (M.8) and an electromagnet (M.9)).

The electric power system is shown in Table D 1. All solenoid valves, the electromagnet (M.8) and the FT sensor (M.6) are powered by DC 24-voltage I/O ports on the TM robot (M.3). The screwdriver (M.5) and cutting tool (M.7) are powered by a 230 V AC wall plug socket. The electric gripper (M.11) is powered by an external DC power supply at 24 V.

The communication methods and connections are summarised in Figure D 1 and Table D 2. The Stuabli robot (M.1) is linked to the TM robot (M.3) via an Ethernet RJ45 cable on ethernet ports via the socket TCP/IP protocol. In this configuration, the Staubli robot (M.1) operates as a server, and the TM robot (M.3) works as a client connected through an assigned IP address. In robotic communication, the Staubli robot transmits I/O control signals to the TM robot, which processes these signals to toggle their I/O ports accordingly. The electric gripper (M.10) is connected to the Staubli robot (M.1) by a RJ45 cable on an

EtherCAT port, sending 16-bit binary information to control the gripper model, the position of each finger, and the speed and force on the electric gripper.

The FT sensor (M.6) is connected with the TM robot (M.3) on an EtherCAT port, enabling the transfer of force and torque data along three axes for real-time analysis. The TM robot (M.3) is equipped with 15 I/O ports supplying 24 V DC signals to control various subcomponents, including the screwdriver (M.7), electromagnet (M.9) and all solenoid valves for the tool changer (Robot side) (M.2), pneumatic gripper (M.11), pin clamp device (M.14–M.17) and Press-fit component disassembly device (M.19–M.20). The mechanical locking mechanism of the tool changer (tool side) (M.9) is controlled pneumatically via airflow and is regulated by solenoid valves. This allows the Staubli robot (M.1) to interchange tools by connecting to the tool changer (tool side) (M.9). The detailed design of the pneumatic system is introduced in the next section.

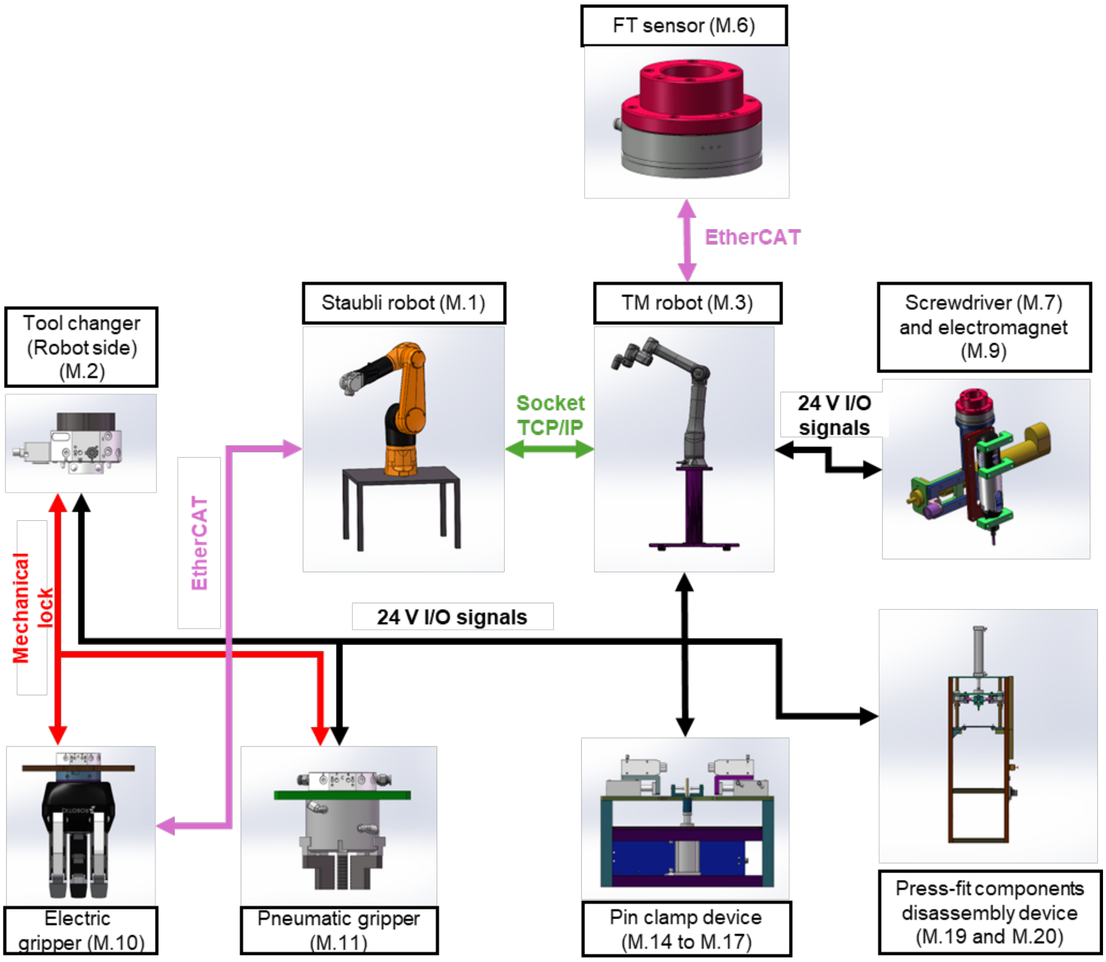

Figure D 1 Overall communication schematics in the robotic system.

Table D 1 Mapping of the electric power supply and I/O ports.

No	**1**	**2**	**3**	**4**	**5**	**6**	**7**	**8**	**9**
Components	1 Push cylinder (M.16)	2 Clamp cylinders (M.14)	2 Pin clamps (M.15)	2 Bearing clamp cylinders (M.20)	1 Bearing push cylinder (M.16)	Tool changer (M.1)	Pneumatic gripper (M.10)	Screwdriver (M.5)	Electromagnet (M.8)
Power supply	TM I/O 0&7	TM I/O 1&8	TM I/O 2&9	TM I/O 3&10	TM I/O 4&11	TM I/O 5&12	TM I/O 6&13	Wall plug	TM I/O 15
Voltages (V)	**24**							**230**	**24**

No	**10**	**11**	**12**
Components	Cutting tool (M.7)	Electric gripper (M.11)	FT sensor (M.6)
Power supply	Wall plug + cable extension	External power supplier	TM ECAT power port
Voltages (V)	**230**	**24**	**24**

Table D 2 I/O communication mapping.

TM I/O	**0**	**1**	**2**	**3**	**4**	**5**	**6**
Cable	In P1	In P2L & In P2R	In P3R	In P4L & In P4R	In P5	In P6	In P7
Devices	Pin clamp device			Press-fit component disassembly device		1 Tool changer (M.1)	1 Pneumatic gripper (M.10)
Component (s)	1 Push cylinder (M.16)	2 Clamp cylinders (M.14)	2 Pin clamps (M.15)	2 Bearing clamp cylinders (M.20)	1 Bearing push cylinder (M.16)	-	-
Action	Push up	Clamps close	Pin clamps lock	Clamps close	Push down	Tool changer Lock	Gripper close

TM I/O	**7**	**8**	**9**	**10**	**11**	**12**	**13**
Cable	Out P1	Out P2L	Out P3R	Out P4L & Out P4R	Out P5	Out P6	Out P7
Devices	Pin clamp device			Press-fit component disassembly device		1 Tool changer (M.1)	1 Pneumatic gripper (M.10)
Component (s)	1 Push cylinder (M.16)	2 Clamp cylinders (M.14)	2 Pin clamps (M.15)	2 Bearing clamp cylinders (M.20)	1 Bearing push cylinder (M.16)	-	-
Action	Push down	Clamps open	Pin clamps unlock	Clamps open	Push up	Tool changer Unlock	Gripper open

TM I/O	14	15	Ethernet port	RJ45 Ecat	**Stabil I/O**	J206	J207
Cable	Power cables	Power cables	RJ45	RJ45	**Cable**	RJ45 (green)	RJ45
Devices	Screwdriver (M.5)	Electromagnet (M.8)	Staubli robot	FT sensor ATI M20	**Devices**	3-finger electric gripper	TM robot
Component (s)	-	-	-	-	**Component (s)**	-	-
Action	on/off	On/off	Data transfer	Data transfer	**Action**	on/off	Data transfer

Appenxdix E. System design: Pneumatic system

This section details the pneumatic system used in the robotic cell (Figure E 1). The airflow is generated by a compressor and passes through a filter (M.22), which stabilises the pressure and removes moisture and oil from the air. This prevents damage to pneumatic cylinders caused by moisture and oil. After the filter, the man pipe is split into 2 branches: one branch supplies air to the pin clamp device, the tool changer (tool side) (M.1) and pneumatic gripper (M.10), and the other branch supplies air to the press-fit component disassembly device.

All pneumatic cylinders are controlled via 5/3 solenoid valves (M.17). These valves control the direction and flow of air, and each valve has 3 operational positions. For example, when the push cylinder (M.16) is controlled, there are 3 different positions on a solenoid valve. (1) Initial position: In the initial position, where the solenoid valve (M.17) stays in the middle, no airflow enters the push cylinder (M.16). (2) Push operation: When the TM I/O 0 port is switched on by the TM robot (M.3), the solenoid valve (M.17) moves to the "right" side and then airflows into the push cylinder (M.16) pushes the rod through the safety button (M.18), causing the road to extend. The safety button (M.18) is designed to stop airflow in emergencies. Only if the safety button (M.18) is switched on can the airflow pass to the push cylinder (M.16). (3) Return operation: When the TM robot (M.3) switches the TM I/O 0 port off, the solenoid valve (M.17) moves back to the initial position. When the TM I/O 7 port is then switched, the solenoid valve (M.17) moves to the “left” side, resulting in the return of the rod back into the cylinder.

There are 3 solenoid valves on the pin clamp device. One of them controls the push cylinder (M.16) through the TM I/O 0 port (engage) and TM I/O 7 port (release). The second solenoid valve controls 2 clamp cylinders (M.15) through the TM I/O 1 port (engage) and TM I/O 8 port (release), and the last valve controls 2 pin clamps (M.14) on the TM I/O 2 port (engage) and TM I/O 9 port (release). The tool changes (Tool side) (M.1) and the Pneumatic gripper (M.10) are actuated as follows: (a) TM I/O 5 (engage) and TM I/O 12 port (release) for the tool changer and (b) TM I/O 6 (engage) and TM I/O 13 port (release) for the pneumatic gripper.

In the other loop connected to the press-fit component disassembly device, one solenoid valve controls 2 bearing clamp cylinders (M.20) on TM I/O 3 (engage) and TM I/O 10 ports (release). The bearing pusher (M.19) is controlled on the TM I/O 2 (engage) and TM I/O 9 port (M.19).

The high quality pneumatic diagram is available on this link, titled “motor disassembly - pneumatic drawing”:

https://doi.org/10.6084/m9.figshare.27934512.v2

Robot programming will be introduced in the next section.

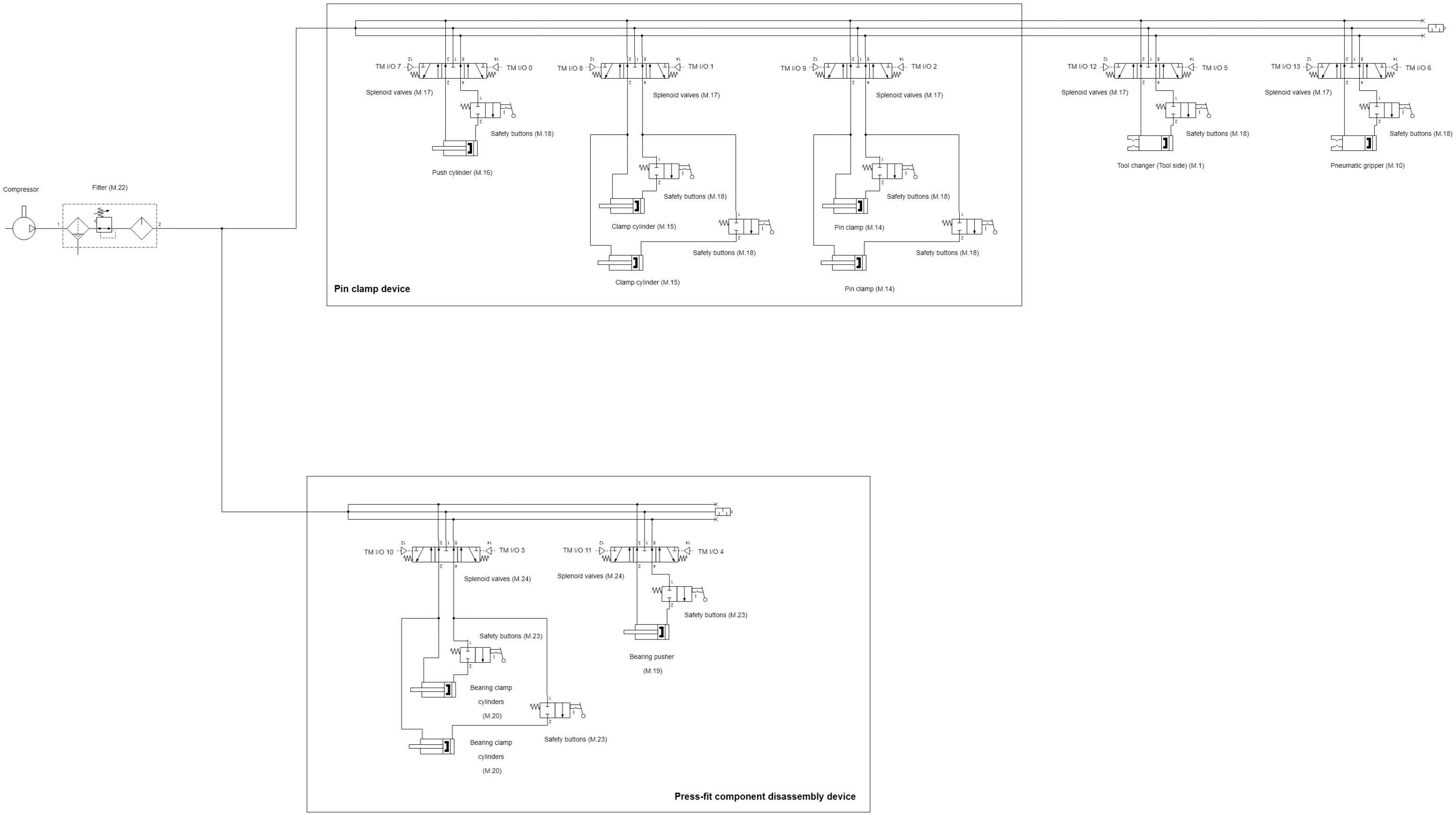

Figure E 1 Pneumatic system drawing.

Appenxdix F. Robotic programming

In this section, the robotic programming of each robot is introduced in detail, including the positions, speeds, movements, frames and communications (Table F 2). The Staubli robot (M.1) executes the main programs, whereas the TM robot (M.3) manages I/O controls and performs the Coil disassembly task (T.4) and Unscrewing task (T.5).

The programming for the Staubli robot was developed via Staubli Robotics Suite 2022.7.0 (SRS 2022.7.0) (Figure F 1 (a)). This software supports offline programming via the VAL 3 programming language and the integration of 3D CAD models. Before task execution, the programs are transferred between this software and the Stuabli robots. In contrast, the software TM flow 1.82.5100 is used for TM robot programming. Instead, its programming interface is graphical and is based on a drag–and–drop methodology to connect logic blocks for controlling operations. (Figure F 1 (b)).

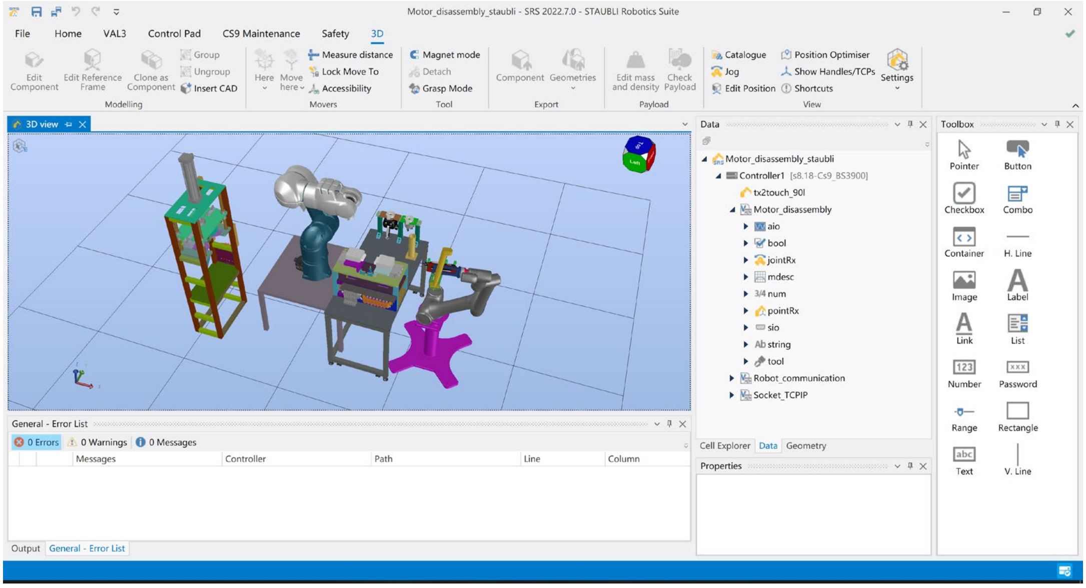

(a) Staubli robot programming software: SRS 2022.7.0

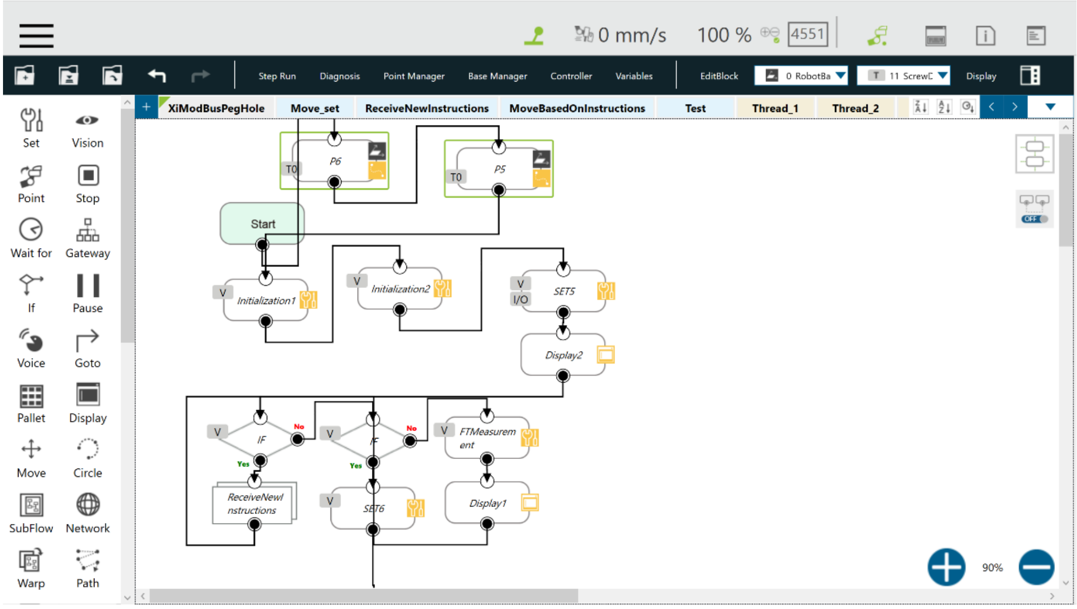

(b) TM robot programming software: TM flow 1.82.5100

Figure F 1 Programming software for the Staubli robot and TM robot.

First, the position of a point in the robot's workspace is defined as a joint point and a Cartesian point. (1) The joint point records the position of each robotic joint in degrees. (2) Record both the translational position (X, Y, Z) in millimetres and the rotational orientation (Rx, Ry, Rz) in degrees.

For the Staubli robot, these positions are predefined via 3D CAD models and task requirements within the SRS software. After programming, they are validated and adjusted during real-world testing. For the TM robot, the positions are recorded differently: the robot’s end effector is manually moved to the desired location by a human operator, and the position is saved either through the software interface or by pressing the robot’s "Point" button.

Second, with respect to the speed, the robot speed is classified into joint speed and linear speed. (1) The joint speed represents the speed of individual robotic joints, expressed as a percentage of the joint's maximum velocity. (2) Translational speed is the speed of the robot’s end effector or tool in millimetres per second (mm/s). The rotational speed is the speed of rotational movements in degrees per second (°/s).

There are 3 different speed settings on the Staubli robot for different movements (Table F 1):

- The ApproSpeed is the approach speed to an object. The tool changer (tool side) (M.2) approaches the tool changer (tool side) (M.9) at the approach speed, e.g..
- NomSpeed represents the normal speed for point-to-point movements.
- The UnplugSpeed is designed specifically for the Unplugging task (T.3), where the Rotor set (B) is removed from the Stator set (C.13).

Table F 1 Speeds used in the Staubli robot.

Name	Accel	Vel	Decel	Tvel	Rvel	Blend	Leave	Reach
ApproSpeed	20	5	20	20	20	Cartesian	5	5
NomSpeed	100	100	100	99.9	99.9	Joint	50	50
UnplugSpeed	50	18	20	20	20	Cartesian	50	5

where Accel and Decel represent the joint acceleration and deceleration, respectively, of the Staubli robot as percentages. Vel is the joint speed of the robot as a percentage. Tvel is the translational speed (linear speed) in millimetre per second (mm/s), and Rvel is the rotational speed in degrees per second (°/s). Blend is a blend model for the control, which has off (no blending), joint (blending) and Cartesian (blending) modes. Leave is the distance between the target point at which blending starts and the next point in millimetres. Reach represents the distance between the target point at which blending stops and the next point in millimetres. For the TM robot, default values are used: (1) the joint speed is 5%, and (2) the linear speed is 5 mm/s.

Third, the movements of the robot are summarised as point-to-point (PTP) movements, linear movements, circular movements and blending movements (Staubli, 2018):

(i) The point-to-point movement occurs when the robot moves from one point (initial position) to another point (final position) (Figure F 2 (a)). PTP movement can be joint type (moving joint angles) or Cartesian type (moving the end of the effector in Cartesian coordinates).

(ii) The linear movement represents the movement of the robot along a straight line between two points or over a specific distance (Figure F 2 (b)). This is normally used on approaching objects.

(iii) The circle movement defines the movement of the robot along a circular path, which is useful for tasks requiring arc-like motions (Figure F 2 (c)).

(iv) The blending movement combines smooth transitions between consecutive movements, preventing abrupt stops (Figure F 2 (d)).

The programs of the Staubli robot and TM robot use only point-to-point (PTP) movement and linear movement based on tasks (Table F 2).

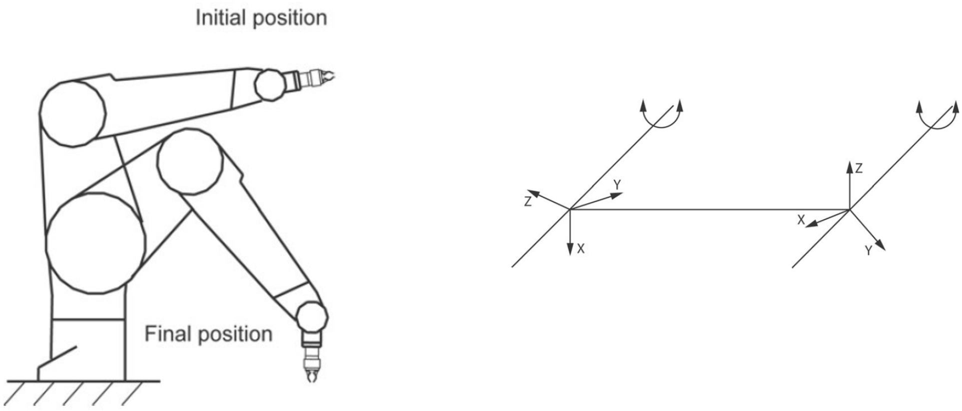

(a) Point-to-Point movement (b) Linear movement

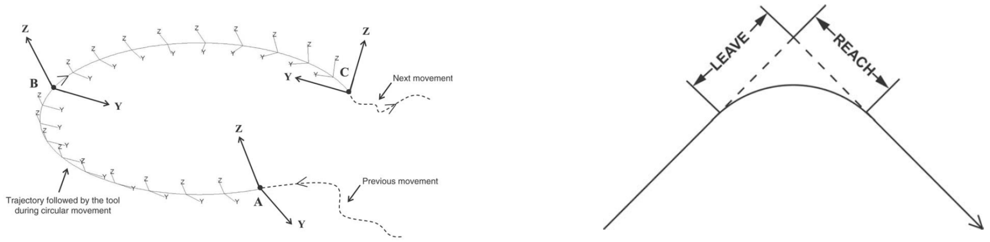

(c) Circle movement (d) Blending movement

Figure F 2 Explanation of robot movements (Staubli, 2018).

Fourth, the frame is defined as a reference frame in the movement, including word frame, Flange frame and Tool Centre Point (TCP) frame. (1) The word frame is defined such that the robot moves to a position according to the robot base. (2) The flange frame is defined such that the robot moves on the basis of the robot flange. (3) The TCP frame, which is defined by the user, is the tool centre fixed on the end of the effector on the robot.

The TCP of the Staubli robot can be set via a 3D CAD model in the SRS software. The TCP is set at the surface of the tool changer (Robot side) (M.2)

(Figure F 3 (a)). The TCP remains the same to simplify the programs when different grippers are installed. In contrast, the TCPs of the cutting tool (M.7) (Figure F 3 (b)), screwdriver (M.5) (Figure F 3 (c)) and electromagnet (M.8) (Figure F 3 (d)) are set on the TM robot system.

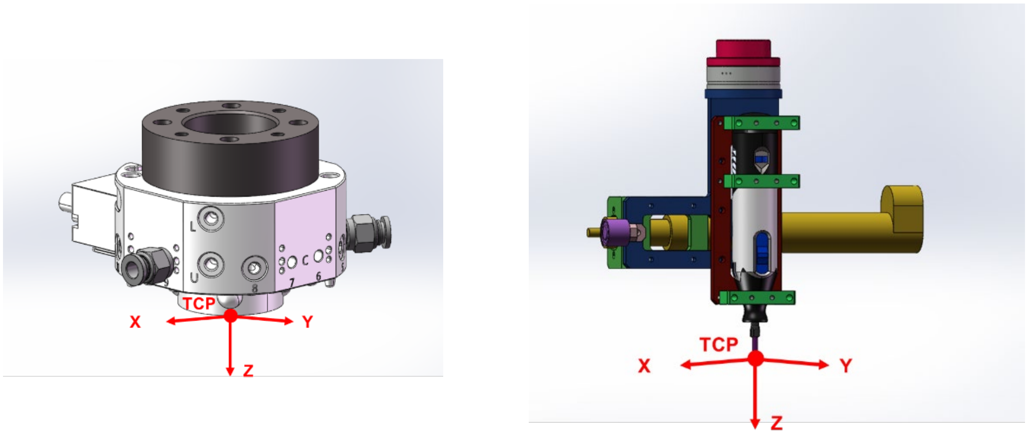

(a) TCP on the Tool changer (Robot side) (M.2)

(b) TCP on Cutting tool (M.7)

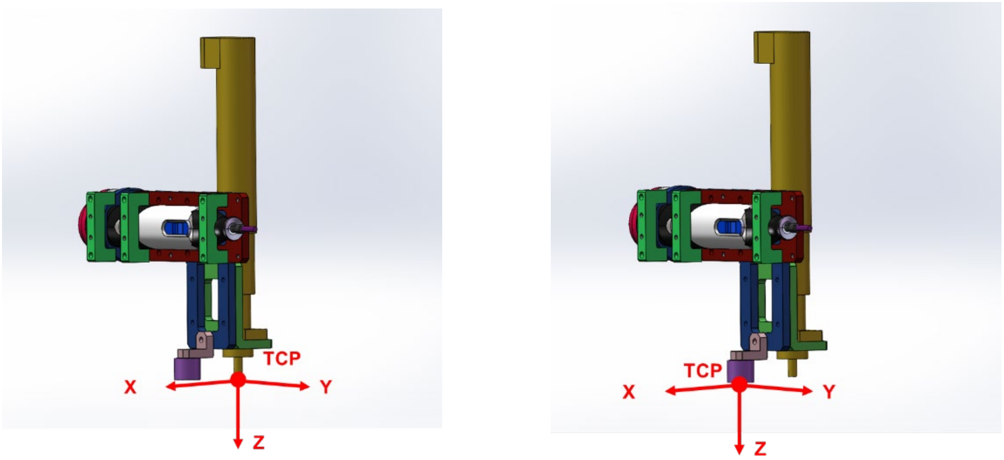

(c) Screwdriver (M.5)

(d) Electromagnet (M.8)

Figure F 3 TCP settings for different tools.

Finally, the communication system in the robotic cell serves two main purposes: (1) control of switch-on/switch-off actions for various tools and devices and (2) information exchange between the Staubli robot (M.1) and TM robot (M.3) to synchronise operations. Details of the robotic communication are introduced in Appendix D.

Table F 2 Robot execution during the disassembly process.

Steps	Object components	Programme name	Staubli actions	Comments - Staubli	TM actions	Comments - TM
1	-	Go_Home	Go jHome	Joint move, normal speed		
2	Pneumatic gripper (pick)	Pick_Pne_Gripper			Swith on I/O 12	Tool changer - unlock
			Go appro pPne_Gripper	Joint move, normal speed		
			Go pPne_Gripper	PTP, appro speed		
					Swith off I/O 12	Tool changer - unlock
					Swith on I/O 05	Tool changer - lock
			Go appro pPne_Gripper	PTP, appro speed		
			Go jHome	Joint move, normal speed		
3	Electric motor (pick)	PM_T1_PP_Motor			Swith on I/O 13	Pneumatic fingers - open
					Swith off I/O 13	Pneumatic fingers - open
			Go appro pPM_1_Motor	Joint move, normal speed		
			Go pPM_1_Motor	PTP, appro speed		
					Swith on I/O 6	Pneumatic fingers - close
			Check and Confirm	-		
			Go appro pPM_1_Motor	PTP, appro speed		
4	4 screws	PM_T2_Unscrewing	Go appro pPM_2_Unscrewing	Joint move, normal speed		
			Go pPM_2_Unscrewing	PTP, appro speed		
					Send I/O = 16	Tell TM to run Unscrewing task
			Check and Confirm	-		
5	Rotor and Front case	PM_T3_PP_Fixture_Cutting	Go appro pPM_3_Cutting_Fixture	Joint move, normal speed		
					Swith on I/O 8	2 Clamps - open
					Swith off I/O 8	2 Clamps - open
			Go pPM_3_Cutting_Fixture	PTP, appro speed		
					Swith on I/O 1	2 Clamps - close
					Swith off I/O 1	2 Clamps - close
					Swith on I/O 2	2 pin - lock
					Swith off I/O 2	2 pin - lock
			Check and Confirm	-		
					Swith on I/O 17	push cylinder - push up
			Go appro pPM_3_Cutting_Fixture	PTP, UnplugSpeed		
					Swith off I/O 17	push cylinder - push up
					Swith on I/O 7	push cylinder - push down
					Swith off I/O 7	push cylinder - push down
6	Rotor and Front case	PM_T4_Rotor_Pne_Gripper	Go appro pPM_4_Rotor_Pne_Gripper	Joint move, normal speed		
			pPM_4_Rotor_Pne_Gripper	PTP, appro speed		
					Swith off I/O 6	Pneumatic fingers - close
					Swith on I/O 13	Pneumatic fingers - open
			Go appro pPM_4_Rotor_Pne_Gripper	PTP, appro speed		
					Swith off I/O 13	Pneumatic fingers - open

7	Pneumatic gripper (drop)	Drop_E_Gripper	Go appro pE_Gripper	Joint move, normal speed		
			Go pPne_Gripper	PTP, appro speed		
					Swith off I/O 5	Tool changer - lock
					Swith on I/O 12	Tool changer - unlock
			Go appro pE_Gripper	PTP, appro speed		
					Swith off I/O 12	Tool changer - unlock
			Go jHome	Joint move, normal speed		
8	Electric gripper (pick)	Pick_Pne_Gripper			Swith on I/O 12	Tool changer - unlock
			Go appro pPne_Gripper	Joint move, normal speed		
			Go pPne_Gripper	PTP, appro speed		
					Swith off I/O 12	Tool changer - unlock
					Swith on I/O 5	Tool changer - lock
			Go jHome	Joint move, normal speed		
9	Rotor and Front case	PM_T5_Rotor_E_Gripper	E_Gripper_control - open	call E gripper open		
			Go appro pPM_5_Rotor_Front_Case_E_Gripper	Joint move, normal speed		
			Go pPM_5_Rotor_Front_Case_E_Gripper	PTP, appro speed		
			E_Gripper_control - close	call E gripper close		
			Go appro pPM_5_Rotor_Front_Case_E_Gripper	PTP, appro speed		
10	Front case	PM_T6_Pressfit_Front_Case_Rotor	Go Trans2	Joint move, normal speed		
			Go Trans3	Joint move, normal speed		
					Swith on I/O 11	Bearing pusher - move up
					Swith off I/O 11	Bearing pusher - move up
					Swith on I/O 3	2 Bearing clamp cylinders - close
					Swith off I/O 3	2 Bearing clamp cylinders - close
			Go appro pPM_6_Pressfit_Front_Case_Rotor	Joint move, normal speed		
			Go pPM_6_Pressfit_Front_Case_Rotor	PTP, appro speed		
			E_Gripper_control - open	call E gripper close		
			Go appro pPM_6_Pressfit_Front_Case_Rotor	PTP, appro speed		
			Check and Confirm			
					Swith on I/O 4	Bearing pusher - move down
					Swith off I/O 4	Bearing pusher - move down
					Swith on I/O 11	Bearing pusher - move up
					Swith off I/O 11	Bearing pusher - move up
11	Bearing (Large)	PM_T7_Pressfit_Front_Case	Go appro pPM_6_Pressfit_Front_Case_Rotor	Joint move, normal speed		
			Go pPM_6_Pressfit_Front_Case_Rotor	PTP, appro speed		
			E_Gripper_control - close			
			Go appro pPM_6_Pressfit_Front_Case_Rotor	PTP, appro speed		
			Go appro pPM_7_Pressfit_Front_Case	Joint move, normal speed		
					Swith on I/O 3	2 Bearing clamp cylinders - close
					Swith off I/O 3	2 Bearing clamp cylinders - close
					Swith on I/O 4	Bearing pusher - move down
					Swith off I/O 4	Bearing pusher - move down

			Go appro pPM_7_Pressfit_Front_Case	PTP, appro speed		
			Go pPM_7_Pressfit_Front_Case	PTP, appro speed		
			Check and Confirm			
					Swith on I/O 10	2 Bearing clamp cylinders - open
			E_Gripper_control - open			
			Go appro pPM_7_Pressfit_Front_Case	PTP, appro speed		
					Swith on I/O 11	Bearing pusher - move up
					Swith off I/O 11	Bearing pusher - move up
					Swith off I/O 10	2 Bearing clamp cylinders - open
					Swith on I/O 3	2 Bearing clamp cylinders - close
					Swith off I/O 3	2 Bearing clamp cylinders - close
12	Coil disassembly	-			Run coil cutting programe	

Appenxdix G. Robotic trajectory planning

This section introduces the robotic trajectory planning for the Coil disassembly task (T.4) (Figure G 1 and Table G 1). The algorithm can be implemented in the robot to execute the Coil disassembly task (T.4).

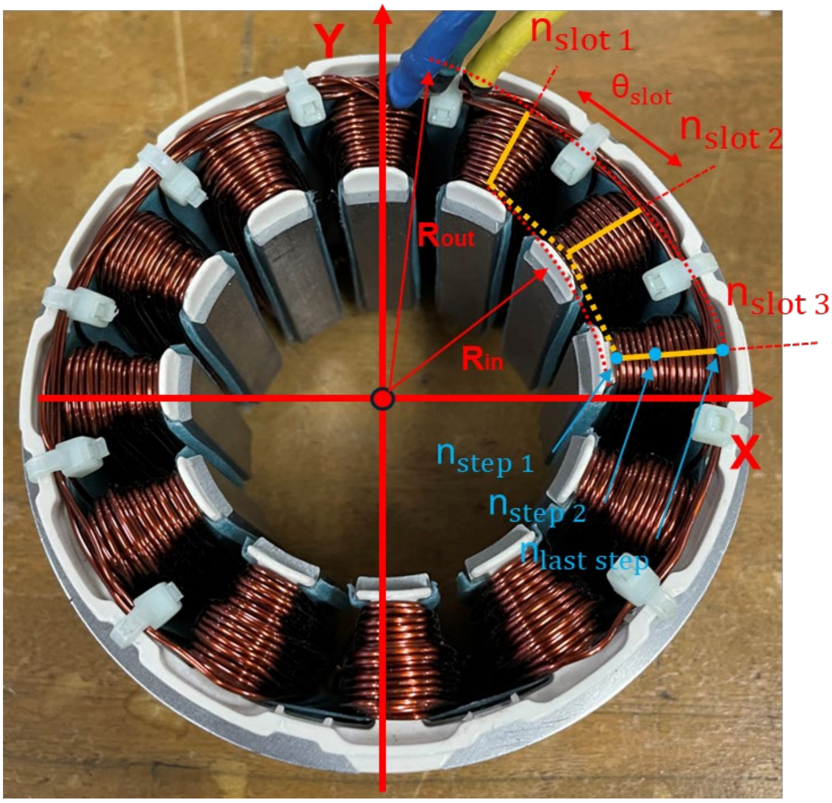

Figure G 1 Robotic trajectory planning for the Coil disassembly task (T.4)

Table G 1 Trajectory algorithm for the Coil disassembly task (T.4).

```
$\theta_{slot} = \frac{360}{n_{slot}}$
For loop ($n_{slot}$): from $n_{slot\ 1}$ to$n_{last\ slot}$
    For loop ($n_z$): from $n_{depth\ 1}$ to$n_{last\ depth}$
    $Z_{(n_{step}, n_{slot}, n_{depth})} = Z_1 + n_{depth} {}^{*} D_{cut}$
        For loop ($n_{step}$): from $R_{in}$ to$R_{out}$
        $X_{(n_{step}, n_{slot})} = (R_{in} + n_{step} * D_{move}) * \cos(\theta_{slot} {}^{*} n_{slot})$
```

```
        $Y_{(n_{step},n_{slot})} = (R_{in} + n_{step} * D_{move}) * \sin(\theta_{slot} * n_{slot})$
        $P_{(n_{step},n_{slot},n_{depth})} = (X_{(n_{step},n_{slot})}, Y_{(n_{step},n_{slot})}, Z_{(n_{step},n_{slot},n_{depth})})$
        Robot move to $P_{(n_{step},n_{slot},n_{depth})}$
        $n_{step} = n_{step} + 1$
        End For loop ($n_{step}$): from $R_{in}$ to $R_{out}$
    $n_{depth} = n_{depth} + 1$
    End For loop ($n_z$): from $n_{depth\ 1}$ to $n_{last\ depth}$
$n_{slot} = n_{slot} + 1$
End For loop ($n_{slot}$): from $n_{slot\ 1}$ to $n_{last\ slot}$
```

Appenxdix H. Force and position records in the coil disassembly process

With respect to the Coil disassembly task (T.4), this section provides the cutting forces and speeds recorded during robotic milling on the Stator set (C.13) (Figure H 1).

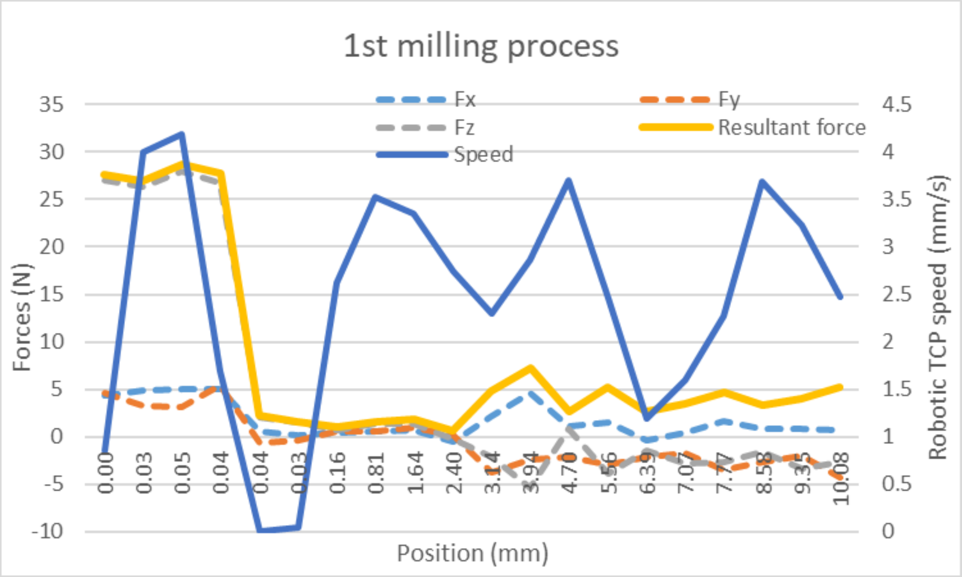

(a) Forces and speed recording in the 1st milling process

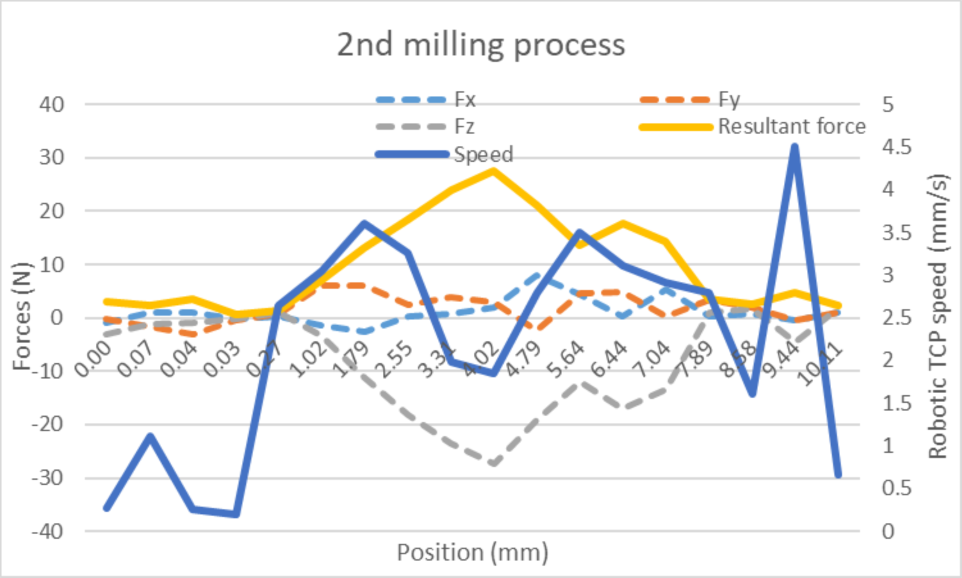

(b) Forces and speed recording in the 2nd milling process

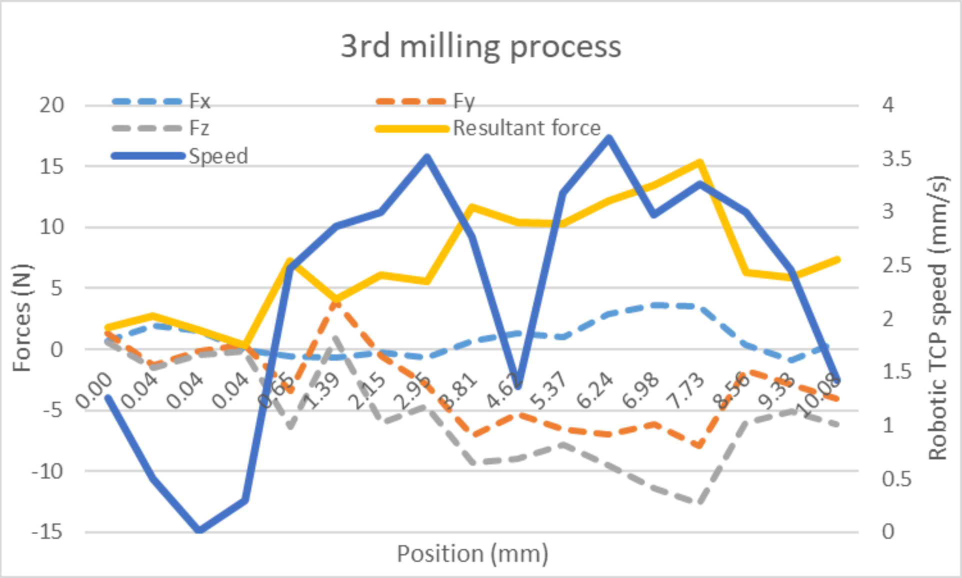

(c) Forces and speed recording in the 3rd milling process

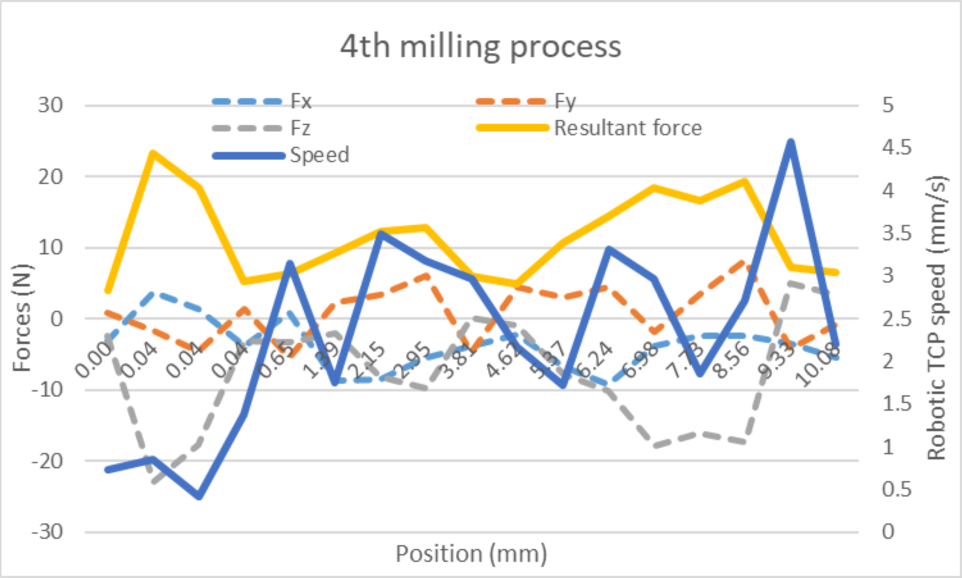

(d) Forces and speed recording in the 4th milling process

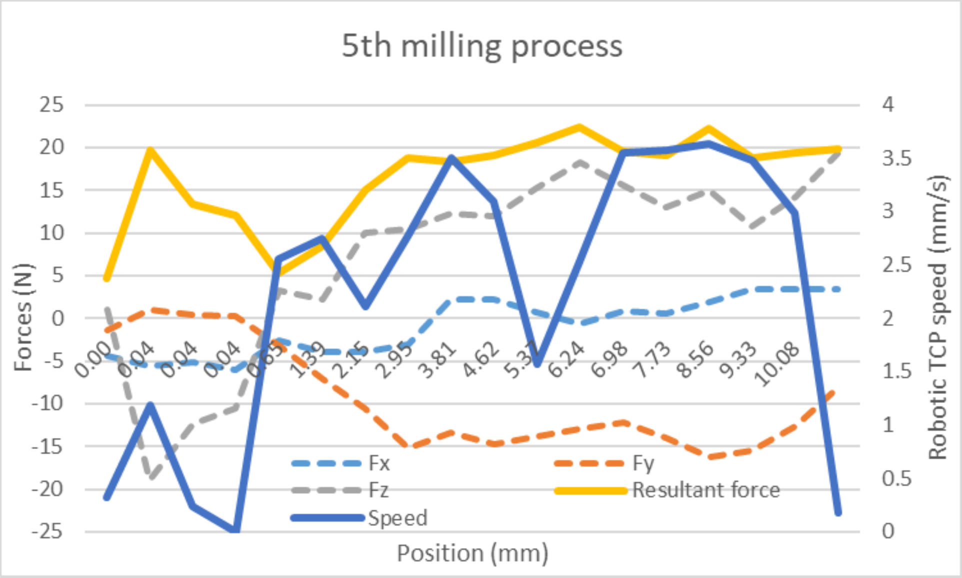

(e) Forces and speed recording in the 5th milling process

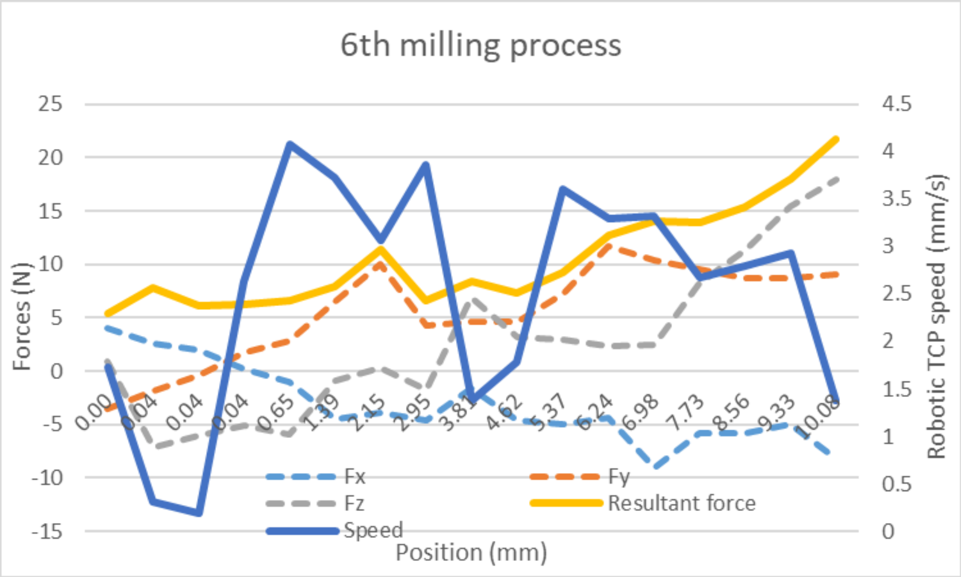

(f) Forces and speed recording in the 6th milling process

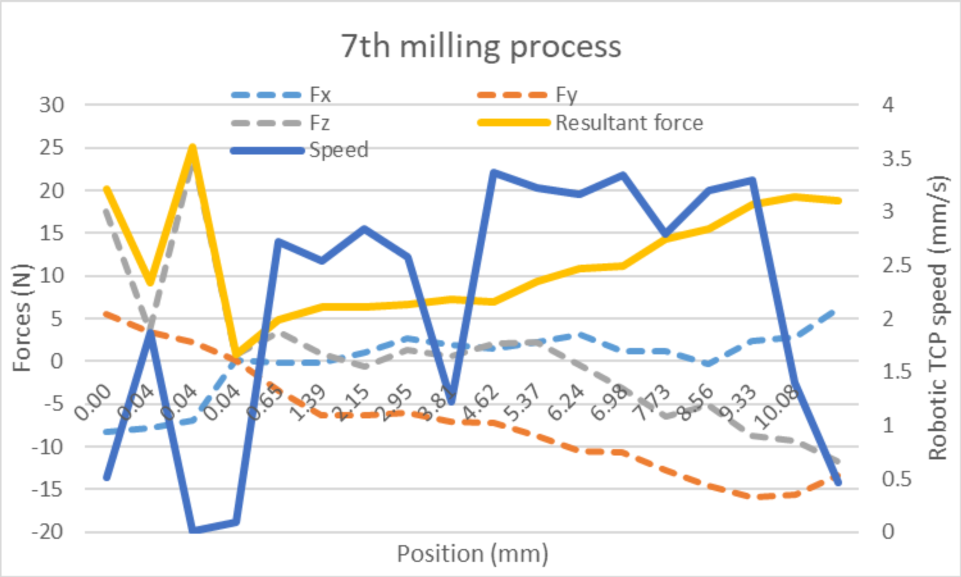

(g) Forces and speed recording in the 7th milling process

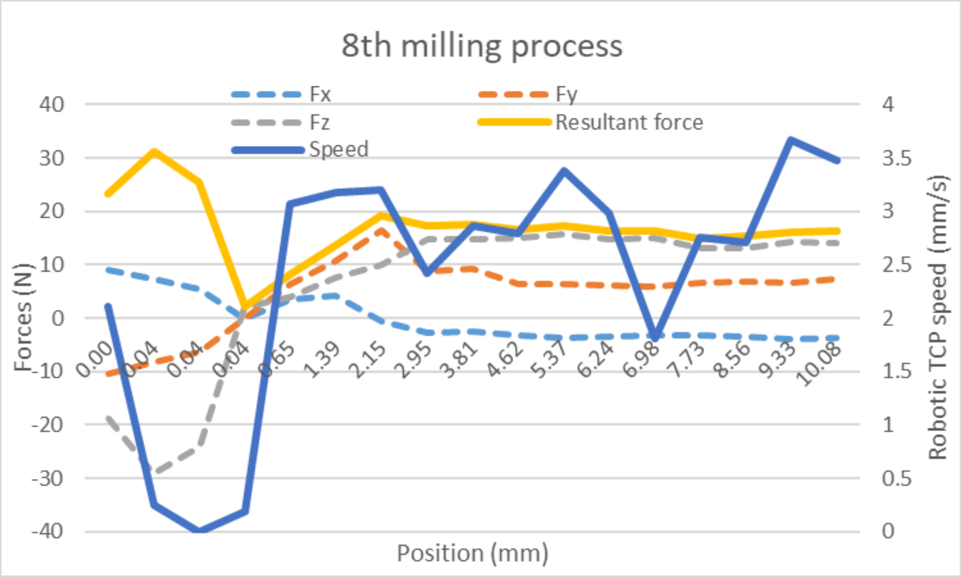

(h) Forces and speed recording in the 8th milling process

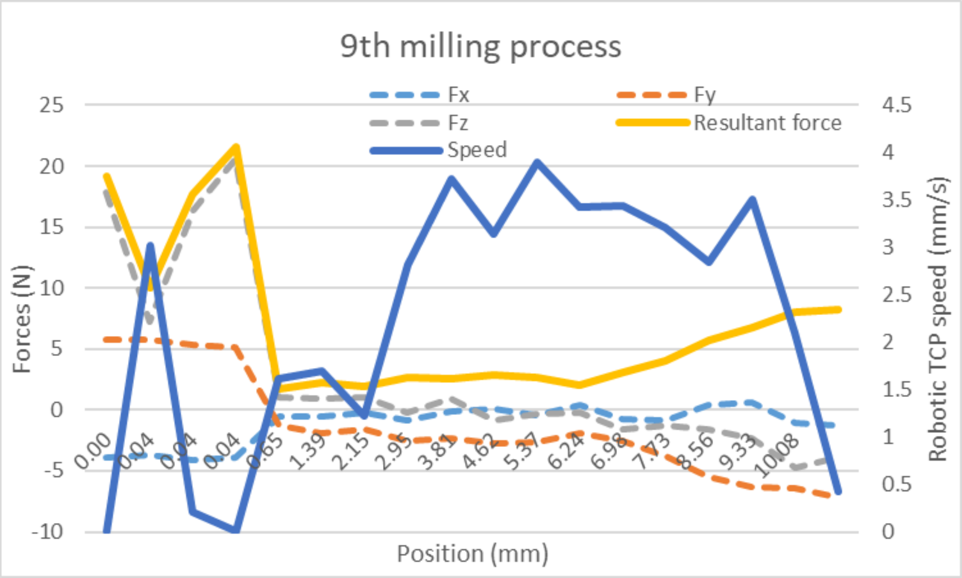

(i) Forces and speed recording in the 9th milling process

Figure H 1 Cutting forces and speeds recorded during robotic milling on the stator set (C.13).